The polarization of Λ^0 hyperons in quasi-real photoproduction

Michiel Demey

The polarization of Λ^0 hyperons in quasi-real photoproduction

ACADEMISCH PROEFSCHRIFT

ter verkrijging van de graad van doctor
aan de Universiteit van Amsterdam
op gezag van de Rector Magnificus
prof. dr. J.W. Zwemmer
ten overstaan van een door het college voor promoties
ingestelde commissie,
in het openbaar te verdedigen in de Agnietenkapel
op vrijdag 16 maart 2007, te 12:00 uur

door
Michiel Demey

geboren te Sint-Niklaas, België

Promotiecommissie

Promotor: prof. dr. G. van der Steenhoven

Co-promotor: dr. J.J.M. Steijger

Overige Leden: prof. dr. S.C.M. Bentvelsen
prof. dr. J.H. Koch
prof. dr. ir. E.N. Koffeman
prof. dr. F.L. Linde
dr. W-D. Nowak
prof. dr. D. Ryckbosch

Faculteit der Natuurwetenschappen, Wiskunde en Informatica

The work described in this thesis is part of the research program of the *Nationaal Instituut voor Kernfysica en Hoge-Energiefysica* (NIKHEF) in Amsterdam, the Netherlands. The work was financially supported by the *Stichting voor Fundamenteel Onderzoek der Materie* (FOM), which is financially supported by the *Nederlandse organisatie voor Wetenschappelijk Onderzoek* (NWO).

Contents

Chapter 1

Introduction

Ever since the discovery by the EMC experiment [1] that the spin of the nucleon cannot be explained in terms of the spin of the quarks alone, the spin structure of the nucleon has been under detailed study. According to current views the spin of the nucleon originates from four components:

$$\frac{1}{2} = \frac{1}{2}\Sigma + \Delta G + L_q + L_G, \tag{1.1}$$

where the first term on the right-hand side represents the spin contribution of the quarks, the second term represents the spin contribution of the gluons and the third and fourth component that of the orbital angular momentum of the quarks and gluons, respectively. In our understanding of each of these components considerable progress has been made over the past decade both experimentally and theoretically. Nevertheless, there are several fundamental questions related to the spin structure of the nucleon which remain unanswered: Are the strange quarks polarized inside the nucleon? What is the spin structure of other baryons? What is the role of orbital angular momentum? What drives the relative size of each contribution of the various carriers of angular momentum?

The Λ^0 hyperon is a very good candidate to help answering the first two of these questions for various reasons. As it is the lightest hyperon it's relatively easily produced. More importantly, the Λ^0 hyperon decays into a proton and a pion in a parity violating weak decay which enables the determination of the Λ^0 hyperon polarization by measuring the angular distribution of its decay products. It is the purpose of this thesis to explore these ideas using the new silicon detector array, the Lambda Wheels (LW), at the HERMES experiment at DESY.

More specifically, the work presented in this thesis tries to answer three key questions:

- What is the role of the strange quark in the spin structure of the nucleon?
- Is the spin structure of the Λ^0 hyperon also different from the common expectation, which in this case states that the Λ^0 spin is entirely due to that of the strange quark?
- What is the transverse polarization distribution of quarks in the nucleon?

Although these questions cover different aspects of hadronic spin physics, a more detailed description will clarify that each question can be answered by the same type of measurement, i.e. the polarization of the Λ^0 hyperon under various kinematic conditions.

The role of the s-quark in nucleon spin structure has been under investigation ever since the inclusive spin structure function g_1 has been measured in spin-dependent deep-inelastic lepton scattering experiments. In all those experiments a non-zero contribution of strange quarks was found. Most recently, the HERMES experiment found that the spin of the s quark $\Delta s + \Delta \bar{s} = -0.085 \pm 0.013(\text{theo.}) \pm 0.008(\text{exp.}) \pm 0.009(\text{evol.})$ [2]. However, this measurement is not model independent, as it is based on the assumption of the validity of SU(3) flavor symmetry in hyperon β-decays which is open to question. Within another approach in which the quark helicity distributions are measured in semi-inclusive experiments that tag the contribution of a certain quark flavor by detecting a specific hadron in the final state the contribution of the s-quark was determined to be $\Delta s = 0.028 \pm 0.033(\text{stat.}) \pm 0.009(\text{syst.})$ [3]. Here the measurement is limited by low statistics and different model assumptions, i.e. that non leading order effects can be neglected. As these two results are not fully consistent, it remains an open question whether the s-quark in the nucleon is polarized or not. An answer to this question requires new measurements that are independent of the previous ones. Such a new measurement can be provided by determining the Λ^0 polarization. Ellis describes in his paper [4] that by measuring the longitudinal Λ^0 polarization, directed along the momentum of the Λ^0 in the laboratory frame, the correlation between the orientation of the u-quark and the s-quark in the target nucleon can be obtained. This requires the selection of those Λ^0 hyperons that are formed from the target remnant. While the HERMES spectrometer primarily selects Λ^0 hyperons that are formed from the scattered quark, the Lambda Wheels detector was designed to reconstruct Λ^0 hyperons of which more originate from the target remnant.

Regarding the second question first answers have already been provided by measurements from the HERMES [5], NOMAD [6] and E665 [7] experiments. These measurements are all based on a theoretical model by Jaffe [8] which relates the contribution of the u-quark spin to the Λ^0 spin to the polarization transfer from a longitudinally polarized beam to a longitudinally polarized Λ^0 hyperon. This model only applies to Λ^0 hyperons which are formed, and thus contain, the scattered quark. Unfortunately the few available measurements suffer from large uncertainties both statistically and systematically. A large uncertainty, for instance, is due to the unknown contribution from Λ^0 hyperons originating from the decay of heavier hyperons which could dilute or enhance the polarization of the Λ^0 hyperons originating directly from the scattered quark. Furthermore, the kinematic region where the measurements of the HERMES experiment overlap with those by the NOMAD experiment is very small. Additional measurements of the Λ^0 polarization, as they can be carried out by the LW are needed to clarify the experimental situation. The LW are designed to increase the hyperon statistics and extend the kinematic coverage of the data.[1]

The third question originates from the fact that there are three leading-order structure functions of the nucleon. The unpolarized structure function f_1 describes the momentum distribution of unpolarized quarks in an unpolarized nucleon. This function has been studied extensively and is well known. The helicity dependent structure function g_1 describes the longitudinal spin distribution of the quarks in a longitudinally polarized nucleon. It has been measured by various experiments including the HERMES experiment [2]. It is fairly well understood [10]. The third structure function is the transversity structure function h_1 which describes the distribution of transversely polarized quarks in a transversely polarized nucleon. Experiments addressing this third leading-order structure function have only been started since a few years. To access the transversity distribution three possible approaches are available [11]. Through measurements of single spin asymmetries of semi-inclusively produced hadrons off a transversely polarized target transversity can be measured [12]. With similar single spin asymmetry measurements involving the detection of a pion pair transversity can also be accessed [13]. While the third method involves measurements of the polarization of the Λ^0 hyperon produced on a transversely polarized target. The first two have already led to first results published by the HERMES collaboration. The third type of measurement has not yet been performed at HERMES, although a conference report [14] presents the first results by the COMPASS experiment on this subject. In a paper by Jaffe [8] it is explained how the Λ^0 polarization measured with a transversely polarized target is related to transversity. This measurement can be carried out with the HERMES experiment, especially now that the addition of the LW will increase the statistics for this

---

[1] The PhD thesis of A. Reischl [9] is devoted to measurements and simulations of contaminations due to heavier hyperons.

type of measurement.

In order to obtain further insight in the above stated questions more measurements of the polarization of the Λ^0 hyperon are needed, both to reduce the statistical errors on measurements performed in the past, and to reduce the systematical errors by using an independent method in obtaining the result. This can be achieved with the newly installed LW detector in the HERMES experiment. The analysis of the first complete data set obtained with the LW forms the main subject of this thesis.

To introduce the reader to the basic kinematic and dynamic parameters used in this thesis chapter 2 contains an introduction to the Deep Inelastic lepton Scattering (DIS) formalism. The theoretical models mentioned above are also discussed in chapter 2. A description of the HERMES experiment with which the measurements are performed is presented in chapter 3 after which a more detailed description of the Lambda Wheels detector and the tracking algorithms developed to analyze LW data is given in chapter 4. Chapter 5 provides a discussion of the reconstruction of Λ^0 hyperons using both the HERMES spectrometer and the LW detector. The reconstructed Λ^0 hyperons are used to evaluate their polarization. This is the subject of chapter 6. In chapter 7 the Λ^0 polarization measurements are related to the three questions posed above and the obtained results are interpreted accordingly. In the final chapter the results obtained in this thesis are summarized and an outlook is presented.

Chapter 2

Physics

This chapter provides the reader with an introduction to Deep Inelastic Scattering (DIS) and a discussion of Λ^0 polarization. In section 2.1 the basic kinematic and dynamic parameters used throughout this thesis are introduced. In section 2.2 the polarization of Λ^0 hyperons is discussed together with the main theoretical models used to predict or describe the main results. As the emphasis of this thesis is on the presentation of the experimental results, the present -more theoretical- chapter has no intention to be comprehensive.

2.1 Deep Inelastic Scattering (DIS)

The scattering process which is primarily studied at the HERMES experiment is called Deep Inelastic Scattering (DIS). In this scattering process the energy of the incoming particle is sufficiently high to break up the target nucleon. By analyzing the scattered particles it is possible to study the internal structure of the nucleon. Because both the target and the beam can be polarized such measurements can also be aimed at unraveling the different contributions to the nucleon spin.

In the HERMES experiment the incoming beam particle is an electron or a positron and the target nucleon a proton or a neutron. The interaction between the incoming lepton and the target nucleon is mediated by the exchange of a virtual photon γ^*.

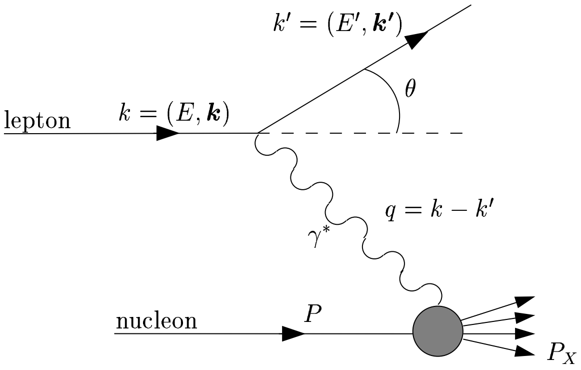

Figure 2.1: Schematic representation of a Deep Inelastic Scattering (DIS) event.

The DIS process is described by the three four-vectors k, q and P as pictured in figure 2.1. These three four-vectors give rise to six Lorentz invariant quantities: k^2, P^2, q^2, $P \cdot q$, $k \cdot q$ and $k \cdot P$. The first two are equal to, and thus represent, the masses of the incoming lepton, $k^2 = m_e^2$, and target nucleon, $P^2 = M^2$, respectively. The last two Lorentz invariants depend on the lepton variables and the mass of the nucleon:

$$\begin{aligned} k \cdot q &= k \cdot (k - k') = m_e^2 - (EE' - |\mathbf{k}||\mathbf{k'}| \cos\theta) && (2.1) \\ k \cdot P &= EM. && (2.2) \end{aligned}$$

In practice, the remaining two invariant quantities are most commonly used to characterize the scattering process. The first of these two is the four-momentum transfer squared:

$$q^2 = (k - k')^2 = 2m_e^2 + 2(|\mathbf{k}||\mathbf{k'}| \cos\theta - EE'), \tag{2.3}$$

which in the relativistic limit ($m_e \ll E$ and $E \approx k$) reduces to:

$$-q^2 \equiv Q^2 \overset{\text{lab}}{=} 4EE' \sin^2(\theta/2). \tag{2.4}$$

The second of the two remaining invariants is usually normalized by the target nucleon mass M

$$\frac{P \cdot q}{M} \equiv \nu \overset{\text{lab}}{=} E - E', \tag{2.5}$$

thus yielding the energy transfer in the laboratory ν. The two invariant quantities Q^2 and ν can also be redefined such that two dimensionless variables called x and y are introduced

$$x \equiv \frac{-q^2}{2P \cdot q} = \frac{Q^2}{2M\nu} \tag{2.6}$$

$$y = \frac{P \cdot q}{P \cdot k} \overset{\text{lab}}{=} \frac{E - E'}{E} = \frac{\nu}{E}. \tag{2.7}$$

The first of these variables is known as the Bjorken scaling variable and can be interpreted as the momentum fraction of the nucleon which is carried by the struck quark. The variable y is the fraction of the beam energy carried by the virtual photon.

In DIS the struck quark and the remnant target quarks are ejected in the scattering process and form color neutral hadrons which can actually be observed in the experiment. This process is known as hadronization. To distinguish between the two types of hadronization mentioned above (from struck or remnant quarks) the variable x-Feynman (x_F) is introduced:

$$x_F = \frac{p_{\|}}{p_{\|}^{\max}} = \frac{2p_{\|}}{W} \tag{2.8}$$

with

$$W^2 = (P + q)^2 = M^2 - Q^2 + 2M\nu \tag{2.9}$$

the invariant mass squared of the final hadronic state and

$$p_{\|} = \frac{\mathbf{p_h} \cdot \mathbf{q}}{|\mathbf{q}|} \tag{2.10}$$

the component of the momentum $\mathbf{p_h}$ of the hadron parallel to the momentum transfer vector.

A positive value of x_F indicates that the produced hadron most likely originates from the struck quark, this is also known as the current fragmentation region. A negative value, on the other hand, indicates that the hadron (most likely) originates from the target remnant which is called the target fragmentation region. These two fragmentation processes are pictured in figure 2.2. To clarify the distinction between the current and target fragmentation regions the scattering process is shown in the center of mass (c.m.) frame in the bottom panel of figure 2.2. Here one can see that if the momentum of the

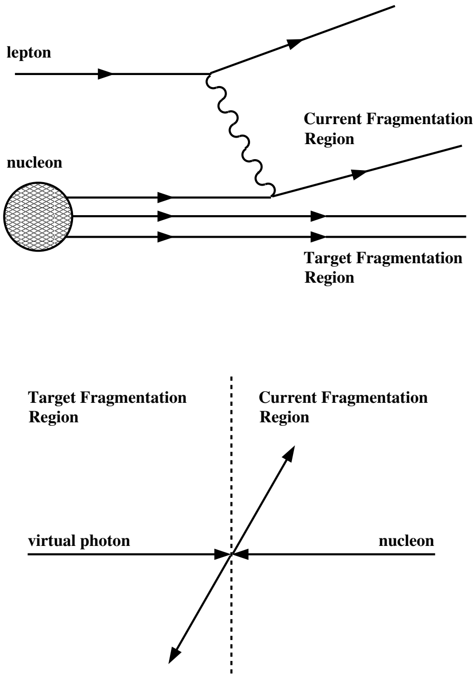

Figure 2.2: A schematic representation of the difference between current and target fragmentation. In the top panel the Feynman diagram is shown, the bottom panel shows the momenta in the nucleon-photon c.m. system.

hadron is directed towards the left side of the picture, in other words in the same direction as the target remnant, x_F will be negative which corresponds to target fragmentation. Current fragmentation corresponds to positive values of x_F where the momentum of the hadron is directed towards the right side of the picture and in the same direction as the virtual photon.

It should be noted that in the kinematic region covered by the HERMES experiment an absolute separation between current and target fragmentation is not possible. As explained in [15] Berger's criterion [16] can be used to arrive at a more accurate identification of current fragmentation events. Applying this criterion to HERMES kinematics one can select hadrons originating from the struck quark more purely by selecting the invariant mass of the hadronic state $W^2 \geq 23$ GeV^2 and the fraction of the energy transferred in the DIS process carried by the hadron $z \geq 0.2$. In figure 2.3 the spectra for W^2 and z obtained from a Monte Carlo simulation of the HERMES experiment are shown for events where a Λ^0 hyperon is detected without the requirement of a detected scattered beam lepton. The different distributions labeled as LW, short and long represent three different types of tracks reconstructed in the HERMES experiment, which will be described in detail in section 4.3. From figure 2.3 it can be seen that the requirement on W^2 selects 50%, 53%

and 72% of the events in the case of LW, short and long tracks, respectively. Therefore the LW and short track sample will contain more of a mixture of Λ^0 hyperons originating from current and target fragmentation processes whereas the long track sample contains mostly Λ^0 hyperons created in the current fragmentation region.

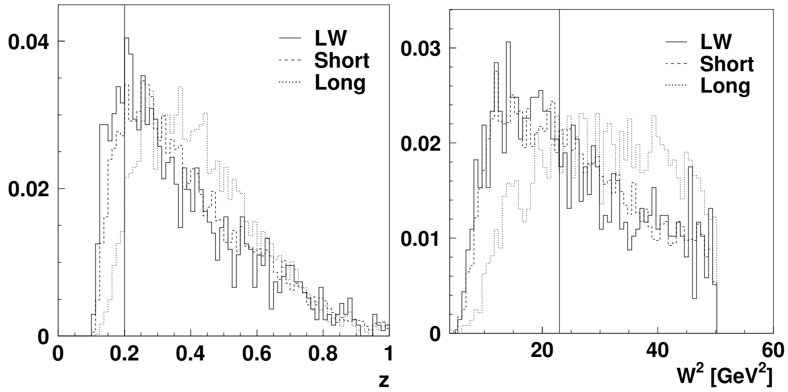

Figure 2.3: Distribution of events in the kinematic variables z (left) and W^2 (right) as obtained from a MC simulation where a Λ^0 hyperon is detected in the HERMES spectrometer and the scattered beam lepton is not. The three types of histograms represent the different types of tracks reconstructed in the HERMES experiment, which are described in detail in section 4.3.

The models describing the polarization of the Λ^0 hyperon discussed in the next section differ substantially depending on which of the two complementary fragmentation regions they correspond to. Hence a clear distinction will be made between the regions both when the data and the models are discussed.

2.2 Λ^0 Polarization

When discussing Λ^0 hyperon polarization a distinction must be made between transverse and longitudinal measurements of the Λ^0 polarization. In the transverse case, the Λ^0 polarization is directed perpendicular to the Λ^0 production plane. Such a polarization may emerge spontaneously and can thus be measured with an unpolarized beam and an unpolarized target. It is still unclear however what the underlying mechanism is that gives rise to such a spontaneously emerging transverse Λ^0 polarization [17]. In the longitudinal case, the Λ^0 polarization is directed along the momentum of the Λ^0. It originates from the polarization of the beam and/or the polarization of the target which is transferred to the produced Λ^0 hyperon.

The analysis presented in this thesis is focused mainly on measurements of the longitudinal Λ^0 polarization where the transfer of the polarization from the beam to the Λ^0 is studied. Various model predictions for the longitudinal Λ^0 polarization are presented in subsection 2.2.1. In subsection 2.2.2 models for Λ^0 polarization induced by a transversely polarized target are discussed. Such transverse polarization data are shown to give access to the transversity distribution, which is the single leading-order parton distribution function which remains largely unmeasured [12].

2.2.1 Longitudinal Λ^0 Polarization

The physical processes giving rise to longitudinal Λ^0 polarization are different depending on the kinematic domain considered. On the one hand there are models predicting a non-zero longitudinal Λ^0 polarization in the current fragmentation region ($x_F > 0$). In such models the polarization of the Λ^0 originates from the polarization of the struck quark and to the extent to which the Λ^0 spin can be attributed to the flavor of the struck quark [8]. On the other hand, models predict that in the target fragmentation region ($x_F < 0$) longitudinal Λ^0 polarization originates from the polarization of strange quarks in the sea of quark-antiquark pairs [4]. More recent models try to combine the two production mechanisms into one approach [18]. Below these three approaches are discussed separately. In each case, an assessment of their impact on the measurements performed at the HERMES experiment is also presented.

Λ^0 polarization in the current fragmentation region

The commonly assumed mechanism leading to longitudinal Λ^0 polarization is shown in figure 2.4. When the incoming lepton beam is polarized the virtual photon exchanged in the scattering process is also polarized and interacts with quarks in the nucleon of opposite spin orientation. The spin of each particle is indicated by open arrows in figure 2.4. When hyperons are formed from the struck quark (i.e. in the current fragmentation domain) they are polarized if the scattered quark flavor is one of the significant carriers of the Λ^0 spin.

A more detailed discussion is given in [5] of which the key elements are reproduced here. The induced polarization of the struck quark (P_q) is related to the polarization of the beam leptons (P_b) via the relation:

$$P_q = P_b D(y), \tag{2.11}$$

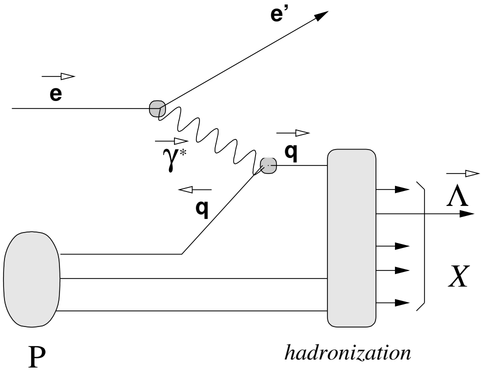

Figure 2.4: A schematic representation of the spin (indicated with the arrows) transferred from the polarized lepton beam to the produced Λ^0 hyperon (picture taken from [5]).

where the depolarization factor

$$D(y) = \frac{1-(1-y)^2}{1+(1-y)^2} \tag{2.12}$$

is accounting for the loss of polarization of the virtual photon as compared to that of the incident lepton. The induced longitudinal Λ^0 polarization is then given by:

$$P^{\Lambda}_{L'} = P_b D(y) D^{\Lambda}_{LL'} \tag{2.13}$$

where $D^{\Lambda}_{LL'}$ is the spin transfer coefficient describing the probability that the polarization of the struck quark, oriented along the virtual photon direction L, is transferred to the Λ^0 along the quantization axis L'.

The measurement of the spin transfer coefficient $D^{\Lambda}_{LL'}$ is of great interest because it can be related to the unknown spin-dependent fragmentation function[1] $G^{\Lambda}_{1,f}$ and the known spin-independent fragmentation function $D^{\Lambda}_{1,f}$ as follows [8]:

$$D^{\Lambda}_{LL'}(z,x,Q^2) = \frac{\sum_f e_f^2 q_f(x,Q^2) G^{\Lambda}_{1,f}(z,Q^2)}{\sum_f e_f^2 q_f(x,Q^2) D^{\Lambda}_{1,f}(z,Q^2)}, \tag{2.14}$$

where q_f are the unpolarized quark distribution functions inside the nucleon and e_f represents the charge of the quarks of flavor f over which is summed.

---

[1] The spin-dependent and spin-independent fragmentation function are also sometimes referred to as $\Delta\hat{q}_\Lambda$ and $\hat{q}_\Lambda$, respectively [8].

Because both the quark distribution functions and the Lambda fragmentation functions vary slowly with Q^2 one can approximate their Q^2 dependence by evaluating the function at the average $\langle Q^2 \rangle$. Under these conditions the x-dependence can be isolated, enabling an integration over x:

$$
\begin{aligned}
D^{\Lambda}_{LL'}(z)_{\langle Q^2\rangle} &\simeq \sum_f \frac{G^{\Lambda}_{1,f}(z)}{D^{\Lambda}_{1,f}(z)} \int \frac{e_f^2 q_f(x) D^{\Lambda}_{1,f}(z)}{\sum_{f'} e_{f'}^2 q_{f'}(x) D^{\Lambda}_{1,f'}(z)} dx \qquad (2.15)\\
&= \sum_f D^{\Lambda}_{LL',f}(z)\omega^{\Lambda}_f(z), \qquad (2.16)
\end{aligned}
$$

where $D^{\Lambda}_{LL',f}(z) = G^{\Lambda}_{1,f}(z)/D^{\Lambda}_{1,f}(z)$ is the partial spin transfer from a struck quark of flavor q to a Λ^0 hyperon and the purity ω^{Λ}_f is defined as the net probability that a Λ^0 was produced after a quark of flavor f was struck. Equation 2.16 is essentially based on the following three assumptions: (i) that the produced Λ^0 hyperon contains the struck quark of flavor f, (ii) that the Λ^0 hyperon was produced directly and not via the decay of a heavier hyperon, and (iii) that the original helicity of the quark is preserved during the fragmentation process. The partial spin transfer coefficient can be further simplified if it is realized that the Λ^0 fragmentation functions are proportional to the quark distribution functions for the same quark flavor in the Λ^0 hyperon [19]. This is due to the fact that the probability to produce a (polarized) Λ^0 hyperon starting from a (polarized) quark of flavor f is proportional to the probability to find such a quark in the Λ^0, i.e. the (spin-dependent) quark distribution function (Δ) q^{Λ}_f:

$$
D^{\Lambda}_{LL',f} \equiv \frac{G^{\Lambda}_{1,f}}{D^{\Lambda}_{1,f}} \simeq \frac{\Delta q^{\Lambda}_f}{q^{\Lambda}_f}. \qquad (2.17)
$$

Here, $\Delta q^{\Lambda}_f / q^{\Lambda}_f$ can be interpreted as the average polarization of quarks of flavor f in the Λ^0 hyperon. Because of the u quark dominance relation 2.15 can be further simplified for deep-inelastic lepton scattering off the proton as:

$$
D^{\Lambda}_{LL'} \approx \frac{\Delta q^{\Lambda}_u}{q^{\Lambda}_u}. \qquad (2.18)
$$

This leads to the conclusion that measurements of the spin transfer coefficient can be used as a probe of the non-strange components of the Λ^0 spin structure. In the naive Constituent Quark Model the spin of the Λ^0 is entirely due to the spin of the s quark, $\Delta s_{\Lambda} = 1$, while the u and d quarks do not contribute to the Λ^0 spin, i.e. $\Delta u_\Lambda = \Delta d_\Lambda = 0$. This leads to the prediction $D^\Lambda_{LL'} \simeq 0$. There are various model calculations which predict different values for the spin contributions of the s quark and the u and d quarks in the Λ^0. One example is the estimate by Burkardt and Jaffe [20] which is based on SU(3)-flavor symmetry in conjunction with experimental results on the proton with which they obtained $\Delta q^\Lambda_u = \Delta q^\Lambda_d = -0.23 \pm 0.06$ and $\Delta q^\Lambda_s = 0.58 \pm 0.07$. This estimate attributes a much more important role to the spin of the u and d quarks as carriers of the spin of the Λ^0. A more complete overview of the various predictions is given in [5].

In a recent HERMES publication[2] [5] measurements of the longitudinal spin transfer coefficient $D^\Lambda_{LL'}$ are presented and compared with results from the NOMAD [6] and E665 [7] experiments.

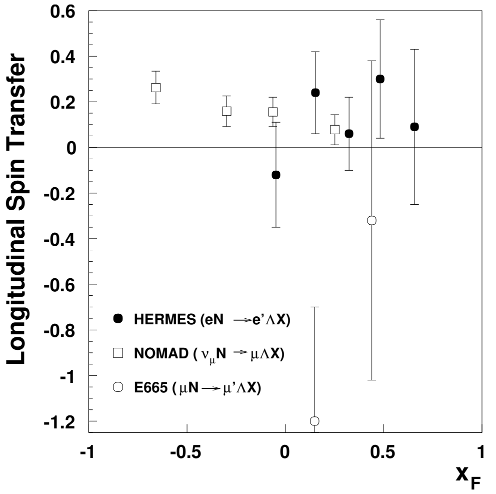

Figure 2.5: The dependence of the longitudinal spin transfer coefficient ($D^\Lambda_{LL'}$) on x_F [5]. The error bars are statistical only. The results from the HERMES, NOMAD and E665 experiments are shown.

In these measurements a small value of $D^\Lambda_{LL'}$ is observed which is in agreement with the model calculations predicting a small contribution of the u and d quarks to the spin of the Λ^0 hyperon. The HERMES measurements are also found to be in agreement with the NOMAD measurements and the less precise E665 data.

However, several remarks have to be made about these measurements. Not all detected Λ^0 hyperons are directly produced from the fragmentation of quarks. Some Λ^0 hyperons may also originate from heavier hyperons like Σ^0, Σ^* and Ξ hyperons decaying into a Λ^0 hyperon. A detailed study of this

---

[2] These measurements are based on the data taking period 1999-2000 and supersede the previously published data [21], which were based on the 1996 and 1997 data. The older data set is included in the more recent data set.

subject can be found in [9] where it is concluded that up to $\sim 50\%$ of the Λ^0 hyperons may be the result of heavy hyperon decays. The Λ^0 hyperons originating from decays of heavier hyperons may be polarized if their parents were polarized. For example the polarization of the Σ^0 hyperon, responsible for 38% of the yield of indirectly produced Λ^0 hyperons in the HERMES spectrometer [9], is transferred to the Λ^0 hyperon as $P_\Lambda = -1/3 P_{\Sigma^0}$ [22]. As the polarization of individual hyperons produced in DIS is unknown, the presently observed small Λ^0 polarization can either be the result of cancellations between polarization values of successive hyperons or the result of a dilution masking a larger intrinsic polarization. These problems can be circumvented by using (presently non-existing) experimental results on Σ^0, Σ^* and Ξ polarization and the results of [9] to correct the data. Moreover it is also important to compare data from different experiments with different admixtures of target remnant effects in order to assess to what extent such effects are important.

Λ^0 polarization in the target fragmentation region

In contrast to the current fragmentation region, where the Λ^0 hyperon is formed from the struck quark, the target fragmentation region describes Λ^0 hyperons which are formed from the remnant diquark. The model for this process described in [4] attributes the polarization of these Λ^0 hyperons to the polarization of a residual strange quark in the sea of quark-antiquark pairs of the nucleon. As was shown in figure 2.4 polarized Λ^0 hyperons can also be produced in the target fragmentation region when a polarized beam is used. If it is assumed that the spin of the Λ^0 hyperon is mostly carried by the (valance) strange quark a measurement of the Λ^0 polarization in the target fragmentation region can provide information on the correlation between the relative orientation of the spin of the strange quarks and that of the struck quark in the nucleon. This is expressed in a spin-correlation coefficient C_{sq} defined as:

$$C_{sq} = \frac{P_{s+q} - P_{s-q}}{P_{s+q} + P_{s-q}} \tag{2.19}$$

where $P_{s\pm q}$ is the probability that the longitudinal projection of the remnant s quark spin is parallel/anti-parallel to that of the struck quark q.

In [4] the polarization of the remnant s quark is shown to be:

$$P_{s_{rem}} = \frac{\sum_q e_q^2 [P_T \Delta q(x) - P_B D(y) q(x)] C_{sq}}{\sum_q e_q^2 [q(x) - P_B P_T D(y) \Delta q(x)]}, \tag{2.20}$$

where P_T and P_B are the longitudinal polarization of the target and the beam, respectively. In case of an unpolarized target ($P_T = 0$) and assuming u-quark dominance this equation simplifies to:

$$P_{s_{rem}} = -P_B D(y) C_{su}. \tag{2.21}$$

An additional correction needs to be applied to take into account the effect of Λ^0 hyperons originating from heavier hyperons. For this purpose a dilution factor D_F is introduced which reduces the observed polarization of the Λ^0 hyperon:

$$P_\Lambda = D_F P_s. \tag{2.22}$$

This equation also reflects the aforementioned assumption according to which the Λ^0 spin is entirely attributed to the constituent strange quark. In this way the measured polarization of the Λ^0 can be related to the spin-correlation coefficient C_{su} that provides information on the relative orientation of u and s quarks in the nucleon:

$$P_\Lambda = -D_F P_B D(y) C_{su}. \tag{2.23}$$

Using this equation experimental values for C_{su} can be derived from Λ^0 polarization measurements. The results of such studies can be compared to two model predictions for C_{su}. On the basis of [4] two extreme predictions for C_{su} can be given:

- With reference to figure 2.6 it can be shown that if the nucleon (target) spin is mainly carried by the u quark, while the $q\bar{q}$-sea quark pairs have the vacuum quantum numbers, one expects $C_{su} \simeq -1$.
- If on the other hand gluons are a dominant carrier of nucleon spin, one expects $C_{su} \simeq 0$ as can be seen from figure 2.7 taken from [4]. Please note that in experiments with unpolarized targets both nucleon spin orientations, of which only one is shown, contribute equally. Hence, both gluon orientations are equally important despite the fixed beam polarization. This results in $C_{su} \simeq 0$.

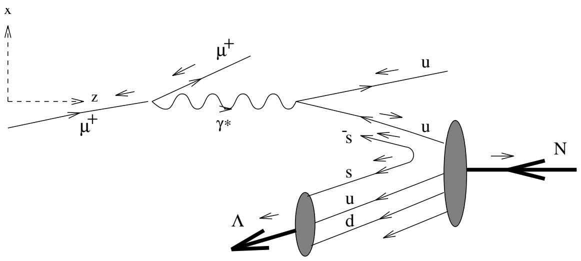

Figure 2.6: Dominant diagram for Λ^0 production in the target fragmentation region in deep-inelastic μN scattering from a valance u quark [4]. The same diagram also applies to eN scattering.

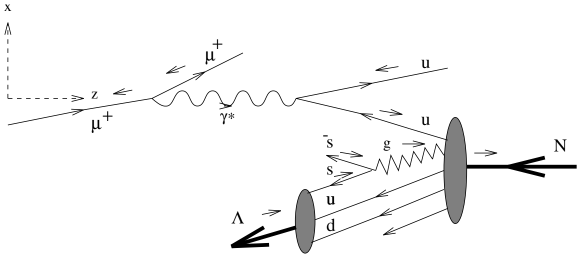

Figure 2.7: The same diagram as in figure 2.6 but under the assumption that gluons are the dominant carrier of the nucleon spin.

Unifying model

While the models discussed above focus exclusively on the target or current fragmentation regions, in a more recent approach described in [18] the models described above are merged into one prediction. The distinction between current and target fragmentation is still preserved and determined from the LUND Monte Carlo used in this study. The model described above in the current fragmentation is used when the struck quark is contained in the produced Λ^0 hyperon or when the struck quark is contained in a heavier hyperon which decays into a Λ^0 hyperon. The polarization of the Λ^0 produced promptly or via the decay of a heavier hyperon Y is calculated from the quark polarization P_q as

$$P_\Lambda^q(Y) = -C_q^\Lambda(Y) P_q \tag{2.24}$$

where $C_q^\Lambda(Y)$ is called the spin transfer coefficient and is calculated for various possible production mechanisms and given in table 2.1. The negative sign is the result of the opposite spin orientation of the incoming and outgoing quark.

Λ^0 parent	C_u^Λ	C_d^Λ	C_s^Λ
quark	-0.18	-0.18	0.63
Σ^0	-0.12	-0.12	0.15
Ξ^0	0.07	0.05	-0.37
Ξ^-	0.05	0.07	-0.37

Table 2.1: The spin transfer coefficient used in equation 2.24 to calculate the Λ^0 polarization from the polarization of the struck quark taken form [18].

The model by Ellis et al. [4] for the Λ^0 polarization in the target fragmentation region has also been updated in [18]. Using a non-relativistic SU(6) quark-diquark wave function the polarization of Λ^0 hyperons originating from the Σ^0, Σ^{*+} and Σ^{*-} hyperons is expressed in terms of the spin correlation coefficient C_{sq} and the polarization of the struck quark P_q:

$$
\begin{aligned}
P_\Lambda(\text{prompt}) &= C_{sq} \cdot P_q && (2.25)\\
P_\Lambda(\Sigma^0) &= \frac{1}{3} \cdot \frac{2 + C_{sq}}{3 + 2C_{sq}} \cdot P_q && (2.26)\\
P_\Lambda(\Sigma^{*+}) = P_\Lambda(\Sigma^{*-}) &= -\frac{5}{3} \cdot \frac{1 - C_{sq}}{3 - C_{sq}} \cdot P_q. && (2.27)
\end{aligned}
$$

The spin correlation coefficient is not fixed in this new approach but obtained from a fit of the NOMAD data. Furthermore the spin correlation coefficient is taken to be different when the struck quark is a valance quark or a sea quark and also other values of C_{sq} are possible. The approach in [23] considers an equal probability of the spin projections $S_z(\bar{s}s) = -1$ and $S_z(\bar{s}s) = 0$ which results in $C_{sq} = -1/3$.

Two different approaches are taken in the LUND Monte Carlo to judge whether the struck quark or remnant diquark is contained in the hyperon[3]. These two requirements yield similar results for the spin correlation coefficient for scattered valance quarks $C_{sq_\text{val}} = -0.35 \pm 0.05$ and $C_{sq_\text{val}} = -0.25 \pm 0.05$, respectively. Both results are obtained from a fit of the NOMAD data. However the results differ substantially if a sea quark is struck, $C_{sq_\text{sea}} = -0.95 \pm 0.05$ and $C_{sq_\text{sea}} = 0.15 \pm 0.05$. As it is assumed that the scattering off sea quarks is negligible in lepton-nucleon DIS, only the two fitted C_{sq_val} values are both considered in the following.

The combination of the two models for Λ^0 polarization in the target and

---

[3] In [18] these two approaches are named model A and model B where the difference lies in the selection of so called rank counters R_q and R_{qq} which correspond to the particle rank from diquark and quark ends of the string in the LUND MC.

current fragmentation is particularly useful when comparing to the HERMES data as the requirement $x_F > 0$ does not exclude Λ^0 hyperons which are formed from the remnant diquark. The result for the two approaches (with the two fitted $C_{sq_{\rm val}}$ values) are shown in figure 2.8 where the calculations are performed for the HERMES kinematics. In this figure the Λ^0 spin transfer is defined as $P_\Lambda/P_B D(y)$, is presented for both approaches. The data points for HERMES were published in [5] and are in agreement with the presented models. The differences between the two model predictions are small.

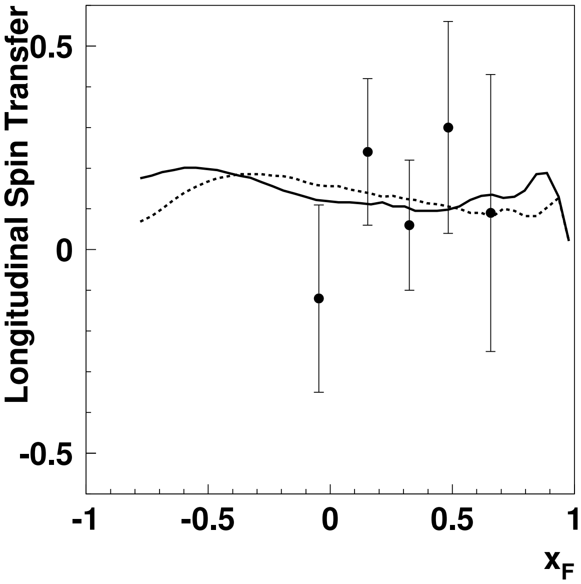

Figure 2.8: Predictions for two models based on the LUND MC for the spin transfer, $P_\Lambda/P_B D(y)$, to Λ^0 hyperons produced in e^+ DIS interactions as a function of x_F [18]. The data points are from [5].

The unified model of [5] is seen to be in agreement with the HERMES data, thus confirming the relatively small value of C_{sq} derived from the NOMAD data. The precision of the HERMES data is such that it cannot be excluded that the gluon polarization model ($C_{sq} \simeq 0$) contributes as well. The important observations about the spin of the nucleon needs to be verified with independent experiments designed to measure the polarization of gluons in the nucleon and that of the Λ^0 preferably at lower x_F values where the sensitivity to C_{sq} increases.

2.2.2 Transverse target Λ^0 Polarization

In the previous subsection the Λ^0 polarization induced by a longitudinal polarized beam was discussed. It is also of interest to measure the Λ^0 polarization arising from the use of a transversely polarized target. In a paper by

Jaffe [8] the Λ^0 polarization due to a transversely polarized target is given by:

$$\vec{P_\Lambda} = \vec{P_N} D(y) \frac{\sum_f e_f^2 h_{1,f}(x,Q^2) H_{1,f}^\Lambda(z,Q^2)}{\sum_f e_f^2 f_{1,f}(x,Q^2) D_{1,f}^\Lambda(z,Q^2)} \tag{2.28}$$

where h_1 is the largely unexplored (leading-order) transversity distribution and H_1^Λ is the unknown transverse fragmentation function. The arrows indicate that the direction of the Λ^0 polarization quantization axis is taken to be parallel to the polarization direction of the transverse target. If u quark dominance is assumed this equation reduces to:

$$\vec{P_\Lambda} = \vec{P_N} D(y) \frac{h_{1,u}(x,Q^2) H_{1,u}^\Lambda(z,Q^2)}{f_{1,u}(x,Q^2) D_{1,u}^\Lambda(z,Q^2)}. \tag{2.29}$$

A measurement of the Λ^0 polarization on a transversely polarized target thus provides a value of the product of the transversity distribution function in the nucleon and the corresponding transverse Λ^0 fragmentation function. This model applies in the current fragmentation region.

Any possible measurement of the transversity distribution is of great importance since this distribution function is the only unexplored leading-order function. Only since a few years experiments are starting to provide information on transversity. These experiments [12, 13] have raised considerable interest as transversity gives independent information in the tensor charge of the nucleon, the role of relativity and Q^2 rescaling [24]. Three methods were suggested to study transversity in DIS. The first is the measurement of single spin asymmetries of semi-inclusively produced hadrons off a transversely polarized target which has led to the results discussed in a recent HERMES publication [12]. The second method uses similar single spin asymmetries but with the detection of a pion pair and is discussed in [13]. The third method, which was described above, is still unexplored in the HERMES experiment and will be discussed in this thesis.

2.3 Summary

In this chapter the theoretical framework for Λ^0 polarization measured in DIS is discussed. With the development of a new detector, the Lambda Wheels, the Λ^0 yield at HERMES is increased and an extension of the data towards smaller values of x_F is expected. With these new measurements three subjects can be addressed:

- the spin structure of the Λ^0 can be studied on the basis of measurements of the longitudinal Λ^0 polarization in the current fragmentation region;
- the relative orientation of the spin of the s quark with respect to the spin of the u quark in the target nucleon can be obtained by measuring the longitudinal Λ^0 polarization in the target fragmentation region;
- independent information on transversity can be provided by measuring the polarization of the Λ^0 in a direction parallel to a transversely polarized target in the current fragmentation region

Although a few measurements exist on each of these three subjects, in all cases the data are scarce, usually carry large error bars, and are subject to substantial systematic uncertainties (e.g. the lack of Λ^0 purity corrections). It is the purpose of the data presented in this thesis to provide additional Λ^0 data on these subjects using a new instrument, the Lambda Wheels, in a somewhat different kinematic domain.

Chapter 3

The HERMES experiment

The analysis discussed in this thesis is based on measurements performed at the HERMES (HERa MEasurement of Spin) experiment during the year 2004. This experiment is located inside the HERA accelerator complex at the DESY (Deutsches Electronen-SYnchrotron) institute in Hamburg, Germany. The HERA accelerator consists of two storage rings with a circumference of 6.3 km each containing a beam of leptons in one and protons in the other ring. Typically, the beams have currents of 100 mA or more for protons and up to 40 mA for leptons. The beams are accelerated to an energy of 920 GeV and 27.5 GeV, respectively.

The HERA facility accommodates four experiments which are located in separate halls positioned at the four quarters of the compass. The HERMES experiment, located in the East Hall, makes use of the lepton beam only. This beam consists of either electrons or positrons which are scattered off a gas target. In the year 2004 a positron beam was used. The two experiments located in the North and the South Hall, H1 and ZEUS, are collider experiments and have their spectrometers positioned around an interaction point of the two beams. The experiment in the West Hall, HERA-B, made use of the proton beam which interacted with movable metal wires. This experiment was concluded in March 2003 after which it was disassembled and removed from the West Hall.

The HERMES experiment was designed to study the internal spin structure of the nucleon. A polarized beam and target are needed for this purpose. The lepton beam is spontaneously polarized in the transverse direction through the Sokolov-Ternov [25] effect and can reach a maximum polarization of about 60% [26]. This polarization is measured by a polarimeter located in the West side of the ring. To study the nucleon spin the spin direction of the lepton beam has to be rotated in the longitudinal direction before it enters the HERMES experiment [27]. At 52 m behind the HERMES target the longitudinal polarization is also measured [28] after which the spin is rotated back in the transverse direction in order to maintain the polarization in the rest of the ring.

Like every fixed target experiment the setup is divided in mainly three parts: the target (described in section 3.1), the spectrometer with its various characteristics (section 3.2) and a trigger and readout system (section 3.3). This chapter is concluded with a discussion on the data production and analysis techniques (section 3.4) and a short description of the Monte Carlo simulations employed by the HERMES experiment (section 3.5).

3.1 Target

The data used in the analysis described in this thesis are collected with both polarized and unpolarized target gasses. The various components of the target which make this possible are briefly discussed here.

When the target is in the polarized mode [29] an atomic beam source (ABS) injects nuclear-spin polarized H atoms into the target cell where areal densities of about 10^{14} nucl/cm^2 are reached. This cell consists of a 75 μm thick, 400 mm long, pure aluminium tube which has an elliptical cross-section of 21×8.9 mm^2. The nuclear polarization of the gas in the cell is measured via a sampling tube by a Breit-Rabi Polarimeter (BRP). This sampling tube is also used by the Target Gas Analyzer (TGA) which measures the relative atomic and molecular content of the gas. A transverse magnet with a field strength of about 300 mT provides a holding field which defines the polarization axis and prevents spin relaxation of the polarized gas[1]. The field map of this magnet is shown in figure 3.1. Here, the field strength along the vertical direction (B_y) is shown versus the z position. The different curves represent the field strength at various x positions in the horizontal plane. The vertical lines indicate the position of the Lambda Wheels (LW) detector which is further discussed in section 3.2.1 and chapter 4.

In unpolarized mode the transverse target magnetic field is switched off and gas is injected into the target cell using the Unpolarized Gas Feed System (UGFS) [30]. This system is capable of injecting various unpolarized gasses like ^{1}H, ^{2}H, ^{4}He, ^{14}N, ^{20}Ne and ^{84}Kr into the target cell. The total areal densities can be varied between 10^{14} and 10^{16} nucl/cm^2. The higher target densities are used for 'end-of-fill' running. In this mode the beam lifetime is decreased from typically 45 hours for polarized ABS operation down to 1 hour or less near the end of a fill of the HERA storage rings, typically after 10-12 hours of normal data taking. This enables operation with a beam

---

[1] Prior to 2002 a longitudinal holding field of 350 mT was used.

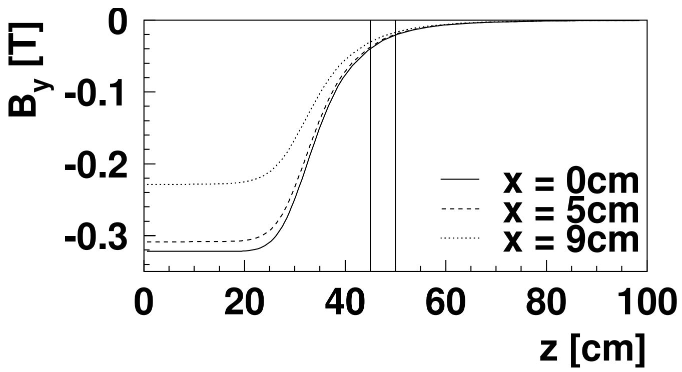

Figure 3.1: The fieldmap of the tansverse target magnetic field where the different curves represent the field strength at various x positions in the horizontal plane. The x, y, z coordinates are defined in section 3.2.

current of 10 mA or less and a high density target where a large amount of unpolarized data can be taken in a short amount of time.

3.2 Spectrometer

The HERMES spectrometer [31] is an open forward angle magnetic spectrometer which is up/down symmetric around the horizontal plane defined by the accelerator ring. The angular acceptance in the vertical direction is limited by the front field clamps of the spectrometer magnet and the steel plate which shields the lepton and proton beam from the field of the spectrometer magnet. This results in an acceptance of $\pm(40-140)$ mrad in the vertical direction and ±170 mrad in the horizontal plane. The spectrometer magnet has a deflecting power of $\int B\mathrm{d}l = 1.3$ Tm bending the tracks of charged particles in the horizontal plane. This together with the tracking detectors makes the determination of the momentum possible. The coordinate system is determined by the lepton beam which defines the z-axis, the vertical direction defines the y-axis pointing upward, the x-axis is put in the horizontal plane to make a right-handed coordinate system of which the origin is located in the middle of the target cell.

The two main features of this spectrometer are the tracking system and the detectors which are used for particle identification, both shown in figure 3.2. These two detector types are discussed in the subsections below followed by descriptions of the radiation protection system and the luminosity monitor at the end of the section.

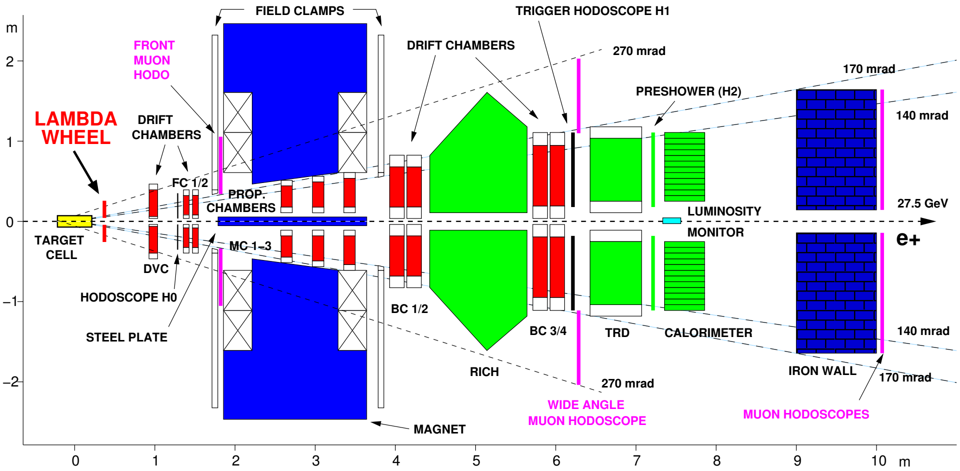

Figure 3.2: Side view of the HERMES spectrometer with the tracking detectors in medium grey (LW, DVC, FC, MC, BC) and the detectors for particle identification in light grey (RICH, TRD, PRESHOWER, CALO).

3.2.1 Tracking

This subsection gives a brief description of the detectors which register the track of the scattered particles. The tracking detectors can be divided in three groups: the front tracking, consisting of the Lambda Wheels (LW), Drift Vertex Chambers (DVC) and Front Chambers (FC), the part in the spectrometer magnet, where the Magnet Chambers (MC) are located and the detectors behind the spectrometer magnet which are the Backward Chambers (BC). Except for the LW, which is a silicon strip detector, all other tracking detectors are wire chambers, consisting of several planes of parallel strung wires aligned vertically or tilted at an angle of ±30 degrees with respect to the vertical direction. To resolve the left-right ambiguities each chamber is equipped with two sets of planes with a certain orientation, where the second plane with the same orientation is shifted by half a wire distance. The planes with vertically aligned wires determine the x-position of the track, the tilted planes measure also the vertical position and together with the position of the planes in the z-direction the track can be reconstructed. The tracking algorithms, which are applied to the data taken with these detectors are described in section 4.3.

The detectors closest to the target at a distance of 45 cm from the middle of the target cell are the Lambda Wheels [32]. This detector is at the basis of the analysis presented in this thesis and will be described in detail in chapter 4. For this detector system a special tracking algorithm was developed which is described in section 4.3.2. The tracks which are reconstructed with this special tracking algorithm are called LW tracks. Further downstream of the lepton beam the DVC [33] is located at $z = 1.1$ m. It consists of two drift chambers containing six planes of wires each with a drift cell size of 6 mm. The next tracking detector is the FC [34] which is closest to the magnet field clamp at $z = 1.5$ m. It is composed of four drift chambers containing six planes each with a cell size of 7 mm.

In the spectrometer magnet the MC tracking chambers are located [35]. These are multi-wire proportional chambers with a cell size of 2 mm. There are six chambers with three planes each. This detector is especially important for the detection of low momentum particles which are bent out of the acceptance of the detectors behind the spectrometer magnet. The tracks of such particles are called short tracks.

Behind the spectrometer magnet the BC is located [36]. It is composed of eight drift chambers of which four are located before and four after the Ring Imaging Čerenkov (RICH) detector. Each chamber has six planes with a cell size of 15 mm. When particles produce a hit in these BC chambers it is possible to reconstruct the track throughout the whole detector. These tracks are called long tracks.

The HERMES tracking algorithm and performance are further discussed in section 4.3.1.

3.2.2 Particle Identification Detectors

In HERMES Particle Identification (PID) is accomplished by the use of four detectors: the Ring Imaging Čerenkov detector (RICH), the Transition Radiation Detector (TRD) and preshower-hodoscope counter combined with the electromagnetic calorimeter (CALO). The latter three are designed to make a clear separation between scattered beam leptons and hadrons coming from the scattering process. The RICH is designed to determine the hadron type and can make a distinction between pions, kaons and protons.

The four PID detectors are located behind the spectrometer magnet. The RICH [37] is the one closest to the magnet. This detector is based on the fact that charged particles emit Čerenkov light when they have a speed in a medium which is larger than the speed of light in that medium. In the RICH the particles first traverse a wall of aerogel tiles before they enter a volume filled with C_4F_{10} gas in which spherical mirrors reflect the emitted Čerenkov light towards a PMT matrix. This matrix has a fine enough granularity to measure the ellipsoid shape of the light cones from which the angle between the propagation direction of the particle and the light front can be determined. These opening angles are shown in figure 3.3 for pions, kaons and protons for the two media, separately, as obtained from a Monte Carlo. Together with the momentum measured by the tracking detectors a separation between these various hadrons is made possible.

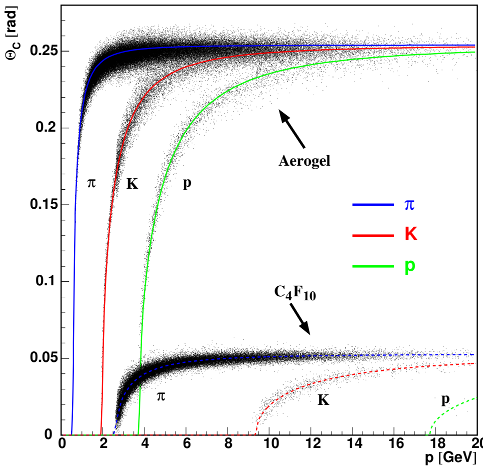

Figure 3.3: The opening angle of the Čerenkov light measured by the RICH for pions, kaons and protons in the aerogel (upper bands) and C_4F_{10} (lower bands) media. The data points are obtained from a Monte Carlo.

While the RICH can determine the hadron type of a particle, the TRD is needed to separate the leptons from the hadrons. It is based on the measurement of transition radiation which is emitted when a charged relativistic particle crosses a boundary between media of different dielectric constants. The mean energy of this radiation is in the range of X-ray photons and is directly proportional to the Lorentz factor γ. Beam leptons have very large values of γ (i.e. larger than 6000) while hadrons have a much lower value of γ (i.e. less than 200). The TRD is equipped with a radiator medium of polyethylene/polypropylene fibers arranged in a plane to make a module of 6.35 mm thickness. This is followed by a multi-wire proportional chamber filled with a mixture of 90% Xe and 10% CH_4 gas. It is because Xe has a short absorption length for soft X-rays that the chamber is sensitive to the detection of transition radiation.

The last PID detector system consists of the preshower detector and the electro-magnetic calorimeter [38]. The preshower detector is composed of 1 cm lead and 1 cm plastic scintillator and is placed directly in front of the CALO. Because 1 cm of lead corresponds to 0.064 nuclear interaction lengths the signal produced by hadrons through the strong force will be typically minimum ionizing, around 2 MeV, while beam leptons, which interact through the electromagnetic force, have a mean deposited energy of about 20-40 MeV because the radiation length is 1.8 for lead. The CALO is composed of $9 \times 9 \times 50$ cm^3 lead glass blocks which can fully contain an electromagnetic shower, while hadrons only deposit a fraction of their energy.

These lead glass blocks are stacked in two sets of 42 columns containing 10 blocks each placed in the top and bottom half of the spectrometer. Together with the momentum measurement the determination of the E/p ratio can distinguish leptons from hadrons.

3.2.3 Beam Loss Monitor

Just behind the DVC the Beam Loss Monitor (BLM) is positioned [39]. This is a radiation protection system to prevent damage due to high levels of radiation induced by the lepton beam. Excessive radiation could damage the target cell and the electronics of the LW. The BLM consists of two sets of 4 small ($4 \times 4 \times 1.3$ cm^3) ionization chambers filled with Ar gas. They are placed in the horizontal plane at either side of the beam at a distance of 6 cm from the beam line. These ionization chambers measure the radiation induced by the lepton beam and can trigger the beam kicker magnet when the radiation exceeds a set threshold after which the beam is dumped in a controlled way. Since the radiation during injections of the lepton beam exceed the set threshold, the kicker magnet trigger is vetoed during injections. However, because the signal from the ionization chambers is recorded with an ADC during a 100 ms time window around the trigger it is possible to monitor the accumulated radiation during these injections. During data taking in the year 2004 the BLM triggered a beam dump in about half a dozen cases. All triggers were clearly due to high levels of beam induced radiation which were mostly caused by a failure in the RF control system of the accelerator[2].

3.2.4 Luminosity monitor

A luminosity measurement enables a comparison of data collected on different target gasses or spin states or entirely different experiments. The luminosity is defined as the product

$$L = \Phi_{beam} \cdot N_{targ} \tag{3.1}$$

of the flux of beam particles Φ_{beam} and the number of target atoms inside the cross section of the beam N_{targ}. For the measurement of the luminosity at HERMES the elastic scattering of the beam leptons with the electrons of the target atoms is used. This scattering is referred to as Bhabha scattering ($e^+e^- \rightarrow e^+e^-$) with the associated annihilation of the e^+e^- pair into

---

[2] Information obtained from the machine operators.

photon pairs ($e^+e^- \to \gamma\gamma$) in case of a positron beam, and Møller scattering ($e^-e^- \to e^-e^-$) in case of an electron beam. The luminosity detector is placed at $z = 7.2$ m [40]. The scattered particles and photons are detected in two sets of radiation hard $NaBi(WO_4)_2$ crystals placed on the left and right side of the beam in a 3×4 configuration. To separate background events from the scattering processes of interest as described above, the requirement of two coincident signals in both calorimeter sets with an energy deposited above 5 GeV, has to be fulfilled.

3.3 The trigger and readout system

The HERMES spectrometer is equipped with a single level trigger system which initiates the full readout of all detector signals for each event. The most important trigger in HERMES is the DIS trigger which is based on coincident signals in all three top or bottom Hodoscopes[3] and a summed signal of two adjacent columns of scintillators in the CALO which has to exceed an adjustable threshold. Various other triggers are implemented for different physics analyzes and for calibrating and monitoring the spectrometer components.

When a trigger initiates the readout of the detector a certain time is needed to complete this readout. During this period no trigger can initiate the readout of the next event. This period of time is called dead time and depends on the speed of the readout. This dead time is reduced at HERMES through a system of double buffering which enables the readout of the next event while the incoming event is processed. The goal of a proper trigger system is to accept as many triggers of physical interest as possible and disregard most background events. This causes the overall trigger rate to decrease and minimizes the dead time. An example of such a trigger condition as used in HERMES is the requirement of a coincidence with the bunch crossing of the lepton beam, also called the HERA clock. Under normal operating conditions the HERMES trigger and readout system accepts up to 500 events per second with dead times less than 10%.

The detector signals are read out by the HERMES Data AcQuisition (DAQ) system composed of ADCs and TDCs which digitize the analog detector signals and stores this information in an EPIO (Experimental Physics Input Output Package [41]) data format. The data are structured in events which is the smallest possible data structure.

---

[3] These are three plastic trigger scintillators: H0 located just in front of the FC before the spectrometer magnet, H1 in front of the TRD at the back side of the spectrometer and H2 also known as the preshower counter in front of the CALO, see also fig 3.2.

3.4 Data production and analysis

Before the detector signals can be used for a physics analysis a long chain of intermediate steps have to be taken. A schematic drawing of the sequence of steps is shown in figure 3.4.

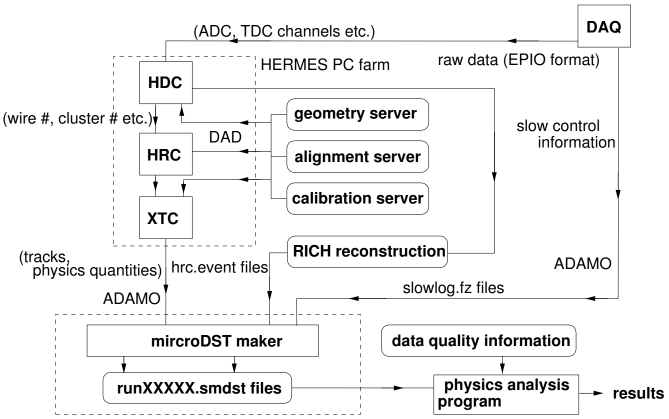

Figure 3.4: A schematic drawing of the offline data production chain.

The raw EPIO data are stored in files of 450 MB called runs. These files are processed with the HERMES DeCoder (HDC) which converts the detector signals from ADC and TDC values into hits, energies etc. This is done by accessing DAD (Distributed Adamo Database) servers which contain the geometry, alignment and calibration of all the detector components. When the detector information is decoded it is ready for the main tracking algorithm called HERMES Reconstruction Code (HRC). This code reconstructs tracks from the hits in the tracking detectors (see also section 4.3.1). After HRC the data are passed on to the tracking code for events with data from the LW which is called the eXtended Tracking Code (XTC, section 4.3.2). All this information is stored in an ADAMO (Aleph Data Model [42]) database format.

Apart from the regular DAQ, which records the physics events, there is also a slow-control system which reads out the detector status like high voltage, pressure, temperature, etc every 10 s. This information is synchronized and merged with the events in the ADAMO database in the final step of the chain, the production of μDST files. In this final step also the PID algorithm is included. The output of this data production step is also in ADAMO format containing all possible information on the particle track, type, charge, energy etc and various other variables such as beam and target polarization, luminosity etc. Since the slow-control system records information only every 10 s the events are grouped in what is called bursts which contain all the events within these 10 s. This complete chain of steps is iterated when more precise information on calibration and alignment is available for the DAD servers. The data production used in this thesis is the 04b data which is the first iterated production of 2004 that includes the calibration of the detectors obtained with the 04a data production.

In order to carry out an actual physics analysis the reconstructed tracks have to be identified as originating from particles of a certain type. This together with a discussion on the data quality and the calculation of the luminosity and equivalent number of DIS events is the subject of the following subsections.

3.4.1 Data Quality

To ensure that only those data are used that were collected when all detector components were functioning in a proper way the quality of the data needs to be verified. This is done on the basis of a bit pattern included in the μDSTs for each burst and separately for the top and bottom half of the spectrometer. The bit pattern contains the result of several checks performed on the data. If one of these checks results in the conclusion that these data are not to be used in a physics analysis then the corresponding bit is set to 1. If the data pass the checks then this bit is left zero. In this way the analyzer can judge himself if the checks performed by the data quality software are relevant for the specific analysis he is conducting which may require only a subset of the checks to be fulfilled.

The various bits can be divided into 4 main categories: the target (indicating the target mode, polarized/unpolarized), the beam and luminosity (beam current and polarization, luminosity monitor rate), the DAQ and production (burst length, bad μDST records, dead time) and the spectrometer (HV trips, PID, marked in the logbook as bad data taking).

Apart from the selection criteria on the bursts there are also requirements on single tracks. One of the first checks on the tracks is if they are all within the spectrometer magnet acceptance and do not hit the field clamps of the magnet or the steel plate around the beam pipe. Furthermore, the tracks which reach the back of the spectrometer should be within the active volume of the calorimeter. Note that these track requirements are only applied on tracks reconstructed with the HRC tracking code and do not apply to the tracks reconstructed in the LW which are often outside the standard HERMES acceptance. A last check on the tracks is the rejection of so called ghost tracks. These are tracks which have almost the same track parameters as another track within the same event. In this case one of the tracks needs to be rejected.

When the track passes these restrictions the next step is to determine which type of particle can be associated with the track.

3.4.2 PID

To determine the particle type associated with a given track the four PID detectors: RICH, TRD, Preshower and CALO (described in section 3.2.2) are used in a formalism based on a Bayesian probability analysis. In a first stage these four detectors are combined to separate hadrons and leptons. Each detector has specific distributions, also called parent distributions, which specify the probability of a given detector response for a particle of type i through likelihoods $\mathcal{L}^i$. These likelihoods can be determined for one detector from the measured data by making stringent requirements on the other three PID detectors thus ensuring that only particles of type i have indeed been selected. The quantity which is used in the eventual PID scheme is the probability that a measured detector response originates from a certain particle type. This probability is defined as:

$$P^i = \frac{\phi^i \mathcal{L}^i}{\sum_j \phi^j \mathcal{L}^j} \tag{3.2}$$

where ϕ^i is the flux factor for particle type i and the sum runs over all possible particle types j. The flux factor is defined as the a priori probability that a track originates from a particle with type i for given track parameters. These flux factors are determined from the data in an iterative process which typically converges in less than five steps starting from equal flux factors for hadrons and leptons.

The separation between leptons and hadrons is done by calculating the logarithm of the ratio of the probabilities for leptons (e) and hadrons (h) defined as the PID value for each detector:

$$PID = \log_{10} \frac{P^e}{P^h} = \log_{10} \frac{\mathcal{L}^e}{\mathcal{L}^h} - \log_{10} \frac{\phi^h}{\phi^e}. \tag{3.3}$$

In this way several PID values can be calculated of which only two are used in this analysis, namely:

$$PID_3 = PID_{\mathrm{calo}} + PID_{\mathrm{pre}} + PID_{\mathrm{rich}} \tag{3.4}$$

$$PID_5 = PID_{\mathrm{trd}} = \sum_{i=1,6} PID_{\mathrm{trd},i} \tag{3.5}$$

where the subscripts indicate the specific detector and the sum runs over all 6 individual TRD modules. The sum $PID_3 + PID_5$ is required to be smaller than zero for hadrons and larger than zero for leptons.

After the separation between hadrons and leptons the hadron sample can be divided into pions, kaons and protons using the RICH. This separation is based on the opening angle of the Čerenkov light produced in the two media in the RICH (shown in figure 3.3). The algorithm which determines the particle type also makes use of the track momentum determined by the main tracking code and the measured opening angle. As a result a quality parameter is assigned to each track which is a logarithmic ratio of the largest and second largest PID likelihood as determined by the RICH PID algorithm. When this quality parameter is zero the two likelihoods are the same and the particle remains unidentified. For values larger than zero the particle is identified as the type with the largest likelihood.

3.4.3 Luminosity and DIS

To be able to compare data taken in different years and with different targets the luminosity corresponding to a certain subset of the data needs to be calculated. As described in section 3.2.4 the luminosity monitor measures the rate of elastic scattering events of the beam leptons with the electrons in the target atoms. In the eventual μDSTs this rate is calculated for each burst. To obtain a true luminosity measure one has to multiply this rate with the dead time of the DAQ, the length of the burst, a calibration constant and the ratio of the number of nucleons to electrons of the target atoms. The calibration constant is different for each year and target setup and is determined by the luminosity monitor expert and given on the HERMES data quality web pages [43]. The values calculated by the data quality group for the 2004 data are given below:

target year 2004	luminosity [pb^{-1}]	DIS [10^6]	σ_{DIS} [nb]
polarized H	44.2 ± 1.3	2.224	50.3 ± 1.5
unpolarized D	76.3 ± 1.8	3.312	43.4 ± 1.0

The number of DIS (Deep Inelastic Scattering) events in a data set is also evaluated as it provides an alternative way to compare different data sets. The selection of DIS events requires a strict set of cuts to be fulfilled for the highest momentum lepton in an event:

- charge is the same as the beam charge
- momentum < 28 GeV
- primary vertex in the target cell

- $Q^2 \geq 1$ GeV^2
- $W^2 \geq 4$ GeV^2
- $0.1 \leq y \leq 0.85$

With the numbers given on the HERMES data quality web page the DIS cross section can be calculated for both the polarized and unpolarized data sets the result of which is shown in the table above. One observes a difference in cross sections between H and D that can be attributed to the differing quark content of the nucleons of H and D. The beam positron couples stronger to the u quark, with charge $+2/3$, than to the d quark, with charge $-1/3$. As hydrogen contains more u quarks per nucleon than deuterium, the DIS cross section on hydrogen is larger.

3.5 The HERMES Monte Carlo

The data obtained from the present analysis are compared with a simulation using the HERMES Monte Carlo (MC). The generator used for this MC is PYTHIA 6.225 [44] which generates Λ^0 hyperons in a 4π acceptance. The PYTHIA generator has been extensively tuned to resemble the kinematics observed in the HERMES data [45, 46]. The particles generated with PYTHIA are then tracked by a GEANT MC of the HERMES spectrometer. The GEANT MC simulates the interactions of particles with all materials in the HERMES spectrometer. The GEANT MC also simulates the detector responses of the various detector components and has an output which is similar to the output of the HERMES DeCoder (HDC). This makes it possible to apply the same chain of algorithms to the MC data as is applied to the measured data and enables a direct comparison between results found in the data with the MC simulations.

Chapter 4

Lambda Wheels

In 1997 it was proposed to develop and build the Lambda Wheels together with a Recoil Detector (RD) [47]. Both detectors were designed as silicon-strip detectors and had to be placed inside the beam vacuum close to the beam line. The LW was designed as a wheel-shaped detector placed between the target and the first tracking detector and the RD was proposed to be a flat array of silicon counters placed parallel to the target. The physics case for the LW was mainly based on a predicted increase in Λ^0 yield (by a factor of 2), a reduction of the false asymmetries encountered in the measurement of the Λ^0 polarization from 0.35 to 0.02, and access to the kinematic region of negative x_F which is unaccessible with the standard HERMES spectrometer. Furthermore the LW were expected to increase the detection probability of Λ_c baryons with a factor 2 as well. With the addition of the RD the exclusivity of reactions needed to study GPD's can be ensured and the study of J/Ψ production was predicted to be improved. In general the proposed detectors were expected to contribute to the study of the role of strangeness (through Λ^0 production) and gluons (through charm production) in the nucleon spin structure. It is noted that the importance of Λ^0 production has increased (see chapter 7) while that of charm production has decreased once it was found that the production cross section is small at the relevant energies [48].

To test the feasibility of operating a silicon detector under the harsh conditions mentioned above a Silicon Test Counter (STC) was installed and commissioned in the fall of 1998 [49]. The STC proved that the operation of silicon counters inside the beam vacuum close to the lepton beam itself is possible [50]. With the data collected by the STC it was shown to be possible to measure the momentum distribution of recoiling protons from DIS events on a deuterium target [51]. The first prototype LW module was installed and operated at HERMES in the beginning of 2000 [48, 52]. The first steps to incorporate the LW data into the HERMES data stream were taken together with the development of a dedicated tracking code. This enabled the determination of the angular resolution of this prototype LW detector which was found to be 2.1 mrad while the single-plane efficiency was determined to be 97%.

All 12 modules of the LW were installed for the first time at HERMES in 2002 after the delayed HERA upgrade which resulted in the commissioning of the complete LW detector system in 2002-2003. During the commissioning phase data were collected with the LW that were used to fully align the LW with respect to the HERMES spectrometer [9, 53]. The commissioning also provided the first successful data taken with the LW together with the HERMES spectrometer in the second half of 2003. The analysis presented in this thesis uses the data which were taken from January till the summer shutdown in August in the year 2004.

The first design of the RD was changed into four parallel arrays of silicon detectors surrounding the target and was expanded with a Scintillating Fiber detector, a photon detector and a superconducting longitudinal magnet [54]. The RD was installed at the end of 2005 and was commissioned in 2006.

This chapter describes the design of the LW (section 4.1) followed by a discussion of the data taking with the LW during 2004 in section 4.2. The tracking algorithms for long, short and LW tracks are discussed in section 4.3. In section 4.4 the evaluation of the efficiency of the LW is presented.

4.1 Design

Because the LW had to be placed between the downstream end of the target and the first tracking detector it was chosen to mount it inside the so called pumping cross[1]. A schematic drawing of the chosen configuration can be seen in figure 4.1, further illustrated by a picture in figure 4.2. The pumping cross is a barrel-shaped vessel attached to the target chamber equipped with two pumps which prevent the gas from the target cell to deteriorate the beam vacuum ($< 10^{-7}$ mbar). This configuration implies that the design has to fulfill several strict requirements. The selected materials should have a low out-gassing rate and should not influence the pump capacity in the pumping cross. The RF field induced by the beam should be shielded from the electronics to ensure a proper readout of the detector. The support structure and detector itself should contain a minimum amount of material

---

[1] A compromise between detection yield and cost had to be made. The larger the detector the more acceptance is covered but the higher the cost. The smaller the distance to the target the bigger the acceptance but the lower the yield of longer living particles through the longer decay length.

in the HERMES acceptance to minimize the multiple scattering of particles in the front region. The installation and maintenance should be possible through two C250 flanges in the pumping cross. Moreover, an external cooling should be added to the system to take away the heat produced by the electronics. The track resolution should be comparable to that of the HERMES front tracking. These requirements led to the choice of a silicon strip detector.

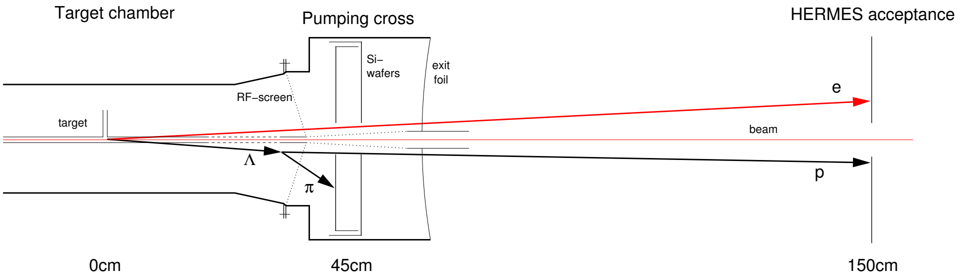

Figure 4.1: The location of the LW with a schematic drawing of a Λ^0 decay.

The LW is a wheel-shaped detector which consists of 12 trapezoidal modules mounted on a rotatable frame inside the pumping cross. The installation of the LW is carried out through the C250 flanges where each module is inserted and fixed to the frame after which the frame is rotated such that the next module can be installed. The pumping cross is closed on the side of the spectrometer with a 300 μm thin stainless steel foil. The RF fields from the beam are minimized by an RF screen mounted at the side of the target and by covering the wake field suppressor[2] and pumping holes of the target extension with a fine mesh.

Each LW module contains two double sided silicon wafers which are 5 cm apart, as illustrated by the CAD drawing in figure 4.2. The wafers are trapezoidal with an apex of 30^o, a base of 85.3 mm and a tip of 23.2 mm. The silicon wafers have a thickness of 300 μm, the strips have a width of 60 μm and a pitch of 160 μm. Each side has 516 strips of which 17 strips are too short and left unconnected. This makes the LW a detector with a total of 23952 channels to be read out.

The readout of the strips on the wafers is done by 128-channel HELIX v2.2 chips which are connected to the strips with 25 μm aluminium wire bonds. Four such chips read out one side of a wafer which makes for 16 chips per module and 192 chips for the entire LW. These HELIX chips are placed on a multi-layer kapton-copper hybrid because normal printed circuit boards would not fulfill the ultra-high vacuum requirements. The HELIX chips are

---

[2] The wake field suppressor is an open cylindrical tube connecting the target cell with the beam pipe behind the exit foil. The suppressor has a set of holes to ensure that the vacuum inside and outside are the same.

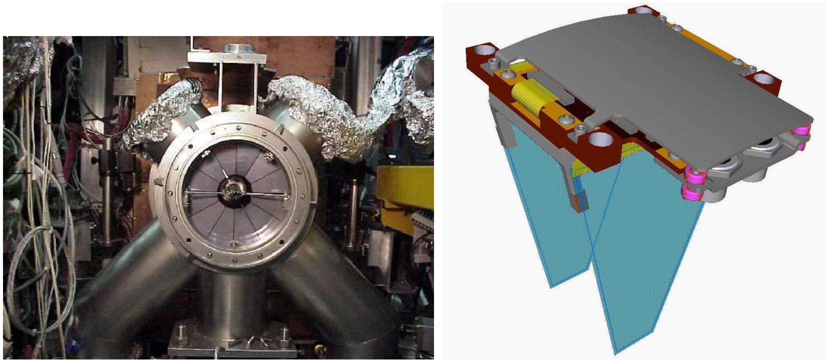

Figure 4.2: Picture of the complete LW installed inside the pumping cross on the left with a CAD drawing of a single module shown on the right.

powered with a ±2 V LV power supply system which is controlled through a CAN (Controller Area Network [55]) interface. There is also a bias voltage applied to the wafers to deplete the silicon with a CAEN power supply [56] which provides typically 50 V to each wafer .

Because each HELIX draws a current of 0.09 A during normal operation an external cooling is needed to take away the 70 W of heat produced for the entire LW. This cooling consists of a closed alcohol circuit which is cooled by peltier elements which transfer their heat to an open water circuit which is kept at a constant temperature of 12^oC. The closed alcohol circuit cools the modules through heat conducting copper blocks with which the LW modules are mounted on a wheel shaped frame inside the pumping cross. This cooling system can keep the LW modules, when switched on, at a stable temperature of -10^oC. A disadvantage of the v2.2 HELIX chip is that the time to initialize the chips is about 10 minutes or more at temperatures below 0^oC. As a remedy a flashlight has been built that is mounted on a flange of the pumping cross which shines light in the pumping cross during the initialization of the HELIX chips. The emitted photons take the chips out of their metastable equilibrium which otherwise prevents their initialization. With this remedy the LW could be switched on in a matter of minutes. This is important because the HELIX chips have to be switched off before a beam dump and during injection because radiation could produce a temporary short in the chip which would destroy it.

The initialization itself of the HELIX chips is controlled by a custom made HeLix Control Unit (HLCU) which sets the internal registers of all 192 HELIX chips of the LW. This unit also provides the clock and trigger for the chips. For the readout of the HELIX chip a custom made Hermes Analog to Digital Converter (HADC) is used. Each LW module is read out by one HADC module which consists of 4 ADCs with 512 channels each. These

HADC modules are capable of subtracting the common mode noise for each chip and a preloaded pedestal value. When the signal from a strip is still above a set threshold after these subtractions it is accepted as a fired strip and written to the data stream. In this way the total number of channels written to the data stream is reduced to a few channels per wafer side for each trigger.

4.2 Operation

The first step in going from the output of a detector to a physics analysis is the readout of the detector. In the LW this is organized by using HELIX chips which send their signals to the HADCs. This readout starts upon an external trigger after which the HELIX chips send the information from the silicon strips in a sequential order to the HADC which then puts the measurement for each strip in one ADC channel. In order to synchronize this sequence of data the HELIX chip starts the sequence with a signal called data valid. This signal is measured in the HADC with a comparator. The data collected in the HADCs is then passed on to the DAQ system which reads out each HADC sequentially. In the DAQ the information from the HADCs is merged with the readout information from all other HERMES detectors and stored in an event.

There is however a small chance (1 in 221500 for each HADC) that the comparator in the HADC does not recognize the data valid signal of the HELIX data stream after which the data is not entered in the HADC. When the DAQ wants to collect the data from this HADC it will fail which causes the following HADCs not to be read out. The information from the HELIX chips is, however, stored in the following HADCs and will be read out by the DAQ on the next trigger. Therefore the current event will contain information from less than 12 HADCs and the next event will contain information from different events which causes the data to be unsynchronized. The working solution used during the 2004 data taking was to operate the HADCs for a fixed time of a few seconds after which a reset was initiated which cleared all data from the HADCs and synchronized the readout[3].

In the decoder the events from the LW were checked on their synchronization. Events which had less than 12 modules in the data were rejected together with events which were not synchronized[4]. This results in a data

---

[3] This problem was anticipated in the design of the detector but it was assumed that it could be solved in the general HERMES readout system which appeared not feasible.

[4] The synchronization of an event can be checked by scalers which are counted in the HADC. These scalers contain, among other, the number of triggers, accepted triggers and rejected triggers. These scalers should count the same for all HADC modules and indicate a loss of synchronization if not.

taking efficiency of less than 100%. The percentage of remaining synchronized events to the total events taken are given in figure 4.3 for each run in the 2004 data taking.

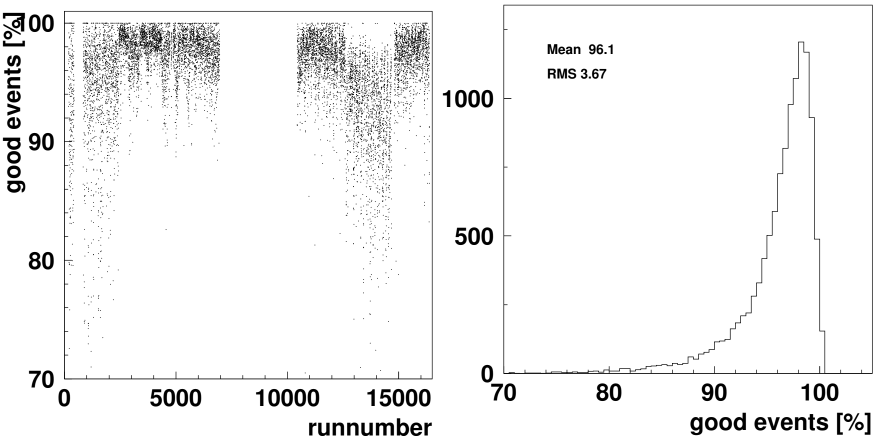

Figure 4.3: The percentage of events taken with the LW which pass the synchronization requirements in the decoder for each run taken in 2004.

The larger spread for the first 2000 runs in the left panel of figure 4.3 is due to the time between resets which was 10 s at that period. This time was based on the dead time of 2 s which was needed to reset the HADCs. After the initial 2000 runs the software was optimized and the dead time reduced to a few ms which enabled a much shorter operation cycle of 2 s after which the HADCs were reseted [57]. This reduced operation cycle decreases the number of events which are not synchronized since the probability of an unsynchronized event, causing all data to be unsynchronized until the HADC reset, is constant. The small gap at run 700 was due to a broken HLCU. The larger gap between run 7000 and 10000 was due to a short in the power supply of the VME crate which caused a downtime of one month in the LW operation. The drop from run 13000 till 15000 was caused by a malfunctioning LW module. Nevertheless a total average of $96.1 \pm 3.7\%$ of good events were collected during the operation of the LW in 2004 and a dead time of less than 2.5% was achieved. These events are further processed in the production chain and are used in the dedicated tracking code discussed in the next section.

4.3 Spectrometer and LW tracking

As mentioned before there are three types of tracks recorded in the HERMES experiment namely: long tracks (observed throughout the whole spectrometer), short tracks (observed in the front and magnet chambers but not in all back chambers) and LW tracks (reconstructed from hits in the LW). The first two track types are reconstructed with the main HERMES Reconstruction Code (HRC), which is the subject of the first subsection. The latter track type is reconstructed with the eXtended Tracking Code (XTC), which is the subject of the second subsection. In what follows a description of the working principles of each reconstruction method is given together with the relevant resolutions of the two tracking algorithms.

4.3.1 Long and short tracking

The spectrometer tracking algorithm for long tracks is designed to first find straight tracks in the front part and the part behind the spectrometer magnet [58]. In a second step the tracks in the front and back part of the spectrometer are combined in the center of the spectrometer magnet in a method called forced bridging. In a third step the charge and momentum of the tracks is determined.

Treesearch

The track finding algorithm used in the tracking code is based on a pattern recognition method called treesearch. This method is based on the use of a pattern database containing all possible configurations of tracks in a given detector with given resolution. In HERMES this method is used for the first time on such a big scale. This requires a special way of compressing the database. The compression is based on the symmetry of the patterns which can be exploited by only storing the symmetry relations between patterns instead of the patterns themselves. In this way the size of the database can be reduced from 126 million down to 31,000 entries. This method is described extensively in [58].

Forced Bridging

The front chambers suffer from a low resolution in the position determination. To compensate an additional requirement is introduced by enforcing that the front and back tracks of one event should meet in the same point in the middle of the spectrometer magnet. This method is called forced bridging.

Momentum Determination

The momentum of a long track is determined by comparing the response of the detectors to that calculated on the basis of 500'000 electron and positron tracks trough the spectrometer. These calculations are varied on a lattice in the z-position of the vertex, scattering angle in x, scattering angle in y, and the momentum. All this information is stored in lookup tables from which the momentum of the track is determined starting from the forced bridge assumption. This method results in the determination of the momentum with an accuracy of 0.1% [58].

Short tracking

The algorithm for the reconstruction of short tracks uses the requirement of a minimum of 4 hits in the planes of the Magnet Chambers (MC) detectors. The track finding is done with the use of a lookup table which contains entries for different charge, bending angle in the horizontal plane and momentum. With this lookup table a 1-dimensional histogram in momentum is filled for each plane of the MC after which the histograms are merged and a significant increase in one of the momentum bins is identified as evidence for a short track. For the track fitting also hits in the 12 planes of BC1 and BC2 are used when these hits are present. The track fitting is combined with the determination of the momentum in an iterative process by tracing the track in the magnetic field and minimizing the deviation from the hits in the tracking detectors [59].

Momentum and Angular Resolution

The performance of the long and short tracking algorithms as encoded in HRC was investigated with the HERMES Monte Carlo which included a full GEANT simulation of the detector. The results obtained from this study are shown in figure 4.4. Here the resolutions in momentum and horizontal scattering angle Θ_x are shown versus momentum for hadrons and leptons.

One can see that the momentum resolution for hadrons varies between 1.4 and 1.6% and the scattering angle is defined with an accuracy better than 1 mrad for momenta above 4 GeV.

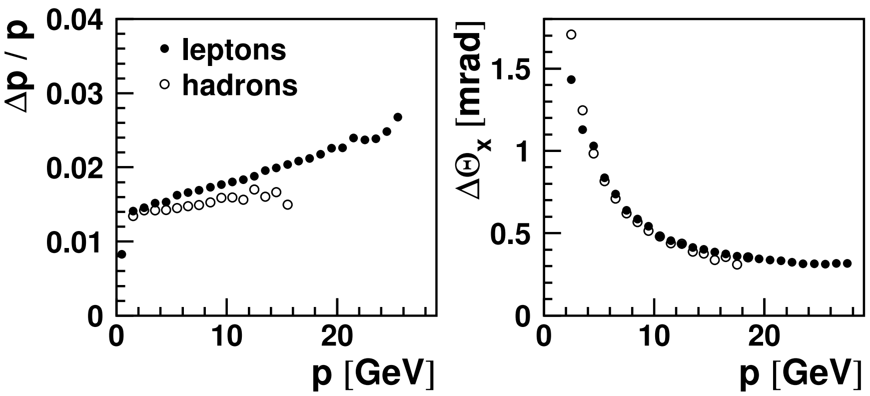

Figure 4.4: Momentum and angular resolutions versus momentum of leptons and hadrons as obtained from the HRC tracking code in combination with the HERMES Monte Carlo [3].

Multiple Scattering

The efficiency and accuracy of the tracking detectors and reconstruction algorithm determine the resolutions to a certain extend, but a large contribution to the observed resolution is due to multiple scattering as well. The formula for multiple scattering is [60]:

$$\theta_0 = \frac{13.6\ \text{MeV}}{\beta c p} z \sqrt{x/X_0}\,[1 + 0.038 \ln(x/X_0)]\,, \tag{4.1}$$

where p, βc and z are the momentum, velocity and charge number of the incident particle and x/X_0 is the thickness of the scattering medium in radiation lengths.

From this formula the multiple scattering due to the 0.3 mm stainless steel exit foil ($X_0 = 18$ mm) and the two 0.3 mm thick silicon wafers ($X_0 = 94$ mm) of the LW can be calculated. In figure 4.5 the multiple scattering for protons and pions is shown for momenta which are typical for the HERMES experiment.

From this figure it is clear that the addition of the LW to the HERMES spectrometer introduces only a minor additional contribution to the multiple scattering which is mostly dominated by the exit foil. Furthermore, the multiple scattering for protons and pions is comparable in size, and for momenta below 4 GeV multiple scattering is the dominant contribution to the angular resolution of the tracking in HERMES. These results will be used in the next chapter where the effect of the angular and momentum resolutions of the tracks on the resolution of the Λ^0 mass is studied.

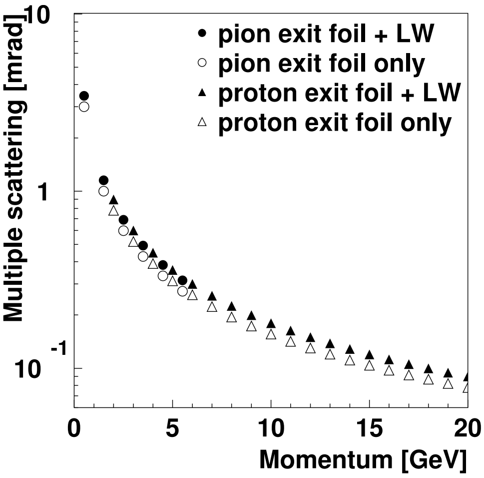

Figure 4.5: Multiple scattering due to the exit foil only (open symbols) and also including the effect of the two silicon wafers of the LW (closed symbols), for protons (squares) and pions (circles) versus their momentum.

4.3.2 LW tracking

The LW tracking is performed in what is called the eXtended Tracking Code (XTC). This code is based on an algorithm that was extensively described and discussed in [48] and [9]. In this section the working principles of the code and some results are given.

The LW tracking code consists of five steps to convert the decoded detector information to tracks which can be used in a physics analysis. These steps can be summarized as the formation of clusters for each wafer side, the determination of the hit position in each wafer, the construction of tracks in each module, the alignment of the LW in the HERMES spectrometer, and the comparison of LW tracks with those observed in the spectrometer.

The first step is the clustering where neighboring strips that fired are combined into clusters. The signal associated with the clusters is the sum of the signal in all strips in the cluster. The cluster position is a weighted average of the contributing strips. The clustering enables a more accurate position determination. Single strips which have no neighboring strips that fired are also called a cluster. Also two fired strips which have a dead strip or disconnected strip in between are combined into a single cluster. These clusters are made independently for each side of the wafer.

The second step is to evaluate hit coordinates from clusters on the front and back side of a single wafer. This is done with a Figure of Merit algorithm described in [48]. It favors correlated signals in clusters on the front and back side of a wafer and disfavors combinations which are due to noise with a relatively small or large signal. Tracks are reconstructed from the hit coordinates found in each wafer of a single LW module.

All possible tracks between hit coordinates in the first and second wafer of a module are constructed. Because the two space points are located in two wafers that are 5 cm apart always a straight line is defined. Tracks which have an angle larger than 0.5 rad are rejected on the basis of a Monte Carlo study which showed that decay pions from Λ^0 decay cannot be produced beyond this angle [61].

To enable the comparison of the formed tracks with those found in the HERMES spectrometer the tracks have to be corrected for the misalignment of the LW w.r.t. the spectrometer. The alignment procedure is described in detail in [9]. It involves the positioning of the complete LW detector in the z direction where an offset of 1.2 ± 0.2 cm was found. Furthermore, minor offsets in the x and y positions were found of -0.22 ± 0.05 cm and 0.068 ± 0.002 cm, respectively. The rotational corrections were also determined of which the rotation around the beam line was found to be the biggest with a value of 7.0 ± 2.6 mrad. The LW modules were each measured in an optical alignment machine before installation with a precision of 5 μm which enabled corrections for the positions of the wafers in the modules. All these corrections have been applied to the data.

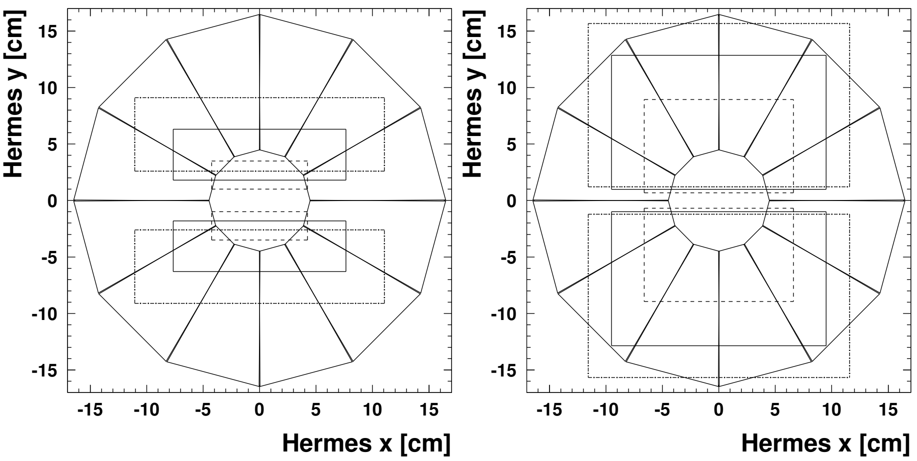

Figure 4.6: The LW acceptance at $z = 47.5$ cm. On the left: the HERMES spectrometer acceptance is drawn for particles originating the beginning of the target $z = -20$ cm (dashed), middle $z = 0$ cm (solid) and end $z = 20$ cm (dotted). On the right the DVC acceptance is drawn for the same values of z as were used on the left side.

When the tracks are properly corrected for the results obtained in the alignment procedure they can be compared with the HERMES spectrometer data. Three criteria are used to calculate a quality factor for each reconstructed

HRC	-1	not in HERMES acceptance
	0	in the acceptance but no matching HRC track
	HRC nr	nr of the matched HRC track
DVC	-1	not in the DVC acceptance
	0	in the DVC acceptance but no hit in at least 3 different wire-orientations (X, U, V)
	1,2	cannot occur
	3,4,5,6	nr of planes containing a hit
target	0	not in the target
	1	in the target

Table 4.1: The criteria to assign a quality factor to a LW track.

LW track. First, it is verified if the tracks originate from the target by selecting the distance to the beam smaller than 0.75 cm and the z vertex position within the target cell to be within ±20 cm. The second criterion is a comparison involving the DVC. As can be seen on the right in figure 4.6 the acceptance of the DVC has a significant overlap with the LW acceptance. Each track in the LW is projected on to the DVC to check if it is in the DVC acceptance and to look for signals in the DVC in the vicinity of the reconstructed LW track. In the third and last criterion the LW track is compared to tracks originating the HERMES spectrometer acceptance, shown on the left in figure 4.6, as reconstructed by the HRC tracking code. On the basis of these three criteria a quality factor is assigned to each track reconstructed in the LW. In table 4.1 the criteria are listed which are used to calculate the quality factors shown in table 4.2.

As can be seen in table 4.2 an extra factor is assigned to the criteria for both HRC and DVC tracks. A negative factor is added when the LW track is inside the DVC and/or HERMES acceptance but is not observed in that detector, while a positive factor indicates that the track is inside the acceptance and detected in the DVC and/or HERMES acceptance. The quality factor is 0 or 0.42 if the track is not in any acceptance or only originating from the target, respectively[5]. The negative values listed in 4.2 indicate that the track is inside the acceptance but not detected there, while values of 1 or higher indicate that the track is also detected in the DVC and/or has a matching HRC track.

---

[5] The value 0.42 is historical and was chosen to reflect the importance of the selection criterion which is the least restrictive in case the track originates from the target.

HRC			DVC			target		qf	
-1	0	nr	-1	0	3,4,5,6	0	1	HRC DVC	Sum
x			x			0			0.00
x			x				0.42		0.42
x				x		0		-0.5	-0.50
x				x			0.42	-0.5	-0.08
x					0.3 0.4 0.5 0.6	0		1.5	1.80-2.10
x					0.3 0.4 0.5 0.6		0.42	1.5	2.22-2.52
	x		x			0		-0.5	-0.50
	x		x				0.42	-0.5	-0.08
	x			x		0		-1.0	-1.00
	x			x			0.42	-1.0	-0.58
	x				0.3 0.4 0.5 0.6	0		1.0	1.30-1.60
	x				0.3 0.4 0.5 0.6		0.42	1.0	1.72-2.02
		x	x			0		1.5	1.50
		x	x				0.42	1.5	1.92
		x		x		0		1.0	1.00
		x		x			0.42	1.0	1.42
		x			0.3 0.4 0.5 0.6	0		2.0	2.30-2.60
		x			0.3 0.4 0.5 0.6		0.42	2.0	2.72-3.02

Table 4.2: The calculation of the quality factor used in the LW tracking code.

LW Resolutions

To calculate the resolution of tracks observed in the LW these tracks are compared to spectrometer tracks. In a first study the angular resolution of the LW is determined by comparing the slope of a LW track with the slope determined by HRC. The width of these distributions is plotted on the right in figure 4.7. Here the angular resolution is given for each module in the x and y direction of the slopes. The values differ for each module orientation, as the relative orientation of the strips of each module varies from module to module, as is indicated on the left in figure 4.7. On average the angular resolution of the LW tracks is 3 mrad. This is larger than the angular resolution in HRC because of the small lever arm of 5 cm within the LW as compared to 12 cm between the two FC chambers and 175 cm between BC1/2 and BC3/4.

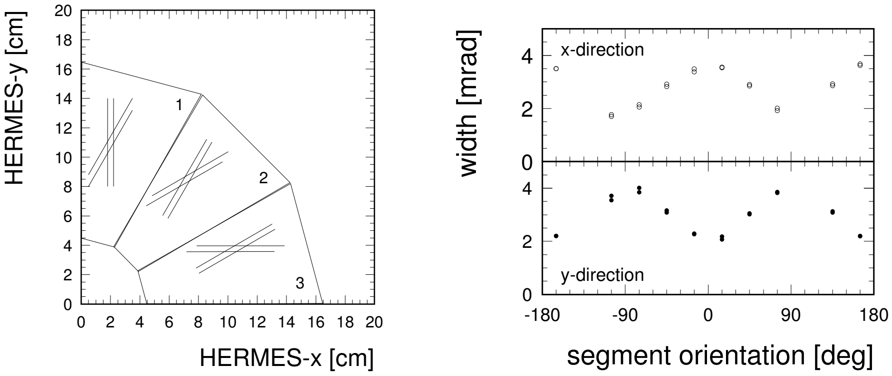

Figure 4.7: On the right side the angular resolution in the x and y direction is plotted for each LW module. The variation is due to the orientation of the strips indicated on the left side.

The vertex resolution of the LW is compared with that of the HRC tracks in figure 4.8. Here the resolutions in x and y are given versus the z position of the vertex. One can see that the vertex resolution of the LW is better than that of the spectrometer and agrees well with the simulated values. Due to the circular acceptance of the LW the values for x and y are the same while the spectrometer is more accurate in the x direction than in y. This is due to the orientation of the wires in the FC tracking chambers which is vertical or tilted at ±30 degrees. This configuration determines the x direction better than the one in y. Also the dependence on the z position is more clear in the LW because of the worse angular resolution.

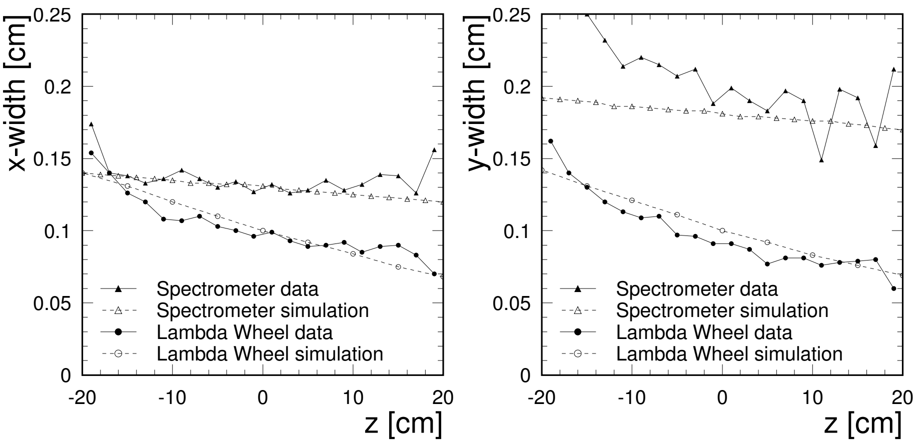

Figure 4.8: The vertex resolution in x (left) and y (right). The LW (circle) and spectrometer (triangle) vertex resolutions are plotted versus the z position of the vertex and compared with a simulation (open symbols).

From these studies it is concluded that the position of the decay vertex of a Λ^0 hyperon can be reconstructed with an expected resolution below 1.5 mm when both decay particles are tracked in the LW. This result will be shown to result in a major improvement in the reconstruction of Λ^0 hyperons using the LW in section 5.1.6.

4.4 Efficiency

The efficiency of the prototype LW module has been determined in [48] and that of the complete LW in [9]. In this section the efficiency for the complete LW is determined for the running period 2004.

The efficiency is determined by comparing HRC tracks that pass the active volume of the LW with LW tracks in that same volume. The HRC tracks are projected on the LW and a circle with a certain radius, called road width, is formed around these projection points. In this circle a LW track is searched for with similar slopes. To avoid edge effects the area at the edges of the modules with a width equal to the road width is not considered. The efficiency for a single LW module is defined as the number of HRC tracks which have a matching LW track divided by the total number of HRC tracks that pass the active volume under study. This number is calculated for each module using a road width of 1.5 cm. The results for all 12 LW modules versus run number is presented in figure 4.9.

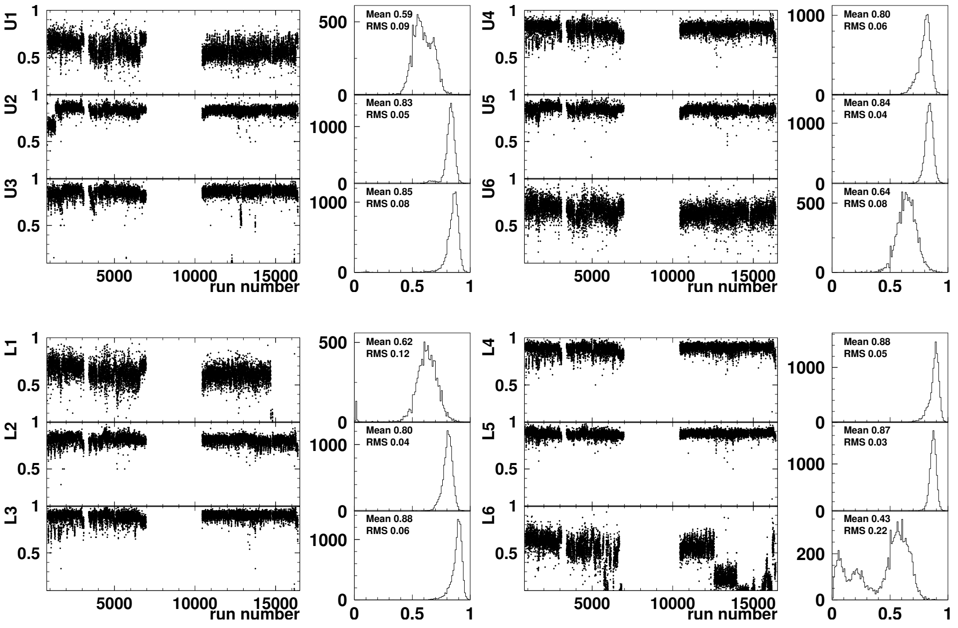

Figure 4.9: Efficiencies of all 12 LW modules versus run number for the data taking period 2004, where efficiency is the percentage of HRC tracks in the active volume of the LW which have a corresponding LW track.

The dropping efficiency at the end of the running period in module L6 was due to a problem in the corresponding HADC and a problem with the HV. The missing data for module L1 from run 15000 is due to a broken wire bond on the module.

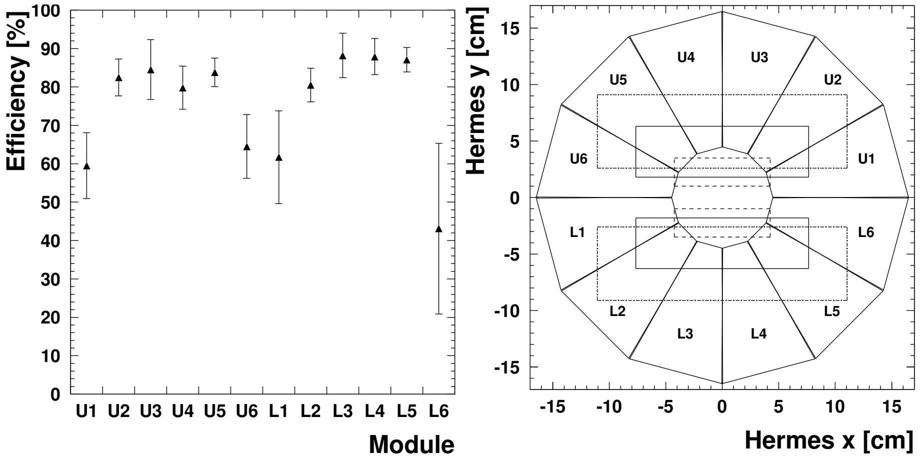

Figure 4.10: Average efficiencies for all 12 LW modules. The lower efficiencies for modules U1, U6, L1 and L6 is due to the overlapping HRC acceptance shown on the right.

The efficiencies are averaged over the year using the width of the efficiency distribution as the error for the mean. In this way figure 4.10 has been obtained. A somewhat lower efficiency is observed for modules U1, U6, L1 and L6 while the efficiencies of the other modules have approximately the same values. This behavior can be related to the overlap of the HRC and LW acceptance shown on the right in figure 4.10. The modules in the horizontal plane have only a very small overlap with the HERMES acceptance which is also located at the edges of the wafers. Therefore, the projection of the HRC track has a higher probability to end up in the neighboring module which has a negative effect on the efficiency. The average efficiency calculated without the 4 low efficiency modules in the horizontal plane is found to be $84.5 \pm 1.6\%$. Because this efficiency is determined by requiring at least one LW track per event the loss due to synchronization problems (see section 4.2) is not included in this number. When the percentage of good events of $96.1 \pm 3.7\%$ (see end of section 4.2) and the average dead time of 2.5% is taken into account the total tracking efficiency is evaluated to be $79.2 \pm 3.4\%$.

With all the hardware and tracking software introduced it is now possible to perform a physics analysis on the long, short and LW tracks. In the next section the analysis tools developed to reconstruct the Λ^0 hyperon are described.

Chapter 5

Λ^0 Hyperon reconstruction

This chapter describes the observation of Λ^0 hyperons through their decay $\Lambda^0 \rightarrow p\pi^-$ which has a branching ratio of 63.9% [1]. The detection of the Λ^0 hyperon enables the measurement of it's polarization, which is the subject of the next chapter. The polarization gives information on the relative orientation of the spin of the s-quarks with respect to that of the valence u-quarks as introduced in chapter 2. Such data will give us more insight into the spin-structure of the nucleon especially regarding the role of the sea quarks. It is also of interest to measure the Λ^0 polarization with unpolarized incident leptons and a transversely polarized target as such measurements provide an alternative approach to transversity determinations. Although the latter subject is not fully explored in this thesis, it explains why in this chapter also data collected with a transversely polarized target are presented.

The Lambda Wheels (LW) were added to the HERMES spectrometer to facilitate such measurements. In particular, the LW make it possible to explore the kinematic domain of negative x_F which was unaccessible before and which is particularly sensitive to the relative orientation of s-quarks. Furthermore, the LW are capable of measuring the polarization of Λ^0 particles in a more accurate way because of their azimuthal symmetry.

The region where x_F is negative, also referred to as the target fragmentation region, can be explored with the LW because in this region the Λ^0 particles have on average a lower momentum than those in the region where x_F is positive. When the lower momentum Λ^0 hyperons decay in a proton and a pion the angle between the tracks of these two decay products is larger than that of higher momentum Λ^0 hyperons. With the LW, the angular acceptance of the HERMES experiment is increased which leads to an increased acceptance of lower momentum Λ^0 particles.

---

[1] The $\Lambda^0 \rightarrow n\pi^0$ decay has a branching ratio of 35.8% but cannot be reconstructed in the HERMES spectrometer because it does not allow for the detection of neutrons.

This chapter describes how the kinematics of a Λ^0 hyperon is reconstructed with the use of tracks detected in the LW and the tracks detected in the HERMES spectrometer. On the basis of such reconstructed Λ^0 hyperon events the polarization of Λ^0 hyperons can be evaluated as is described in chapter 6.

Because this is the first time the LW are used for Λ^0 reconstruction the newly developed methods are described more extensively. This is the subject of the first part of this chapter. The reconstruction method is based on data taken when the transverse target magnet was switched off. In the second part of this chapter the reconstruction of the Λ^0 hyperon is discussed using data obtained with the transverse target magnet switched on.

5.1 Data analysis without target magnetic field

In the reconstruction of a Λ^0 hyperon decaying into a pion and a proton with the target magnet switched off, the tracks of all particles can be treated as straight lines. In the presence of a non-zero target magnetic field, however, the tracks of the pion and the proton are deflected which makes the reconstruction more complicated. The reconstruction in the presence of a magnetic field is described in section 5.2, while the present section describes the data analysis in the absence of a target magnetic field.

5.1.1 The Lambda Wheels method

Because the Λ^0 hyperon is neutral and has a short lifetime[2] it is not possible to detect it directly. The identification of an event containing a Λ^0 decay is carried out by calculating the invariant mass of its decay products, which are always a proton and a pion in this analysis. On the basis of the invariant mass spectrum the events containing a Λ^0 decay can be largely separated from the background events, as the Λ^0 events appear in a narrow peak centered around the previously measured value of 1.115 GeV [60].

In the calculation of the invariant mass the momentum and direction of each of the two decay particles are needed as can be seen from the equation below.

$$M_\Lambda^2 = m_\pi^2 + m_p^2 + 2\sqrt{(m_\pi^2 + |p_\pi|^2)(m_p^2 + |p_p|^2)} - 2|p_\pi||p_p|\cos\beta. \qquad (5.1)$$

---

[2] The lifetime of the Λ^0 hyperon (10^{-8} s) is short w.r.t. that of a proton, but long w.r.t. that of most elementary particles with lifetimes of about 10^{-23} s.

Here m_π and m_p are the pion and proton mass, $|p_\pi|$ and $|p_p|$ are the sizes of the pion and proton momenta and β is the angle between the pion and the proton tracks.

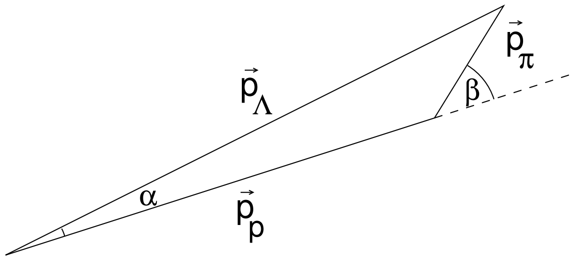

Figure 5.1: The momentum triangle of a $\Lambda^0 \rightarrow p + \pi^-$ decay event. The Λ^0 momentum can be calculated from the values of $|p_\pi|$, $|p_p|$ and β in the case where spectrometer tracks are used, or $|p_p|$, β and α when the LW are used.

The standard method of reconstruction used in the HERMES spectrometer is based on the momenta of all detected particles as measured by their bend in the spectrometer magnetic field. However, for a large fraction of the data collected with the LW the momentum of the decay pion cannot be determined directly as the pion (in contrast to the proton) does not pass the spectrometer magnet. Therefore a new method has to be developed which we call the LW method. By looking at the momentum triangle in fig 5.1 it is clear that the size of the pion momentum $|p_\pi|$ can be calculated if the size of the proton momentum $|p_p|$ and the two angles β and α are known:

$$|p_\pi| = \frac{|p_p| \sin\alpha}{\sin(\beta - \alpha)}. \tag{5.2}$$

The three quantities $|p_p|$, β and α can be determined as follows. We know the size and direction of the proton momentum $|p_p|$ when it is detected in the spectrometer. The angle β can be calculated if the pion direction is measured in the LW. The angle α can be obtained, based on the Λ^0 topology shown in figure 5.2. Here it is seen how α is defined by the direction of the Λ^0, which is determined by the position of the primary and secondary vertices. The secondary vertex can be reconstructed by evaluating the intersection of the proton and pion tracks, for which it is sufficient to know their directions. The primary vertex can be reconstructed by evaluating the intersection of the scattered beam lepton with the line shaped target. If the lepton is not detected, the primary vertex is taken as the intersection point of the beam with the plane defined by the proton and pion tracks.

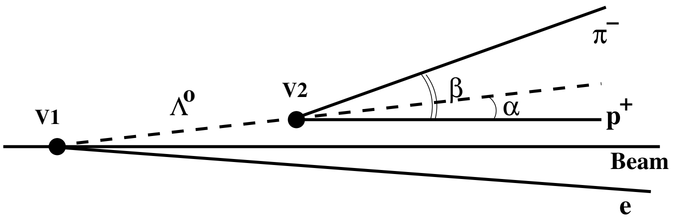

Figure 5.2: The topology of a $\Lambda^0 \to p^+ + \pi^-$ decay where V1 indicates the (primary) production vertex and V2 the (secondary) vertex of the decay.

The LW method, which calculates the Λ^0 invariant mass from $|p_p|$, β and α, is the basis of the analysis of the unpolarized data set when the extended acceptance of the LW is used.

5.1.2 Mass resolution estimate

Before applying the LW method to the unpolarized data set an estimate of the expected resolution of the Λ^0 invariant mass is presented. This is carried out for both methods used to determine the invariant mass as described in the previous section. From the formulas used in the two methods the dependence of the resulting mass resolution on the resolution of the input variables has been calculated.

In the case where proton and pion are detected in the spectrometer the invariant mass is evaluated from the size of the proton and pion momentum and the angle β between the 2 tracks. In this case formula 5.1 can be used to derive the resolution of the invariant mass as a function of the resolution by which the momenta and the angle β are measured. This dependence is shown in figure 5.3 where the mass resolution is shown versus the momentum resolution for various values of the angular resolution.

From the characteristics of the spectrometer tracking [section 4.3] a momentum resolution of 1.5 % for each particle and an angular resolution of 2.1 mrad for the pion and 1.3 mrad for the proton can be expected for Λ^0 production experiments at HERMES. These resolutions lead to an estimated mass resolution of 2 MeV if both the proton and pion are measured in the spectrometer. This is indicated by the dashed lines in figure 5.3.

If the pion is detected by the LW and not observed in the spectrometer, formula 5.1 can no longer be used directly since the pion momentum is derived from a sine rule (equation 5.2). This makes the calculation of the invariant mass dependent on the proton momentum $|p_p|$, the angle β and the angle α. The resolution of the invariant mass of the proton, pion system is derived from the substitution of equation 5.2 in 5.1 and shown in figure

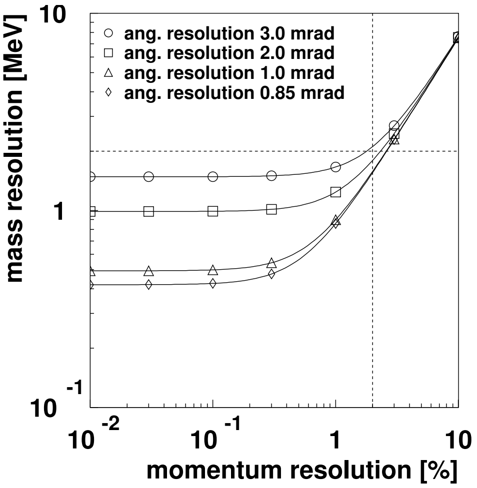

Figure 5.3: The effect on the Λ^0 mass resolution, if the pion and proton are detected in the spectrometer, of the momentum resolution of the decay particles for various angular resolutions of β. The dashed lines indicate the expected resolutions.

5.4. On the left the mass resolution is shown versus the proton momentum resolution for various values of the resolution on α, and on the right the mass resolution is plotted against the angular resolution of α for various values of the resolution in β.

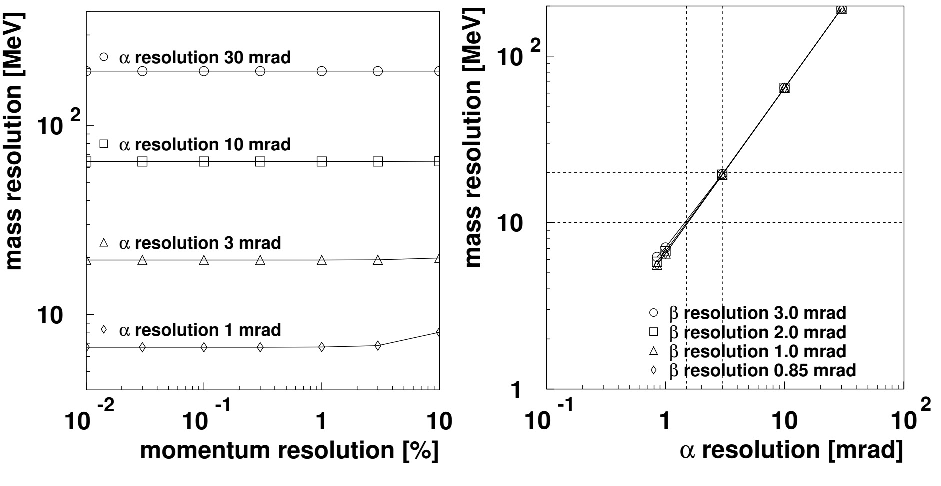

Figure 5.4: The Λ^0 mass resolution if the pion is detected in the LW and the proton in the spectrometer. On the left the effect of the proton momentum resolution is shown for various values of the α resolution. On the right the effect of the α resolution is shown for various β resolutions where the dashed lines indicate the expected resolutions.

From these plots it is seen that the effect of the proton momentum resolution and the β angular resolution do not have a big impact on the Λ^0 mass resolution. It is the accuracy in the determination of α which has the largest contribution.

Because the resolution in α is determined by the resolutions of the production and decay vertices and the vertex separation, this dependency has been studied separately. The result is shown in figure 5.5, where the resolution in α is calculated from the vertex separation for various values of the transverse resolution (σ_t) of the decay vertex and the longitudinal resolution (σ_z) of the production vertex. The horizontal dashed line indicates an α resolution of 3 mrad. With a resolution between 1.5 and 3 mrad for α the Λ^0 mass resolution is estimated to be between 10 and 20 MeV as can be seen from figure 5.4. From figure 5.5 it is seen that such α resolution values can only be reached for sufficiently large vertex separations.

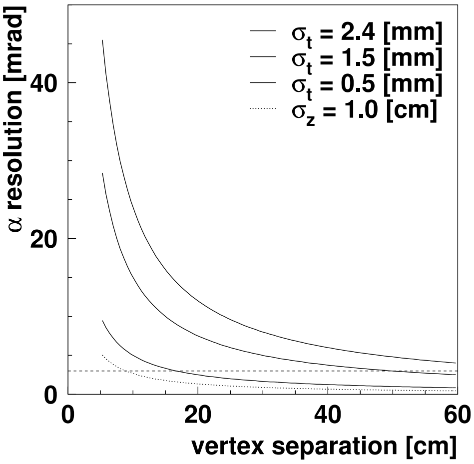

Figure 5.5: The resolution of α as a function of the vertex separation. The α resolution is shown for various values of σ_t, which indicates the transverse resolution of the decay vertex, and σ_z the resolution in z of the primary vertex. The horizontal dashed line indicates a resolution of 3 mrad in α.

Even though the vertex resolution obtained with the LW is better than that obtained with the spectrometer the expected resolution of the Λ^0 mass is 5 to 10 times worse compared to the 2 MeV resolution obtained with the spectrometer. This is due to the method that has to be applied to evaluate the pion momentum when using tracks measured exclusively in the LW.

5.1.3 Validation of the LW method

The estimates of the Λ^0 mass resolutions obtained when using the spectrometer tracks are different from those obtained by the LW method. In this section a comparison between the two methods when applied to the data is presented. A data set containing pion and proton tracks detected in both the spectrometer and the LW is used to compare the number of Λ^0 particles and the mass resolutions obtained by the two methods.

The number of background events in the data set used is reduced by requiring an opposite charge for the two particle tracks, selecting events where the distance between the primary and secondary vertex is larger than 7 cm and a distance of closest approach (DCA) less than 1.5 cm. The invariant mass spectrum obtained with the measurements in the spectrometer can be seen on the left in figure 5.6. Here the vertical line at 1.115 GeV indicates the Particle Data Group (PDG) [60] value of the Λ^0 mass. As expected a mass resolution of 2 MeV is observed, providing a clear separation between the region with the Λ^0 events and the region of the background events. With a window of 3 sigma around the PDG value of the Λ^0 the events containing Λ^0 decays are selected which are represented by the open histogram. The background events are represented by the hatched histogram.

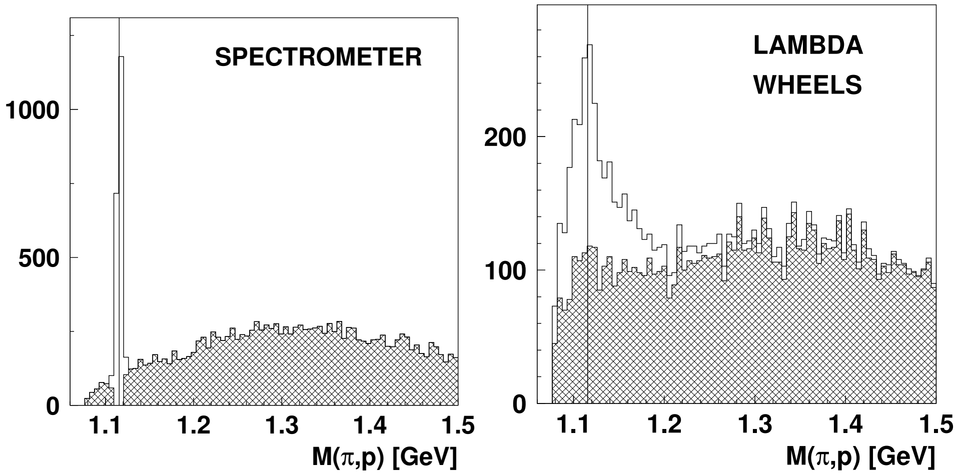

Figure 5.6: The invariant mass spectrum reconstructed from pion and proton tracks which are measured by either the spectrometer only or also involving the LW. Left: track parameters and momenta of the pion and proton as obtained from the spectrometer are used. Right: the proton momentum is obtained from the spectrometer while the track parameters measured by the LW are used. The hatched area represents the background events selected in the left spectrum.

Next, the LW method is applied to these same data using the track parameters as measured by the LW and the proton momenta measured by the spectrometer. This spectrum is shown on the right in figure 5.6. The hatched histogram shows where the background events selected in the left panel outside the Λ^0 mass peak end up in this invariant mass spectrum.

When we subtract the background events in the right hand spectrum of figure 5.6 we get the spectrum displayed in figure 5.7.

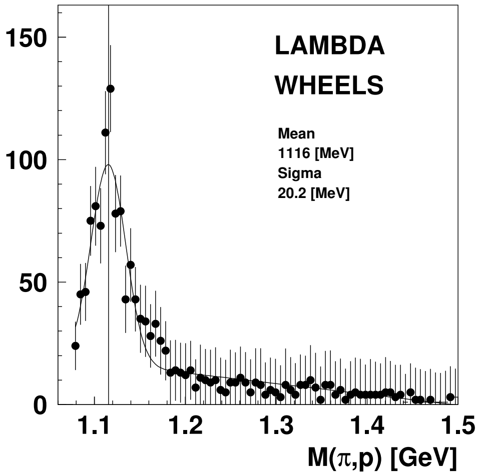

Figure 5.7: The spectrum resulting from the subtraction of the background events shown in the righthand panel of figure 5.6 fitted with a gaussian plus a first order polynomial.

In the spectrum based on the spectrometer measurements only, the number of Λ^0 particles counted in a window of 3 sigma, where sigma is 2.4 MeV, around the PDG value is 1762 ± 48 after subtraction of the background events under the peak estimated with a polynomial fit. When the number of Λ^0 particles are counted in figure 5.7 in a window of 3 sigma, where sigma is 20.2 MeV, around the PDG value a yield of 1387 ± 71 is obtained. This demonstrates that $78.7\% \pm 4.5\%$ of the Λ^0 decays seen in the spectrometer data are also reconstructed by the LW method in a 3 sigma window. The resolution is 20.2 MeV as determined from a fit with a Gaussian plus a first order polynomial is in good agreement with the estimated value discussed in the previous section.

5.1.4 First results obtained with the LW data

With the LW method verified against spectrometer data the reconstruction of Λ^0 hyperons can now be applied to all LW data. The data set analyzed here is the collection of unpolarized target data taken in the year 2004.

In table 5.1 the applied cuts are listed which result in the spectra shown in figure 5.8 where a peak of events around the PDG value of the Λ^0 can be seen.

The set of applied cuts can be divided into three categories, namely PID selection, tracking cuts and restrictions on the Λ^0 topology. The PID selec-

proton PID	not a pion by RICH and positive charge quality factor for RICH identification > 0
Tracking	primary vertex -18 cm$< z < +18$ cm decay vertex $z < 45$ cm quality factor for LW tracks > 1 DCA < 1.5 cm
Λ^0 topology	vertex separation > 8 cm Λ^0 direction in between pion and proton direction

Table 5.1: Requirements imposed on the LW data displayed in figure 5.8.

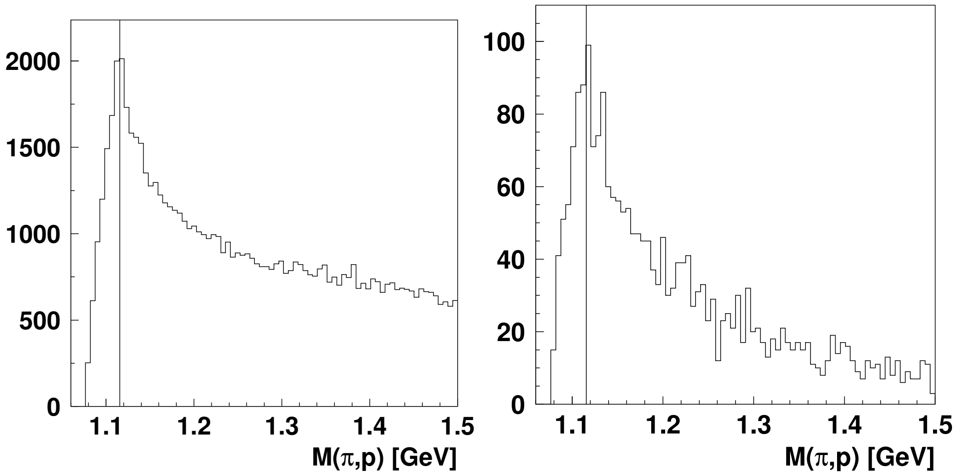

Figure 5.8: Invariant mass spectra with the cuts listed in table 5.1 applied, on the left without detected beam lepton, on the right with a detected lepton.

tion of the proton is done by the RICH which implies that the proton has to be a long track. The particle identification by means of the RICH only enables a positive identification of pions with momenta larger than 1 GeV (as illustrated in figure 3.3), while protons are only positively identified for momenta greater than 4 GeV. Therefore, it is more efficient to exclude positively identified pion tracks rather than using a positive identification of a proton track. With the requirement on the quality factor all unidentified tracks are neglected. The tracking cuts are based on the position and size of the target cell, the LW tracking code described in section 4.3.2 and the relevant resolutions. The cuts related to the Λ^0 topology require the momentum triangle (figure 5.1) to be correctly defined. The vertex separation is based on the resolutions encountered in the LW method (figure 5.5).

The spectra in figure 5.8 show a clear excess at the PDG value of the Λ^0. The events reconstructed in these spectra are the first measurements with the LW which are used for a physics analysis of Λ^0 hyperons that cannot be measured with the spectrometer only. However, because the resolution is a factor 10 worse than in the case of the spectrometer tracks the separation with the background events is more difficult. To model the background in the same phase space as the measured data the mixed event method is used which is described in the next section.

5.1.5 Mixed event background

It is expected that the background in the Λ^0 invariant mass spectrum is mainly due to track combinations which are uncorrelated and are therefore not originating from any resonance. If this is true then this background can be modeled with track combinations which are not contained within the same event. This simulation of the shape of the background is called the mixed event method.

The mixed event method uses the same data set as described in the previous section but the proton track is taken from a different event. By combining a pion and proton track from different events no real Λ^0 decays can be found. Because the mixed event method uses the same data as the unmixed analysis, the same detector acceptance and efficiencies apply to both analyzes. Furthermore, various kinematic dependencies of the mixed event background can be calculated and subtracted from the data obtained in the unmixed data analysis.

All steps used in the analysis with the mixed events are performed exactly in the same way as in the analysis of the unmixed data. The only difference lies in the origin of the proton track parameters at the very start of the analysis which are taken from the previous event. This procedure can be repeated by combining the pion of the current event with the proton from the next to previous event to obtain a bigger mixed event data set. In this analysis the track mixing has been repeated in the five last events. This larger data set is used to describe the background while having minimized statistical fluctuations.

This analysis is applied to the events with and without a scattered lepton. Also various track combinations are used with the proton as a long track and the pion track either being a LW track, a short track or a long track. In this way the various spectra in figure 5.9 are obtained. The mixed event background sample is represented by the hatched histogram. It is normalized to the data, which are represented by the open histograms, by minimizing the difference in each bin in the mass regions covered by the horizontal lines. This normalization region was chosen to be at masses well above the PDG value of the Λ^0 and was extended up to a mass value where the discrepancy

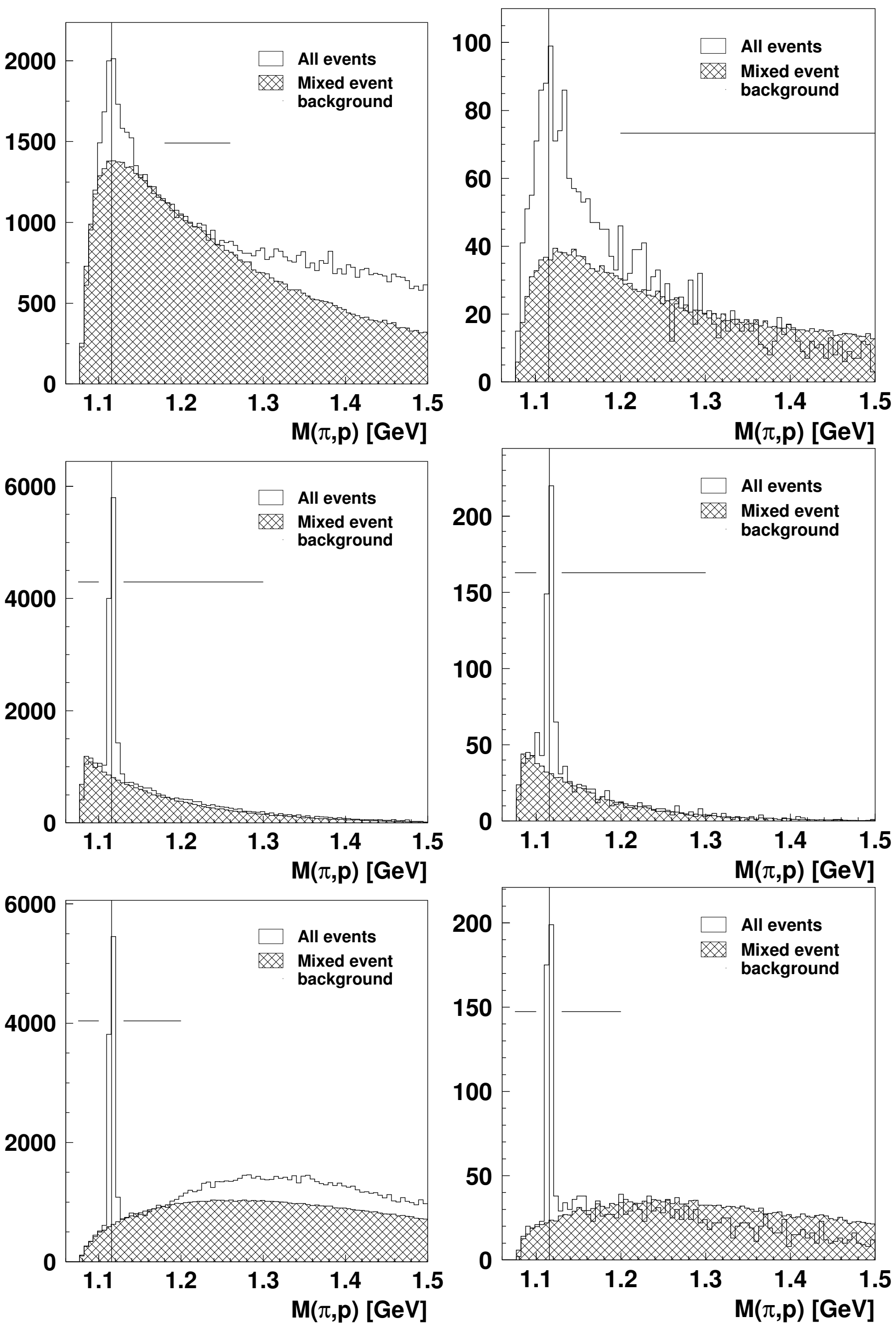

Figure 5.9: Invariant mass spectra for various data samples. In the left column events without a scattered beam lepton are shown while in the right column all events contain the scattered beam lepton. The pion track is from the top to bottom row respectively a LW track, a short track and a long track while the proton track is always a long track. The hatched histogram is a mixed event background normalized to the real data in the regions covered by the horizontal lines.

between data and background becomes relatively large. The plots in the left column show the events without detected beam lepton while the right column contains the events with detected beam lepton. The pion track is from the top to bottom row respectively a LW track, a short track and a long track, while the proton is always a long track. Note that all data sets use different tracks and all pion and proton tracks are only used once.

From figure 5.9 it is clear that the mixed event background does not always describe the shape of the data equally well. The background description in the right column, which contains the events where the beam lepton is also detected, matches the shape of the data at values above 1.20 GeV better than the data in the left column. Especially the discrepancy between the mixed event background and the data in the top left spectrum for LW tracks at higher invariant mass is worrying. In the next section an optimization of the analysis procedure is discussed which reduces this discrepancy.

5.1.6 Optimization

In order to improve the signal to noise ratio of the LW spectra discussed in the previous section a study is carried out of events where the proton is also detected in the LW. This sample of events is a subset of the events used in the top left hand spectrum of figure 5.9. About 35.2% of the events contain a proton track which is also detected in the LW. For these events the track parameters determined with the LW can be used for both pion and proton tracks. It is expected that the resolution of the decay vertex is improved in this way because now the tracks of both decay products are reconstructed in the LW.

An improved vertex resolution is directly correlated with the width of the DCA distribution which becomes smaller with a better vertex resolution. This is precisely what can be seen in figure 5.10. The DCA between the pion and proton track is presented by the dashed distribution where the proton track parameters are determined by the spectrometer, while the solid histogram represents the DCA where the proton track parameters are determined by the LW.

A major improvement is seen by comparing the two distributions. The events below 0.6 cm in the HRC spectrum are now located below 0.2 cm in the LW spectrum. Also, the level and shape of the background events above 1 cm in the two spectra remain the same, which enables a more accurate separation from the background events when the cut on the DCA is lowered down to 0.5 cm, for instance.

This improvement in the determination of the decay vertex is expected to yield a better resolution on the angle α which was shown to have the largest

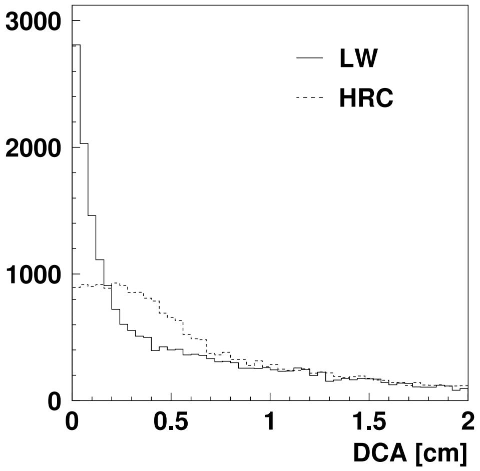

Figure 5.10: The DCA between a pion and proton track. The dashed distribution represents events of which the proton track parameters are determined by the spectrometer. The solid distribution represents the result when LW track parameters are used.

impact on the resolution of the invariant mass as determined with the LW method and illustrated in figure 5.4. The invariant mass distribution for the presently selected data sample where the proton and pion track parameters are taken from the LW is shown in figure 5.11 for events without detected beam lepton. Also shown is the mixed event data set represented by the hatched histogram.

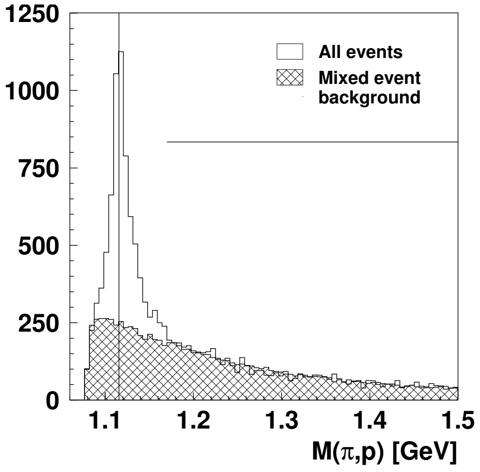

Figure 5.11: The invariant mass for (π,p) events without detected beam lepton where the proton and pion track parameters as determined by the LW are used. The hatched histogram represents the mixed event background.

In this figure the mixed event background distribution describes the region from 1.18 GeV up to 1.5 GeV very well and no discrepancy can be seen anymore. From a Gaussian fit of the Λ^0 peak a σ of 9 MeV is found and the ratio of signal to background is found to be improved by a factor 2.

5.1.7 Monte Carlo comparison

To verify the results found in the previous sections a Monte Carlo (MC) study has been performed with the PYTHIA generator described in section 3.5. This MC was used to generate Λ^0 hyperons which are detected with the HERMES spectrometer and for the LW. The first study addresses the improved invariant mass spectrum shown in figure 5.11. The mixed event spectrum is subtracted from the invariant mass spectrum found in the data to obtain the distribution of measured Λ^0 events. In figure 5.12 the resulting distribution is represented by the solid circles. The histogram represents the result from the MC where only Λ^0 events were generated. This MC histogram is normalized to the data. One can see that the two distributions have a comparable width and shape.

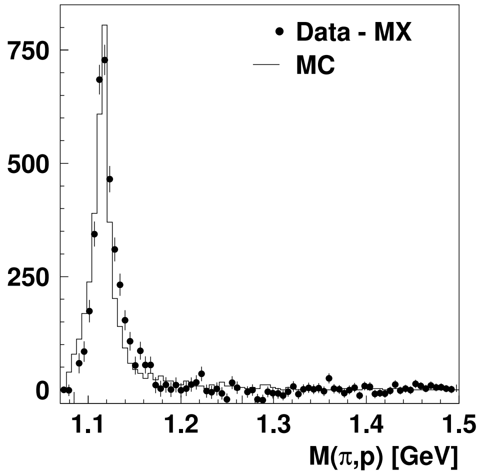

Figure 5.12: The comparison of MC results to data for the (π,p) invariant mass spectrum shown in figure 5.11 after subtraction of the mixed event background.

The second variable studied is the angle β. In figure 5.13 on the left the distribution for the angle β is shown. The data are represented by the open histogram while the MC and mixed event background are represented by hatched histograms. The MC histogram is normalized with the same factor as used in figure 5.12.

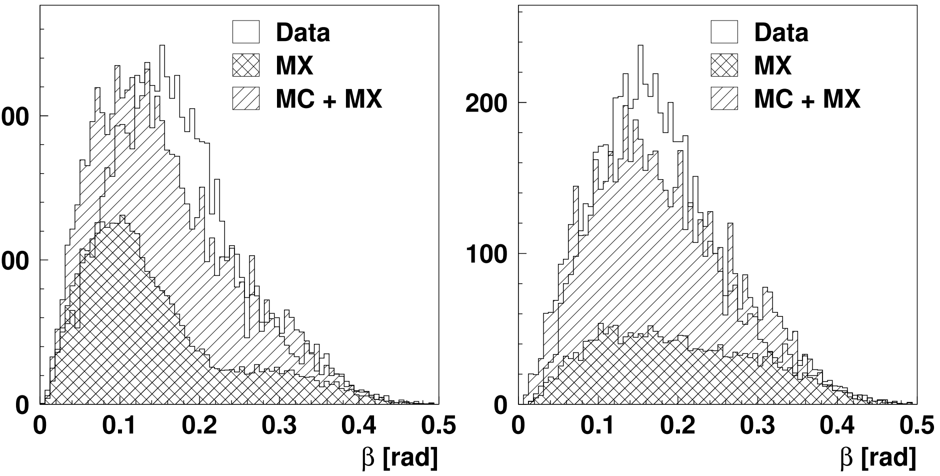

Figure 5.13: Comparison of the MC results to data and mixed event distributions of the angle β. On the left the mixed event spectrum is used as before. On the right an extra cut is applied to the data which is discussed discussed in the text.

In the β distribution for the mixed event background shown on the left in figure 5.13 an excess is seen as compared to the data between 0 and 0.15 rad. This excess causes a deficit of events in this region after subtraction from the data which is not seen in the MC. It is found that this excess of events in the mixed event background is due to tracks coming directly from the beam line. These tracks contribute significantly to the mixed event sample and are mainly due to interactions with the beam pipe. Because these tracks originate from the beam their DCA to the HERMES z-axis is smaller than 0.5 cm. Therefore a cut is introduced to discard events for which the DCA to the beam of both pion and proton track is less than 0.4 cm. With this cut the figure on the right in figure 5.13 is obtained. One can see that the excess between 0 and 0.15 rad is reduced. As a result the spectrum of the data after subtraction of the mixed event background is seen to be much closer to the spectrum found in the MC. The cut on the DCA to the beam for both the pion and proton track does not reduce the number of Λ^0 events since only events in the mixed event background are affected and only a minor effect on the shape of the mixed event invariant mass distribution is found at values below 1.1 GeV in invariant mass.

The same comparison has been carried out for the angle α, the proton momentum p_p and pion momentum p_π which are shown in figure 5.14. The most distinctive discrepancy can be seen in the momentum distribution of the proton. For momenta below 3 GeV the MC is in excess of the data. This is likely due to inefficiencies of the RICH particle identification which are not implemented in the MC. It is shown in [9] that these inefficiencies

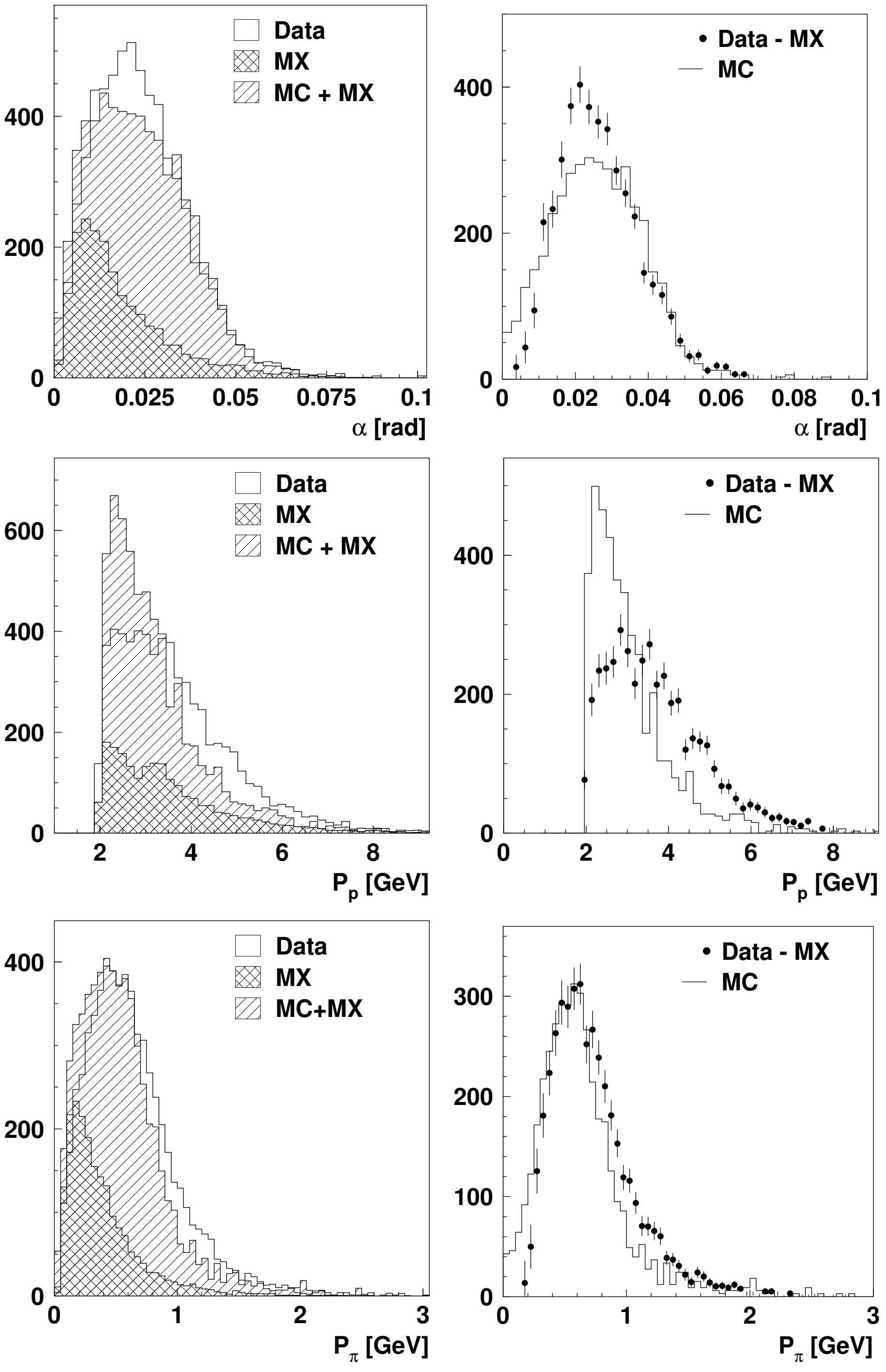

Figure 5.14: Comparison of data, mixed event and MC distributions for the angle α, the proton momentum and pion momentum. The solid circles in the panels on the right represent the data after subtraction of the mixed event spectrum.

for the identification of protons with momenta below 3 GeV is about 50%. As a result the MC overestimates the data below 3 GeV and is, because of the imposed normalization, underestimating the data above this limit.

Otherwise agreement between the data and MC is found, which enables the use of the MC to determine the kinematic variables which are not accessible in the data when the scattered beam lepton is not detected. This is used in the next chapter where the measured Λ^0 polarization has to be related to the average kinematics of the data.

5.1.8 Λ^0 Yields in the unpolarized data

Because the use of LW track parameters for both the pion and the proton has proved to give a major improvement in the invariant mass spectrum the data sets with and without lepton are each split in four parts to make a comparison possible. The Λ^0 yields from these four data sets are presented in table 5.2 where the pion is detected in the LW and the proton is always a long track detected in the spectrometer. The first data set represents the total data set without any constraints on the proton as was shown in figure 5.9. In the second data set the proton is also detected in the LW but the HRC track parameters are used. In the third data set the proton is once more required to be detected in the LW but in this case the LW track parameters are used. In the fourth data set the proton is not detected in the LW and therefore only the HRC track parameters are available. Note that the first data set is the sum of the second and fourth, while the second and third data set are the same but only the track parameters of the proton differ.

In the data set without detected lepton the selection of events where the proton is detected in the LW improves the Λ^0/ Total ratio from 0.17 up to 0.32, which rises up to 0.36 when the LW track parameters are used for the proton track. Even though the third data set represents only 32 % of the total data set (listed in the 2nd column) the Λ^0 yield is increased and the Λ^0/ Total ratio doubled. These improvements are less significant in the data set with a detected lepton. This difference between the two data sets is due to the resolution of the primary vertex. In the case without the detected lepton the primary vertex is determined by the proton-pion plane which is much better defined when defined by two LW tracks.

The Λ^0 yields with the pion and proton detected in the spectrometer are given in table 5.3. In these data sets the proton is always a long track and the pion is also a long track in the 3rd column and a short track in the 4th column. The 2nd column is the result of the combined data set listed in the 3rd and 4th column.

$\pi \in \{\text{lw}\}$ without e	$p \in \{\text{long}\}$ long track	$p \in \{\text{long} \cap \text{lw}\}$ long track	$p \in \{\text{long} \cap \text{lw}\}$ lw track	$p \in \{\text{long} \backslash \text{lw}\}$ long track
Λ^0 yield	2114 (149)	2202 (107)	2474 (106)	701 (105)
Λ^0/Total	0.17 (0.01)	0.32 (0.01)	0.36 (0.01)	0.12 (0.02)
σ [MeV]	9.84 (0.99)	15.90 (1.03)	8.99 (0.54)	7.43 (1.29)

$\pi \in \{\text{lw}\}$ with e	$p \in \{\text{long}\}$ long track	$p \in \{\text{long} \cap \text{lw}\}$ long track	$p \in \{\text{long} \cap \text{lw}\}$ lw track	$p \in \{\text{long} \backslash \text{lw}\}$ long track
Λ^0 yield	396 (32)	212 (23)	195 (25)	192 (24)
Λ^0/Total	0.44 (0.03)	0.47 (0.04)	0.39 (0.04)	0.41 (0.04)
σ [MeV]	23.4 (3.0)	21.8 (3.3)	20.8 (3.6)	26.0 (5.2)

Table 5.2: Λ^0 yields obtained from the LW data and the ratio of Λ^0 events to the total number of events (Λ^0+BG) under the invariant mass peak in a window of $\pm 3\sigma$. The errors indicated are statistical errors. The type of events used are described in the text. The total number of DIS events is 1.87 M with a luminosity of 43.2 ± 1.7 pb^{-1}.

$p \in \{\text{long}\}$ without e	$\pi \in \{\text{long} \cup \text{short}\}$	$\pi \in \{\text{long}\}$	$\pi \in \{\text{short}\}$
Λ^0 yield	13793 (140)	6585 (95)	6880 (104)
$\Lambda^0/(\Lambda^0$+BG)	0.825 (0.003)	0.842 (0.005)	0.775 (0.005)
σ [MeV]	2.68 (0.03)	2.41 (0.04)	2.88 (0.05)

$p \in \{\text{long}\}$ with e	$\pi \in \{\text{long} \cup \text{short}\}$	$\pi \in \{\text{long}\}$	$\pi \in \{\text{short}\}$
Λ^0 yield	529 (25)	265 (18)	264 (16)
$\Lambda^0/(\Lambda^0$+BG)	0.809 (0.016)	0.768 (0.025)	0.852 (0.020)
σ [MeV]	2.74 (0.13)	3.01 (0.23)	2.41 (0.17)

Table 5.3: Λ^0 yields and the ratio of Λ^0 events to the total number of events under the invariant mass peak in a window of $\pm 3\sigma$. The errors indicated are statistical errors. The 2nd column represents the total data set with short and long pion tracks used, the 3rd and 4th column represent these two data sets separately. The total number of DIS events is 1.87 M with a luminosity of 43.2 ± 1.7 pb^{-1}.

The yields found in the MC can be compared to the yields found in the data. The number of reconstructed Λ^0 hyperons found in the MC if the same requirements are applied as in the data are scaled with the luminosity observed in the data. In the data set where the lepton is not detected the number of Λ^0 hyperons corresponding to the best result, shown in the 4th column of table 5.2, are used in the comparison. In the data set where the lepton is detected the result of the 2nd column of table 5.2 is used. The number of Λ^0 events found with the LW are corrected for the efficiency loss discussed at the end of section 4.4 which was found to be 79.2 ± 3.4 %. The results are shown in table 5.4.

		without e		with e	
		MC	DATA	MC	DATA
$p \in \{\text{long}\}$	$\pi \in \{\text{long}\}$	4123	6585 (95)	293	265 (18)
$p \in \{\text{long}\}$	$\pi \in \{\text{short}\}$	10504	6880 (104)	327	264 (16)
$p \in \{\text{long}\}$	$\pi \in \{\text{lw}\}$	12928	3124 (189)	661	500 (46)

Table 5.4: Comparison of the absolute yields in data and MC for all different data samples discussed above.

In this comparison a difference can be seen between between the yields predicted by the MC and those obtained in the data. The MC predicts an increasing yield with decreasing momenta of the pion and thus of the Λ^0, i.e. when going from high momentum long tracks to lower momentum LW tracks. This increase is not observed in the data. Although part of the difference could be attributed to deficiencies in the MC simulation, it is more likely caused by the extrapolations to lower momenta in the MC where PYTHIA is not tuned properly. In the data set without detected lepton the predicted LW yield by the MC overestimates the data by a factor 4 compared to the data, while in the data set with a detected lepton the prediction is closer to the data. In the thesis by A. Reischl [9] a detailed comparison of the measured Λ^0 yield and other hyperon yields to those predicted by the PYTHIA MC is presented. It should be noted that the data analysis performed in [9] uses the data taken in the year 2000 during which a low threshold in the calorimeter was used (1.4 GeV). This lower threshold in the trigger condition results in a higher Λ^0 yield per luminosity unit. Furthermore, the MC used in [9] includes various additions to realistically simulate the observed efficiency in the HERMES spectrometer. Therefore a somewhat different data/MC comparison is found.

The relatively large MC overestimate of the Λ^0 yield in the kinematic range covered by the LW has two important consequences. On the one hand it demonstrates a relatively poor understanding of the hyperon production mechanism as encoded by PYTHIA. On the other hand the polarization measurements carried out with the LW will suffer from substantially larger error bars.

In the next section the LW reconstruction method is applied to the polarized target data.

5.2 Data analysis with target magnetic field

This section describes the reconstruction method used to analyze the data which were taken with the transverse target magnet (TM) switched on. First the effect of the TM on the reconstruction of Λ^0 hyperons is discussed. The correction method for spectrometer tracks is explained in the second part of this section. This correction method is then applied to data which are described in the third part of the section where the improvements and Λ^0 yields are given. A determination of the efficiency of the correction method is presented in the fourth part and a background description using a mixed event method is the subject of the fifth part. The analysis using the LW tracks are discussed in the last subsection where the resulting yields are presented.

5.2.1 Effect of the TM

When the TM is switched on the tracks of all charged particles which traverse the magnetic field are deflected. If the decay of the Λ^0 takes place inside this magnetic field the tracks of the decay proton and pion are bent. Since there is no measurement of the tracks inside the target magnetic field one has to use the existing track information available in the front region, as described in section 3.2.1, outside the range of the target magnetic field where the tracks are straight. With these track parameters one has to calculate the correct position of the decay vertex and the correct angle between the tracks in this vertex to obtain the correct invariant mass of the Λ^0 hyperon.

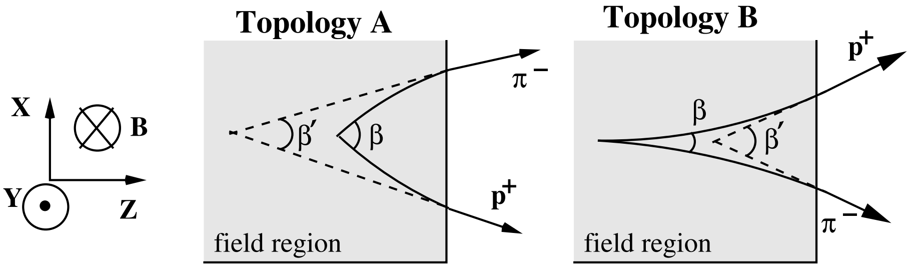

Figure 5.15: A sketch of the tracks of Λ^0 decay particles in the transverse target magnetic field. The solid curves indicate the path of the decay products traversing the magnetic field. The final section of these curves represent the position where they are measured outside the target magnetic field. The dashed lines are the extrapolated straight lines from these measurements.

Since the magnetic field is pointing in the negative vertical direction only the components of the track in the horizontal plane are affected. When looking in this horizontal plane there are two distinct topologies for Λ^0

decays inside the magnetic field as sketched in figure 5.15. Here the curved solid lines represent the tracks as bent by the magnetic field. The final part indicated by the arrow represents the straight track in the field-free region behind the TM where they are measured. The dashed lines represent the naive extrapolation from these straight tracks into the magnetic field. On the left topology A is shown where the horizontal slope of the pion is larger than that of the proton. In this topology the tracks are bent towards each other which results in a larger angle β between the bent tracks compared to the angle β' between the extrapolated straight tracks. From formula 5.1 for the calculation of the invariant mass it is clear that when the straight tracks are used in this topology the angle β' between the straight tracks will be too small which results in a too small invariant mass. Topology B shown on the right in figure 5.15 shows the opposite situation where the horizontal slope of the pion is smaller than that of the proton. In this case the invariant mass using the straight tracks is too large as the angle β' in this topology is larger than the real angle β between the bent tracks.

From these sketches it is also clear that not only the angle between the tracks is different when using the bent or straight tracks, but also the position of the decay vertex is different. This position is used for the vertex separation cut, but even more important is its use in the LW track reconstruction method. In this method the vertices determine the angle α. In figure 5.4 it was shown that the resolution in the angle α was the dominating factor in the reconstructed invariant mass. Hence, it is anticipated that the TM will have an effect on the resolution obtained with track reconstruction with the LW method. This is further explored in the last part of this section.

When the straight line extrapolation is used to calculate the invariant mass of (π, p) pairs in the presence of a target magnetic field the spectrum in figure 5.16 is obtained. This invariant mass spectrum is obtained with spectrometer tracks using the measured momenta and track parameters outside the magnetic field. Here events are selected with the position of the decay vertex at $z < 28$ cm which is inside the magnetic field as can be seen from the TM field map shown in figure 3.1. The mass peak has a width of 10 MeV which is a factor of 4 larger compared to the width of the mass peak in the unpolarized target data set which was 2.6 MeV. One can also see that the peak is split around the PDG value of the Λ^0 and a double peak structure appears. This is due to differences between the two topologies A and B described above. By evaluating the spectrum separately for the two relative sizes of the pion and proton slopes the two additional histograms of figure 5.16 are obtained. The invariant mass is systematically under- or overestimated, respectively, as can be seen from the peak positions of the dashed histograms.

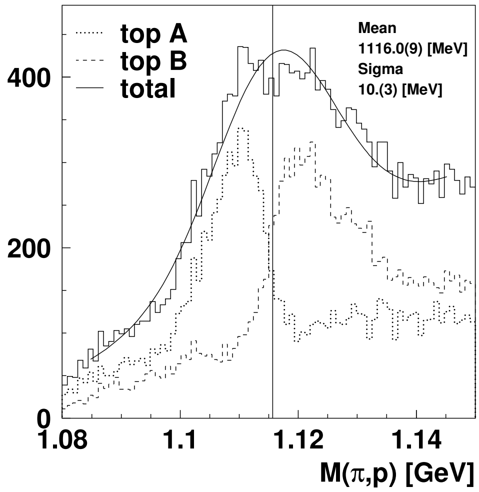

Figure 5.16: Invariant mass spectrum of spectrometer tracks using the measured track parameters and momentum for tracks which have a vertex inside the target magnetic field (decay vertex $z < 28$ cm). The spectra for the two topologies are also shown separatly.

In the following section a correction method is described which will improve the result obtained with the straight track extrapolation.

5.2.2 Correction method

The correction method applied to the front track measurements is based on an approximation of the TM field by a constant field inside a rectangular box. In this 'constant box field' approximation the bending of the tracks in the horizontal plane is described by circles. The curvature of these circles can be calculated from the momentum of the tracks and the strength of the field. The box field is defined in space by a boundary at a fixed z position which separates the space where the tracks are curved from the field free area where tracks are considered straight.

The extrapolation of the measured straight tracks at the boundary plane of the box field defines the track parameters at the border of the box field. Together with the calculated curvature the track parameters in the horizontal plane inside the box field are defined. This is indicated by the dashed lines in figure 5.17. From the curved tracks in the field the vertex in the horizontal plane can be calculated for each track, as represented by the open circles in the figure. Since the vertical slope of the tracks is not changed by the magnetic field the track parameters can be calculated in the vertex position and the corrected invariant mass is obtained.

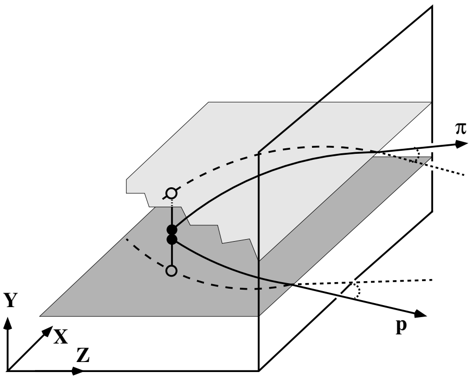

Figure 5.17: An illustration of the correction method described in the text.

The vertical position of the vertex can be different for the two tracks as is illustrated by the closed circles in figure 5.17. This vertical position can be calculated for each track using the vertical slope of the track and the distance on the curved track between the vertex and the position of the track on the boundary of the box field. The distance between the vertical positions of the vertex for both tracks can be used as a selection criterion similar to how the DCA was used in the case of straight tracks.

The effectiveness of this correction method is studied in appendix A where a method is developed to determine the optimal values for the position of the boundary (zfield) and the strength (Bfield) of the field. From this study the optimal values for the Bfield and zfield parameters in the data are found to be 0.32 T and 34.0 cm respectively.

5.2.3 Yields

With the optimal values for the box field approximation defined, the correction method can be applied to tracks which have a vertex inside this box field. In figure 5.18 the invariant mass peak is shown for such events. The kinematic cuts applied to the data are listed in table 5.5. The full histogram represents the result obtained with the correction method applied. The dashed histogram is the result without applying the correction. The peak in the full histogram is fitted with a Gaussian plus a first order polynomial to describe the background. The vertical line indicates the PDG value of the Λ^0. The mass resolution of the Λ^0 invariant mass peak is improved with a factor 3.6.

proton PID	requiring a non-pion in the RICH
	positive charge
	quality factor for RICH identification > 0
Tracking	primary vertex -18 cm$< z < +18$ cm
	decay vertex $z < 34$ cm
	vertical DCA < 2.0 cm
Λ^0 topology	vertex separation > 2 cm
	opposite charge for pion and proton
	momentum of the pion is smaller than that of the proton

Table 5.5: Cuts used in figure 5.18 for obtaining the (π, p) invariant mass spectrum using spectrometer tracks with the target magnetic field correction applied.

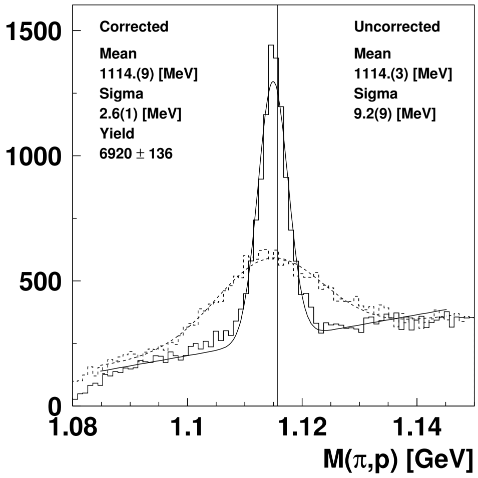

Figure 5.18: The (π, p) invariant mass spectrum obtained with (solid) and without (dashed) the correction method. The peak is fitted with a gaussian plus a first order polynomial to describe the background. The vertical line indicates the PDG value of the Λ^0.

When the background is subtracted by using the parameters of the polynomial fit a yield of 6920 ± 136 Λ^0 events is found for proton-pion track pairs which have a decay vertex $z < 34$ cm.

The events which have a decay vertex $z > 34$ cm are used to obtain figure 5.19. In this data set straight tracks could be used because this is the field free region. Again the peak is fitted with a Gaussian plus a first order polynomial to fit the background. After background subtraction with the fit parameters of the polynomial a Λ^0 yield of 9140 ± 102 is found. The much lower level of background in this data set is due to the implicit vertex separation cut resulting from the selection of the decay vertex at $z > 34$ cm.

These results for the spectrometer tracks are summarized in table 5.6.

	Mean [MeV]	Sigma [MeV]	Yields
In field	1114.9±0.1	2.61±0.06	6920±136
Outside field	1115.9±0.1	2.60±0.03	9140±102

Table 5.6: Λ^0 yields obtained from the polarized target data. The total number of DIS events is 1.56 M

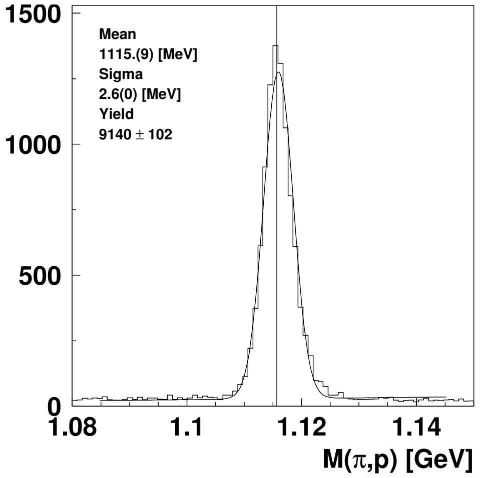

Figure 5.19: The invariant mass spectrum for events which have a decay vertex at $z > 34$ cm where straight tracks are used. The peak is fitted with a gaussian plus a first order polynomial to describe the background. The vertical line represents the PDG value of the Λ^0-mass.

5.2.4 Efficiency

In order to estimate the efficiency loss due to the correction method applied on the polarized data two studies are presented. In figure 5.20 the distribution of Λ^0 events as a function of the z-position of the decay vertex is shown for all reconstructed events within a window of $\pm 3\sigma$ around the book value of the Λ^0. The vertical line represents the value of zfield which separates the events for which the correction is applied ($z < 34$ cm) from those where straight tracks are used ($z > 34$ cm). Only a minor drop can be seen for values close to $z \approx 34$ cm.

In order to compare absolute yields of the polarized data set with those obtained in the unpolarized data set the effect of the calorimeter threshold in the trigger condition used has to be eliminated. For the polarized data taking the calorimeter threshold was low, 1.4 GeV, while during the unpolarized

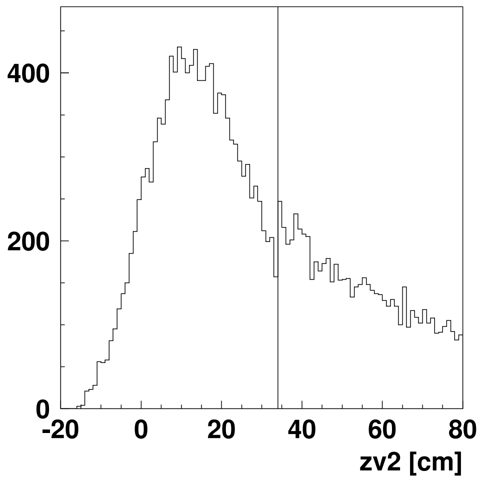

Figure 5.20: The distribution of all reconstructed (π,p) events within a window of $\pm 3\sigma$ around the book value of the Λ^0as a function of the z-position of the decay vertex. The vertical line represents the separation between the corrected ($z < 34$ cm) and uncorrected events ($z > 34$ cm).

data taking a high threshold of 3.5 GeV was used to reduce the dead time due to the higher trigger rate caused by the higher density of the target. In order to eliminate this effect only events with a DIS lepton are considered. This DIS lepton will always deposit more than 3.5 GeV in the calorimeter which removes the selection of the calorimeter threshold. In table 5.7 the relevant numbers are summarized for the polarized and unpolarized data analyzes. From the Λ^0/DIS ratio shown in this table an efficiency loss of 9% ± 6% can be derived for the polarized target data as compared to the unpolarized ones.

	DIS events [M]	Λ^0	Λ^0/DIS [10^{-3}]
Unpolarized target	1.87	529 ± 25	0.283 ± 0.013
Polarized target	1.56	401 ± 21	0.257 ± 0.014

Table 5.7: Comparison of the Λ^0 yield in the data taken with an unpolarized and polarized target obtained with spectrometer tracks. Only events with a DIS lepton are considered to eliminate the effect of using a different threshold setting in the trigger condition.

5.2.5 Mixed Events

In order to correct for background contributions the mixed event method described in section 5.1.5 is applied. This method has the advantage over a polynomial fit of the background that the phase space of the Λ^0 peak is expected to be more realistic. The long and short track data samples are considered separately as was done in the unpolarized target analysis. Because the background level in the spectra with the Λ^0 decay vertex outside the target magnetic field is very low this data set is added to the corrected data with a decay vertex inside the field.

The result of this analysis can be seen in figure 5.21 where the hatched histograms represent the mixed event spectrum which is normalized in the mass regions indicated by the horizontal lines. The top panels show the result for short tracks where the right hand picture zooms in on the region around the Λ^0 peak. The bottom panels show the result for the long tracks.

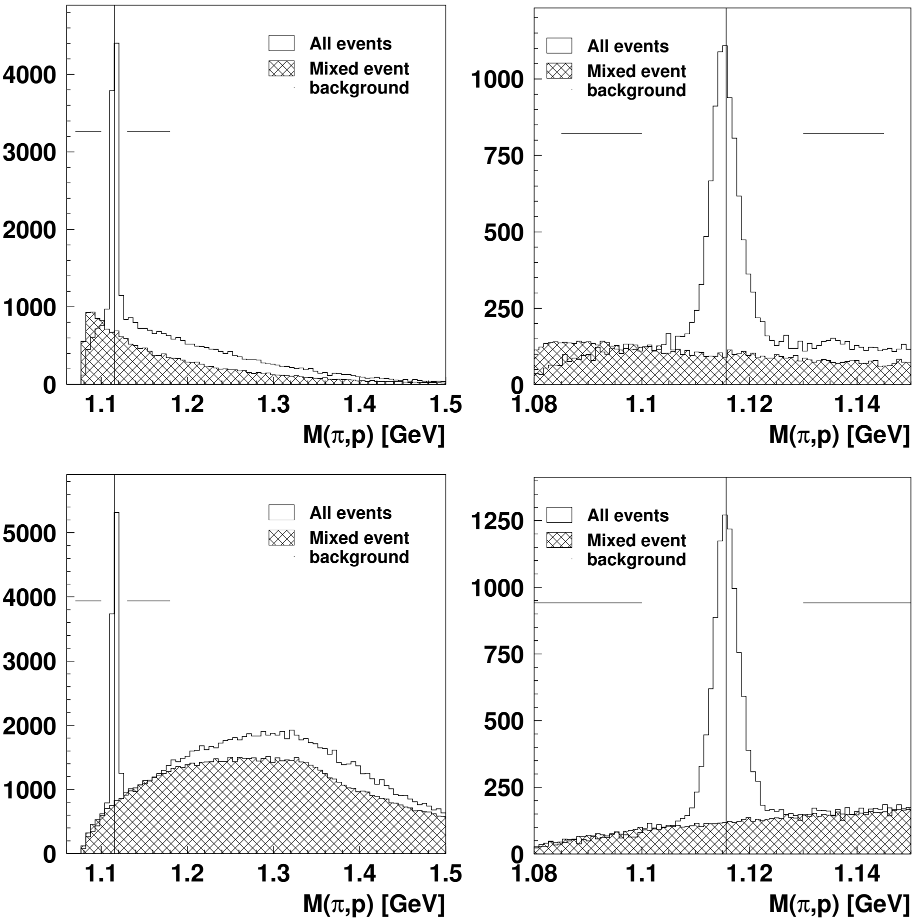

Figure 5.21: Invariant mass spectra for spectrometer tracks with the mixed event background shown as the hatched distribution. The top panels represent the short track sample, the bottom panels show the long track data set. On the right the same distributions are shown but zoomed in on the Λ^0 mass peak.

It is clear that the mixed event spectra do not fit the shape of the background very well. This can be understood by considering the principles of the mixed event method. The mixed event method describes the combinatorial background in spectra that result from the probability that random track combinations still pass the applied cuts. The mixed event spectra describe a given background well when two criteria are fulfilled. The first one is that the background in the unmixed data spectra is mainly due to combinatorial background and the second is that the initial angular distributions and momentum distributions of the tracks are preserved. For the polarized target the second criterion is not valid anymore. The method to correct for the effect of the TM is based on the anzats that both tracks originate from a Λ^0 hyperon. For mixed event data this anzats is not valid. Therefore, the initial track distributions of the mixed event data set are no longer correctly described which leads to the discrepancy seen in the invariant mass spectra.

5.2.6 LW Method

The method for correcting the effect of the TM has been developed in section 5.2.1 for spectrometer tracks. This method cannot be applied directly to the LW tracks because these tracks have no direct measurement of their momentum. Therefore a different approach has to be taken. Using the Monte Carlo a new method is developed. The momentum of the LW track is varied between its the maximum momentum, which is the momentum of the proton track, and a minimal momentum of 100 MeV. By varying the momentum the radius of curvature is varied and therefore the position of the decay vertex is changed. The convergence criterion is that the vertical distance between the vertex on both tracks is minimal for a certain value of the momentum of the LW track.

To check the validity of this method a data set where the pion track is detected in both the spectrometer and the LW is used. However, only 45% of the events which are selected as Λ^0 events in the present analysis using both spectrometer tracks converged to a solution.

This is due to both the angular resolution of the spectrometer (of about 1.3 mrad) and the small difference in y-slope between the two tracks as can be seen in figure 5.22. The resolution of the projection points on the boundary of the constant box field is 0.6 mm and 0.85 mm for the vertical distance between the two points. As seen from figure 5.22 68% of the trackpairs has a difference in y-slope of less than 0.045 which results in a resolution on the difference in y of 0.45 mm per cm in z. Therefore the criterion for the correction method with LW tracks is not sensitive enough and cannot be used.

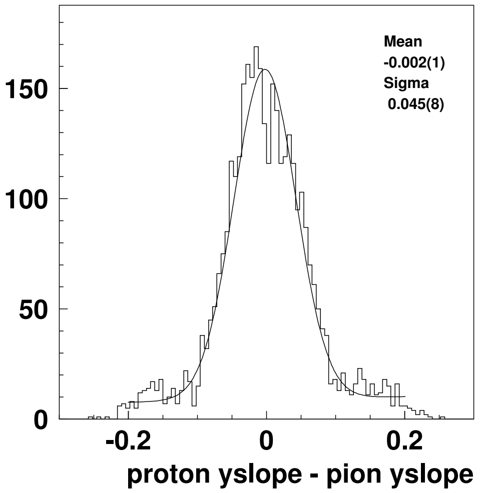

Figure 5.22: The difference in y-slope of proton and LW tracks.

When the LW track data are analyzed using straight tracks it is found that only events with a decay vertex larger than 15 cm in z can be used. In figure 5.23 one can see in the top left panel the invariant mass spectrum found with LW tracks for events with a decay vertex between 10 and 15 cm. The mixed event background overlaps the spectrum of the data completely which makes a subtraction impossible. In the top right panel the same data set is shown where the decay vertex has a value between 15 and 20 cm. Here the mixed event background is lower than the data. The data set with a decay vertex between 15 and 45 cm is shown in the lower left panel. The peak with of 24 MeV is larger than for the unpolarized target data (9 MeV) because of the target magnetic field.

When the events in the subtracted spectrum shown in the bottom right panel in figure 5.23 are counted in a window of ±3 sigma a yield of 2525 ± 85 is found in a data set of 1.56 M DIS events. This result is obtained without a correction for the target magnetic field and with the use of a mixed event background which is also not corrected for the magnetic field. As can be seen from the shape of the mixed event distribution and the fit of the subtracted spectrum, this result is not yet optimized.

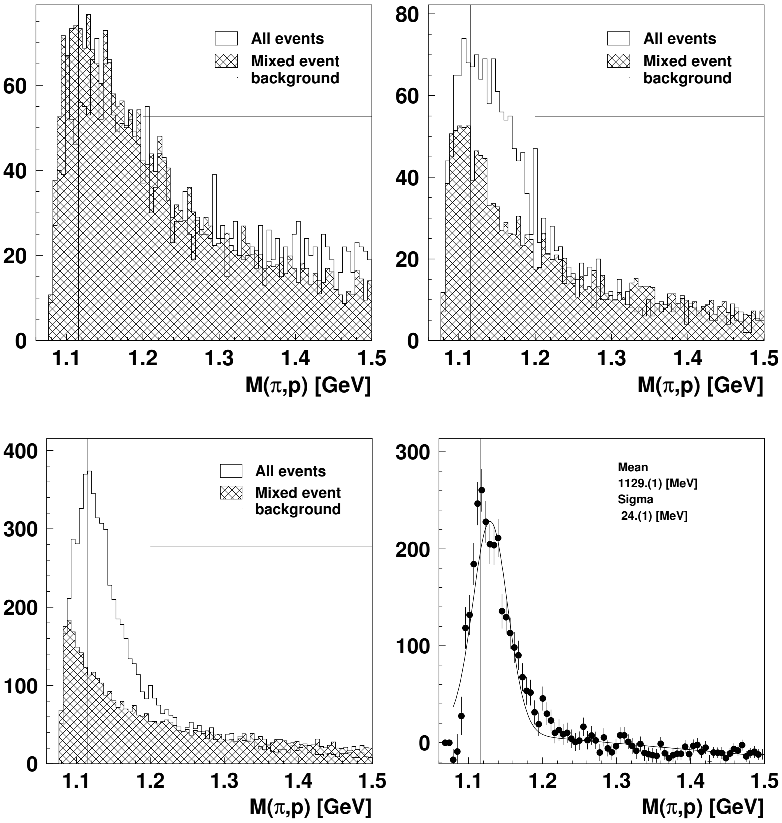

Figure 5.23: The invariant mass spectra for LW tracks. The events with a decay vertex in different intervals is shown together with the mixed event background. Top left [10-15 cm], top right [15-20 cm], bottom left [15-45 cm], bottom right shows the subtracted spectrum corresponding to the bottom left panel.

5.3 Conclusions

It has been proved that with the use of the LW Λ^0 hyperons can be reconstructed despite the absence of a momentum measurement in this detector. A new method has been discussed which enables the calculation of the Λ^0 hyperon invariant mass using the proton momentum and PID information from the spectrometer and the track parameters for the proton and the pion measured using the LW.

In the data without a target magnetic field the resolution of the invariant mass obtained with the LW is a factor 4 larger than that obtained with the spectrometer. It is found that this is consistent with the expectations based on the characteristics of the two methods and also with MC simulations.

The background can be described using a mixed event data set. A comparison with the existing HERMES MC was carried out for the shape of the invariant mass spectra and several relevant variables characterizing the Λ^0 reconstruction. The MC describes the angular distributions rather well but overestimates the lower region of the proton momentum spectrum. This overestimate is also found in the comparison of the Λ^0 yields where the number of low momentum Λ^0 particles is strongly overestimated by the MC simulation.

For data obtained with a target magnet field a correction method is developed for spectrometer tracks which results in invariant mass spectra with comparable resolutions as in the data obtained without a target magnetic field. This correction method cannot be applied to LW tracks because of the absence of a momentum measurement. In this data set only those Λ^0 particles can be reconstructed which decay in the region where the target magnetic field is lower or absent.

Chapter 6

Λ^0 Hyperon polarization

The final goal of the research work described in this thesis is to measure the polarization of Λ^0 hyperons with the use of the Lambda Wheels (LW) in the HERMES spectrometer. The experimental determination of the Λ^0 polarization is based on the weak decay $\Lambda^0 \rightarrow p + \pi^-$. In this decay the angular distribution of the proton in the Λ^0 center of mass (c.m.) system is not isotropic because the proton is preferentially emitted in a direction along the spin of the Λ^0. The angular distribution of these decay protons is described by

$$\frac{dN}{d\Omega} = \frac{dN_0}{d\Omega}(1 + \alpha P_\Lambda \cos\theta), \tag{6.1}$$

where $dN/d\Omega$ represents the angular distribution of all protons from Λ^0 decays, $dN_0/d\Omega$ is the distribution of protons originating from unpolarized Λ^0 particles, α is the parity violating coefficient also called the analyzing power which is known to be 0.642 ± 0.013, P_Λ is the polarization of the Λ^0 and θ is the angle between the direction of the momentum of the proton in the Λ^0 c.m. frame and the polarization vector of the Λ^0.

This chapter describes determinations of the Λ^0 polarization measured with either an unpolarized target and a longitudinally polarized beam, or a transversely polarized target and an unpolarized beam. The longitudinal component of the Λ^0 polarization is measured by evaluating the angle of the proton in the Λ^0 c.m. frame with respect to the direction of the Λ^0 measured in the laboratory frame as shown in figure 6.1. This chapter discusses such polarization measurements using the LW. This is the first time that an analysis of this kind is performed. Three different methods to obtain the longitudinal Λ^0 polarization are presented and applied to the data. The polarization of the background events is also determined. The relevant kinematic variables associated with the Λ^0 polarization events are introduced and taken from the HERMES MC if they cannot be obtained from the measured data. The resulting polarization values are compared to polarization values of Λ^0 hyperons reconstructed with the use of long and short tracks observed in the spectrometer.

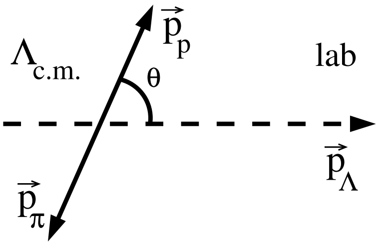

Figure 6.1: Schematic illustration of the angle θ between the proton in the Λ^0 center of mass frame (c.m.) and the direction of the Λ^0 in the laboratory frame.

In the last section of this chapter the Λ^0 polarization along the spin direction of a transversely polarized target, is presented. In this case, the polarization of the Λ^0 is proportional to the polarization of the target. It can therefore be measured with an unpolarized beam and a transversely polarized target. Otherwise, the method used to determine the Λ^0 polarization is quite similar to that used in the longitudinal case.

6.1 Longitudinal $\boldsymbol{\Lambda^0}$ polarization

For the determination of the longitudinal Λ^0 polarization three data sets are used which were discussed in the previous chapter in section 5.1. These three data sets always contain a proton as a long track detected in the spectrometer and a pion which is detected in three different ways namely as a long track, a short track or a LW track. For the case where the pion is detected in the LW the proton is also required to be observed in the LW as this enables the use of the track parameters determined by the LW for both the pion and the proton which yields the most accurate Λ^0 reconstruction (figure 5.11). If the beam lepton is also detected the Λ^0 yield in the LW is too small to provide a useful polarization measurement. For that reason only data without detected beam lepton are used in this chapter. A recent HERMES paper [5] provides detailed results for long and short tracks for a data set that includes the scattered beam lepton. These data are not further discussed here.

6.1.1 The $\cos\theta$ distribution

In order to measure the longitudinal Λ^0 polarization the $\cos\theta$ distribution needs to be evaluated. As was mentioned before, this is the distribution of the cosine of the angle between the proton in the Λ^0 c.m. frame and the Λ^0 direction in the laboratory frame.

The $\cos\theta$ distributions presented in figure 6.2 are obtained from the two data sets with both the pion and the proton track reconstructed with the spectrometer. Only those events are used that fall within a window of $\pm 3\sigma$ (where $\sigma = 2.4$ MeV for long tracks and $\sigma = 2.9$ MeV for short tracks) around the Λ^0 book mass.

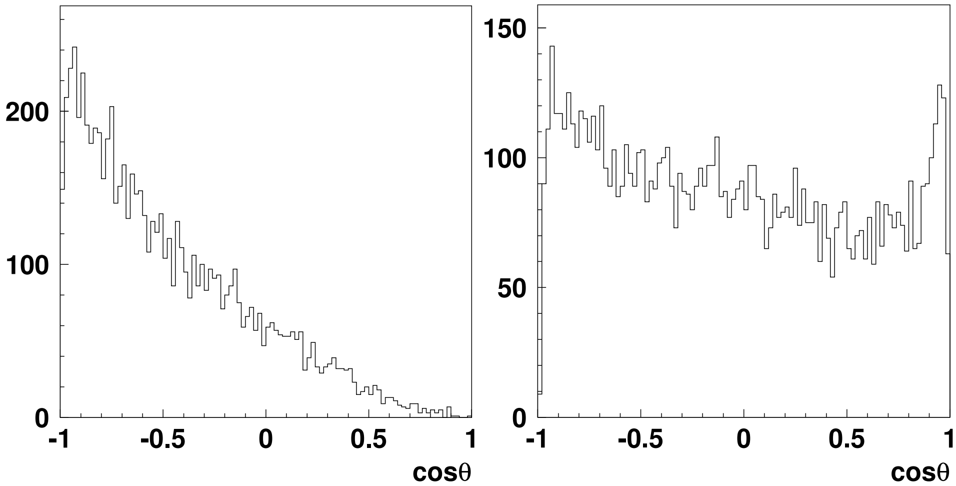

Figure 6.2: The $\cos\theta$ distributions obtained with spectrometer tracks. On the left both the pion and proton are reconstructed as long tracks, on the right the proton is a long track and the pion a short track. The measured angle θ is illustrated in figure 6.1.

On the left the data are shown where both the pion and the proton are observed throughout the entire spectrometer and reconstructed as long tracks. One can see that the distribution is asymmetric and tilted towards negative values of $\cos\theta$. This shape is due to the spectrometer acceptance. When the pion is reconstructed as a long track its momentum has to be sufficiently high to pass through the spectrometer magnet and still be detected in the tracking chambers in the back of the spectrometer. Having a higher momentum the pion is more likely to point in the forward direction in the Λ^0 c.m frame. Under these conditions the proton is typically moving in the direction opposite to that of the Λ^0 in the c.m. frame, i.e. where $\cos\theta < 0$. If, on the other hand, the proton and the Λ^0 are co-linear, i.e. $\cos\theta > 0$, the pion typically has a small momentum and may fall below the threshold.

This explains the asymmetric shape of the distribution towards negative values of $\cos\theta$. On the right side of figure 6.2 the $\cos\theta$ spectrum for the data set where the proton is a long track and the pion is a short track is shown. For short tracks the pion is deflected by the spectrometer magnet over a relatively large angle, as it does not reach the tracking detectors in the back part of the spectrometer. Hence, its momentum is smaller than in the long track sample. Therefore the $\cos\theta$ spectrum is more symmetric.

For events reconstructed with the LW only those events are selected which fall within a $\pm 3\sigma$ window around the Λ^0 book mass where $\sigma = 9$ MeV. The obtained $\cos\theta$ spectrum is shown in figure 6.3.

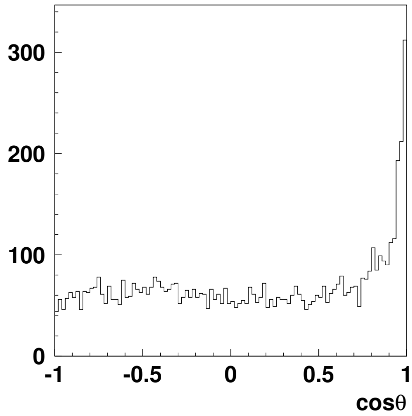

Figure 6.3: The $\cos\theta$ spectrum of Λ^0 events reconstructed with the LW.

Here, one can see an almost flat $\cos\theta$ distribution with a sharp peak at values close to $\cos\theta = 1$. In order to understand this distribution a simple simulation has been performed. The Λ^0 particles are generated with a varying scattering angle between 0 and 0.2 rad and an azimuthal angle between 0 and 2π to approximately simulate the LW acceptance. The θ distribution of the proton in the Λ^0 c.m. frame was simulated isotropically. As expected the resulting $\cos\theta$ spectrum obtained from the analysis of this simulated data set is uniform as can be seen on the left in figure 6.4. When the effect of a finite momentum resolution of 150 MeV is added to the momentum of the pion the $\cos\theta$ spectrum on the right in figure 6.4 is obtained.

This can be understood when considering the low momentum of the pions reconstructed with the LW method (typically below 1 GeV, see figure 5.14). These small pion momenta correspond to a topology where the proton is almost parallel to the Λ^0 and will therefore correspond to an angle θ very close to zero in the Λ^0 c.m. frame. Events of this kind are responsible for the peak at $\cos\theta = 1$ in the LW data.

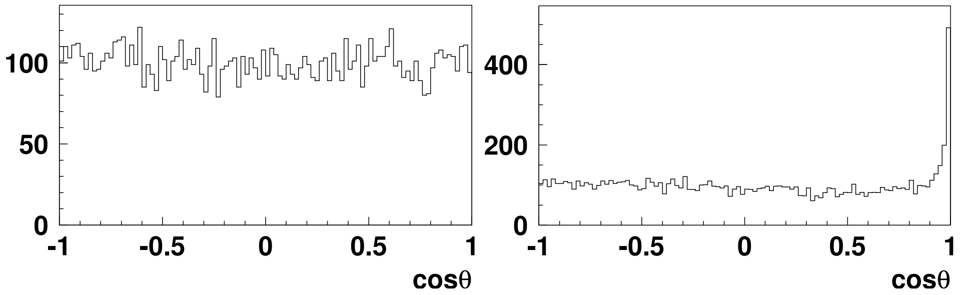

Figure 6.4: The $\cos\theta$ distributions obtained from a simulation where the angular distribution of the proton in the Λ^0 c.m. is isotropical. On the right the effect of a finite momentum resolution of 150 MeV is taken into account.

The assumed resolution of 150 MeV for the pion momentum is in agreement with an assumed resolution of 3 mrad for the angle α as can be verified using equation 5.2. It is concluded that the shape of the $\cos\theta$ distribution for events reconstructed with the LW is understood with an asymmetry near $\cos\theta = 1$ caused by the resolutions typical for this reconstruction method.

6.1.2 Helicity balanced method

In order to measure the Λ^0 polarization one has to know, apart from the $\cos\theta$ distribution, the angular distribution of the protons originating from unpolarized Λ^0 particles denoted by $dN_0/d\Omega$ in formula 6.1. Because the longitudinal Λ^0 polarization originates from the longitudinal polarization of the beam it is possible to obtain this unpolarized Λ^0 distribution when an unpolarized beam is used. This is accomplished by flipping the helicity of the beam on a regular basis, and adding the data of both beam helicities together such that the luminosity weighted average beam polarization equals zero. This technique is known as the helicity balanced method and is described in detail in [62, 63].

The helicity balanced method can only work if the acceptance of the detector does not change during the whole data taking period. In order to verify that no artificial polarization effects have occurred, it has been studied whether the average particle momenta changed over time. This is important as the momentum measurement of the decay particles is crucial for the determination of the Λ^0 polarization. The average measured proton momentum was checked over time and found to vary over a certain period of time during the 2004 data taking. The source of this fluctuation was not found but is believed to be an experimental problem which occurred in specific periods during the year 2004. As a workaround all runs contained within a single fill[1] for which the average proton momentum was higher than 200 MeV as compared to the average of 4.7 GeV of all runs were discarded[2].

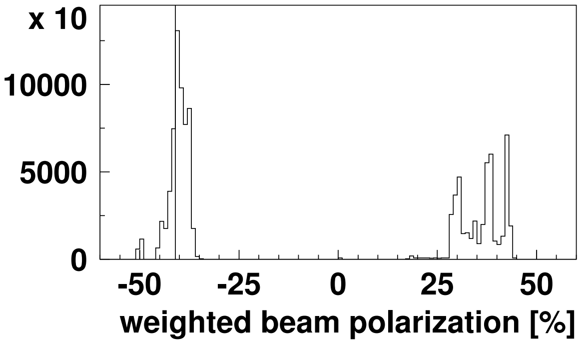

Figure 6.5: The weighted beam polarization where DIS events are used as weight.

	Total data set			Balanced data set		
	negative helicity	total	positive helicity	negative helicity	total	positive helicity
polarization	-40.3%	-7.2%	35.9%	-39.1%	-0.1%	35.9%
DIS events	589647	1041752	452105	417646	8697512	452105

Table 6.1: Polarization and DIS events for the total and the helicity balanced data sets.

The helicity balancing has been applied to the thus reduced data sets. To apply the helicity balanced method the luminosity of the data sets needs to be determined. In this analysis the number of DIS leptons is used as a weight. In figure 6.5 the weighted beam polarization for the total data set is shown. The vertical line indicates the lower limit of -41.01% which is used to balance the data set. All events on the left side of the line are discarded. The relevant statistics are given in table 6.1. It was chosen to discard events with polarization values less than -41.01% to obtain a larger data sample.

6.1.3 Fit $\cos\theta$

As can be seen from formula 6.1 the Λ^0 polarization depends linearly on $\cos\theta$. Therefore the $\cos\theta$ spectrum can be fitted with a straight line to extract the Λ^0 polarization. Because the $\cos\theta$ spectrum also depends on the acceptance of the detector one should first correct for possible false

---

[1] A fill is defined as the period of time in between the moment when particles are injected in the storage ring and the moment when the beam is dumped.

[2] After the removal of these runs the RMS of the average proton momentum per run was found to be 77 MeV.

asymmetries caused by acceptance effects. This can be done by dividing the $\cos\theta$ spectrum of a certain beam helicity with that of the whole helicity balanced data set. The polarization can then be obtained using the following fit function:

$$F(\cos\theta) = B + A\cos\theta \tag{6.2}$$

where $F(\cos\theta)$ is the acceptance corrected $\cos\theta$ spectrum and A and B are the parameters of the linear fit[3]. The resulting polarization is obtained as:

$$P_\Lambda = \frac{1}{\alpha}\frac{A}{B}. \tag{6.3}$$

An example of such a fit can be seen on the left in figure 6.6. The resulting polarization values for the two beam helicities are given on the right for long, short and LW tracks. The measurements obtained with negative beam helicities have been displayed with reversed sign because the beam-induced Λ^0 polarization is of opposite sign if the beam helicity is flipped. Also, the average of the two measurements is shown.

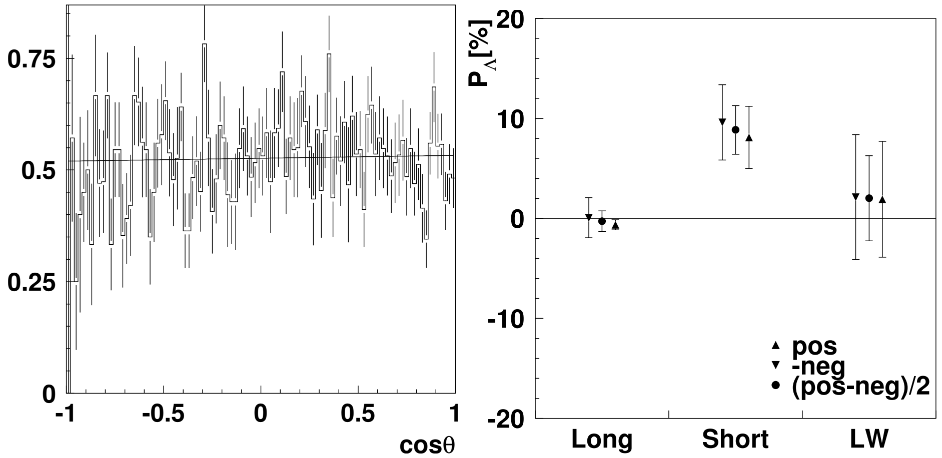

Figure 6.6: On the left: an example (taken from the LW data) of a fitted $\cos\theta$ spectrum which is corrected for the acceptance. On the right: the resulting longitudinal Λ^0 polarization for the two beam helicities and their average for long, short and LW tracks.

The indicated errors are those obtained from the fit parameters. The error bars of the long track data set are relatively small due to the large asymmetry

---

[3] This approach is used somewhat differently by the NOMAD [6] and E665 [7] collaborations as they extracted the $\cos\theta$ distribution for the unpolarized Λ^0 sample from an unpolarized MC study.

in the $\cos\theta$ spectrum illustrated in figure 6.2. For positive values of $\cos\theta$ the statistics is very low. Hence the fit is mainly determined by the bins with a negative $\cos\theta$ which contain a substantial number of counts thus enabling a relatively precise determination of P_Λ. For the short and LW tracks the method gives somewhat larger error bars.

6.1.4 Moment method

Instead of a fit of the $\cos\theta$ distribution, the 'moment method' of [62] can also be used. Also in this case a sample with a weighted beam polarization equal to zero is required. In this method the detector acceptance cancels in a more analytical way. The moment method starts from formula 6.1 written as:

$$\frac{dN}{d\Omega} = \frac{dN_0}{d\Omega}(1 + \alpha P_\Lambda^i \cos\theta_i) \qquad i = x, y, z. \tag{6.4}$$

Summation over identical indices is assumed. It is noted that the orientation of the angle θ changes if a different component of the Λ^0 polarization needs to be calculated. The following moments are introduced:

$$\begin{aligned}
\langle\cos\theta_i\rangle &= \frac{\int \cos\theta_i \frac{dN}{d\Omega} d\Omega}{\int \frac{dN}{d\Omega} d\Omega} & (6.5)\\
\langle\cos\theta_i\rangle^0 &= \frac{\int \cos\theta_i \frac{dN_0}{d\Omega} d\Omega}{\int \frac{dN_0}{d\Omega} d\Omega} & (6.6)\\
\langle\cos\theta_i \cos\theta_j\rangle^0 &= \frac{\int \cos\theta_i \cos\theta_j \frac{dN_0}{d\Omega} d\Omega}{\int \frac{dN_0}{d\Omega} d\Omega}. & (6.7)
\end{aligned}$$

With these moments the formula for the polarization of the Λ^0 can be rewritten as [62]:

$$\langle\cos\theta_i\rangle^\pm = \frac{\langle\cos\theta_i\rangle^0 + \alpha P_\Lambda^j \langle\cos\theta_i \cos\theta_j\rangle^0}{1 + \alpha P_\Lambda^j \langle\cos\theta_j\rangle^0} \qquad i, j = x, y, z. \tag{6.8}$$

The brackets $\langle\rangle^\pm$ indicate an average which is taken over all events with positive (+) or negative (-) beam polarization, while the index 0 refers to the unpolarized Λ^0 sample and corresponds to the average over the whole data set which has an average beam polarization of zero.

For a 4π acceptance the $\cos\theta$ distribution for unpolarized Λ^0 events is uniform. This would imply that the unpolarized moments $\langle\cos\theta_i\rangle^0$ are zero for all directions $i = x, y, z$ and that the matrix $\langle \cos\theta_i \cos\theta_j \rangle^0$ would be diagonal with diagonal elements $\langle \cos^2\theta_x \rangle^0 = \langle \cos^2\theta_y \rangle^0 = \langle \cos^2\theta_z \rangle^0 = 1/3$. Under these assumptions the Λ^0 polarization could be directly calculated by evaluating the average of the $\cos\theta$ distribution as:

$$\langle \cos\theta_i \rangle = \frac{\alpha}{3} P_\Lambda^i \qquad i = x, y, z. \tag{6.9}$$

When $\langle \cos\theta \rangle$ is calculated for the z component this corresponds to the longitudinal Λ^0 polarization. This approximative method has been applied to the three data sets for which the results are shown in figure 6.7. The average value for $\cos\theta$ is calculated for the two different beam helicities and the total helicity balanced data sample.

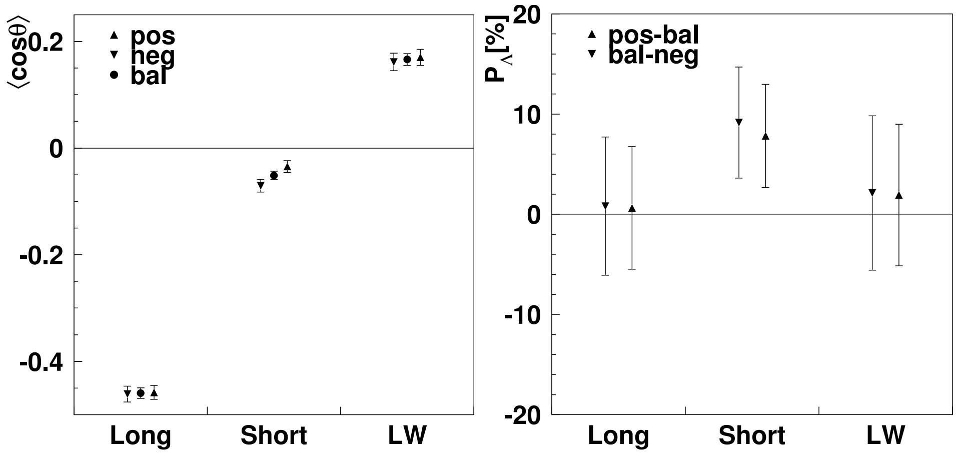

Figure 6.7: On the left, the average value of $\cos\theta$ for the z component of the Λ^0 polarization for long, short and LW tracks, for positive and negative beam helicity states and the whole helicity balanced data set are shown. On the right, the longitudinal Λ^0 polarization assuming a 4π acceptance is displayed.

One can see that the average for the helicity balanced data set in all three cases is not equal to zero, which should be the case in an ideal 4π acceptance. The offset with respect to zero in the case of long and short tracks can be attributed to the selected non-uniform momentum range covered by the HERMES acceptance. In the case of the LW tracks the positive offset is most likely related to the peak at values close to $\cos\theta = 1$ shown in figure 6.3. When these offsets are subtracted the Λ^0 polarization can be calculated using formula 6.9, corrected for acceptance effects. The results are shown on the right of figure 6.7. The results of this approach are consistent with the results obtained from the fit of the $\cos\theta$ spectrum discussed in the previous section.

Instead of assuming a perfect 4π acceptance the z component of formula 6.8 can also be written explicitly as:

$$P_\Lambda^{z\pm} = \frac{\langle z\rangle^0 - \langle z\rangle^\pm}{\alpha(\langle z\rangle^\pm\langle z\rangle^0 - \langle zz\rangle^0)} + \frac{\langle xz\rangle^0 - \langle z\rangle^\pm\langle x\rangle^0}{\langle z\rangle^\pm\langle z\rangle^0 - \langle zz\rangle^0} P_\Lambda^x + \frac{\langle yz\rangle^0 - \langle z\rangle^\pm\langle y\rangle^0}{\langle z\rangle^\pm\langle z\rangle^0 - \langle zz\rangle^0} P_\Lambda^y \tag{6.10}$$

where the shorthand notation $\langle\cos\theta_i\rangle = \langle i\rangle$ with $i = x, y, z$ is used. This is only one of the three possible equations which can be obtained from formula 6.8 but it is the only one which has a first term depending only on averages of the longitudinal z component. All other averages are very small compared to the one in z as can be seen in table 6.2 where all values for the averages are given for the LW track data sample. Furthermore, only the first term in equation 6.10 contributes significantly since the second and third terms are proportional to the polarization components in x and y [4].

	$\langle x\rangle$	$\langle y\rangle$	$\langle z\rangle$
+	0.048 ± 0.012	-0.024 ± 0.018	0.170 ± 0.015
−	0.039 ± 0.012	-0.054 ± 0.019	0.161 ± 0.016
0	0.043 ± 0.008	-0.038 ± 0.013	0.166 ± 0.011

$\langle xz\rangle^0$ = -0.0185 $\langle yz\rangle^0$ = 0.0136 $\langle zz\rangle^0$ = 0.3440

Table 6.2: The values of the $\cos\theta$ averages $\langle x\rangle, \langle y\rangle$ and $\langle z\rangle$ used in equation 6.10 for the different beam helicity states $+, -$ and 0 of the LW data sample.

With the use of formula 6.10, called the moments method, the longitudinal Λ^0 polarization can be obtained for the long, short and LW tracks for positive and negative beam helicities. The results are shown in figure 6.8. Also for this method the results are consistent with the measurements discussed above. The measured Λ^0 polarization as obtained from the data set with negative beam helicity is found to be slightly larger than in the data set with positive beam helicity. This can be attributed to the larger beam polarization of the negative beam helicity data set (see table 6.1). It is noted that for the beam-induced longitudinal Λ^0 polarization, P_Λ, the measured value is proportional to the beam polarization. This dependence is divided out when discussing the longitudinal spin transfer $D_{LL'}^\Lambda$ in the next chapter.

---

[4] The transverse polarization of the Λ^0 measured in HERMES [64] with spectrometer tracks is found to be $0.054 \pm 0.005(\text{stat}) \pm 0.015(\text{syst})$.

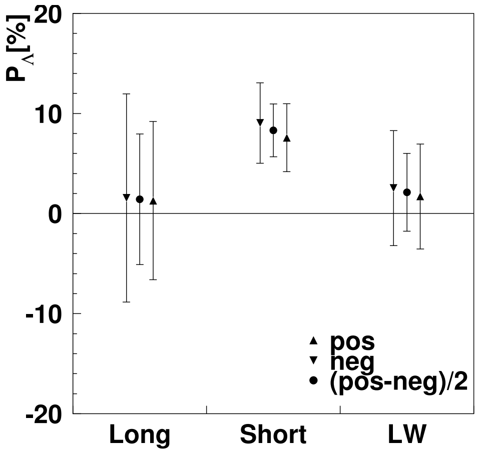

Figure 6.8: Λ^0 polarization values obtained with the moment method encoded by equation 6.10. Note that the results obtained with a negative beam helicity have been displayed with a reversed sign.

6.1.5 Background polarization

The polarization measurements described in the previous sections were always carried out using all events within a fixed invariant mass range of $\pm 3\sigma$ from the center of the Λ^0 peak. These events are mostly Λ^0 events but there is always a number of background events included in the selected data. In this section the polarization of the background events is studied with the moments method described in the previous section.

One has to be careful in calling the result of any of the extraction methods discussed above an actual polarization. This is only true in case a sample is used that exclusively consists of Λ^0 decays. For a mixed event data set or in an invariant mass range outside the Λ^0 invariant mass peak this is no longer valid. The result of a polarization measurement in this case is an asymmetry which has no physical meaning because all the steps taken from the measurement of the track parameters and the particle momenta in the laboratory frame to the measurement of the angle θ in the Λ^0 rest frame are performed under the assumption that a Λ^0 decay has occurred. For simplicity reasons the term polarization is still used both in the case of a Λ^0 decay and for background measurements where only the resulting asymmetry is meant.

In figure 6.9 several measurements of background polarizations are shown. The average polarization measured with positive and negative beam helicities is determined for three different sets of events. The open symbols denote the polarization obtained from the mixed event data set (mx). The closed symbols indicate that real data were analyzed. The squares represent the polarization in an invariant mass range outside the Λ^0 peak. This range is referred to as the sidebands and includes the invariant mass range from 1.07 GeV to 1.105 GeV and from 1.13 GeV to 1.18 GeV for both the long and short track data sets. For the LW data set the range above the Λ^0 peak was chosen from 1.18 GeV to 1.5 GeV because the resolution is worse in this case. The circles in figure 6.9 represent the polarization of the events within a window of $\pm 3\sigma$ around the book value of the Λ^0 mass.

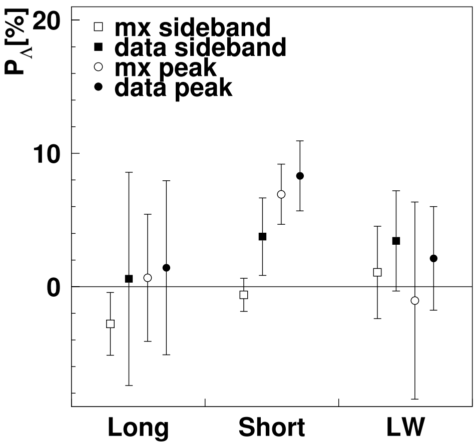

Figure 6.9: The polarization in different invariant mass ranges for long, short and LW tracks. Open symbols represent mixed event data, closed symbols the real data. The squares indicate the sidebands while the circles indicate the $\pm 3\sigma$ region around the Λ^0 book mass.

For long tracks and LW tracks all three possible background polarizations are consistent with each other and with zero. In the short track sample the spread of the three background polarizations is larger, but just consistent with each other. While the polarization value derived from the mixed event data and the sideband data yield a somewhat higher background polarization at the 5 % level, the sidebands in the mixed event data sample yield a value close to 0 %.

6.1.6 Background Subtraction

It is important to correct for possible false asymmetries in the data that yield non-zero polarization values for the background events located under the invariant mass peak of the Λ^0 hyperon sample. In the method chosen to correct for such false asymmetries the polarization values obtained with the mixed event method for the events in the same invariant mass window as the data are subtracted from the measured polarization of the real data. If one assumes that the total polarization of all events under the invariant mass peak (P_{total}) is composed of the polarization of the real Λ^0 hyperons (P_Λ) and the polarization of the background (P_{BG}) one can write

$$P_\Lambda N_\Lambda + P_{\text{BG}} N_{\text{BG}} = P_{\text{total}} N_{\text{total}} \tag{6.11}$$

where N represents the number of events. From this equation the polarization of the Λ^0 hyperon can be derived:

$$P_\Lambda = \frac{P_{\text{total}} N_{\text{total}} - P_{\text{BG}} N_{\text{BG}}}{N_{\text{total}} - N_{\text{BG}}}. \tag{6.12}$$

By applying this formula to the data the polarization values shown in figure 6.10 are obtained. All relevant values for the polarization and the number of events are listed in table 6.3.

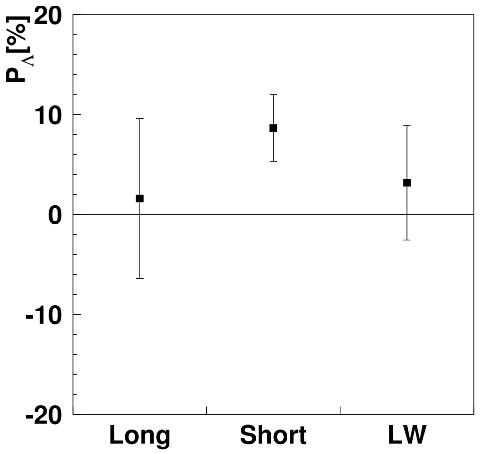

Figure 6.10: The longitudinal Λ^0 polarization with the background polarization obtained from the mixed event data set under the Λ^0 mass peak subtracted.

	Long	Short	LW
P_{total}	1.4% ± 6.5%	8.3% ± 2.6%	2.1% ± 3.9%
N_{total}	3951 ± 63	5271 ± 73	2770 ± 53
P_{BG}	0.7% ± 4.8%	6.9% ± 2.3%	-1.0% ± 7.4%
N_{BG}	674 ± 26	1057 ± 32	688 ± 26
P_Λ	1.6% ± 8.0%	8.6% ± 3.3%	3.2% ± 5.7%

Table 6.3: The polarizations and yields of the three data sets for all events (total) in a $\pm 3\sigma$ window around the book value of the Λ^0 and for the mixed events (BG) in this same window. Also the resulting Λ^0 polarization is given.

The number of background events N_{BG} has been obtained for each data set by fitting the mixed event data sample to the data in the invariant mass intervals corresponding to those of the sidebands. It has been chosen to use the mixed event background polarizations obtained for events within the same invariant mass window as the real data ($\pm 3\sigma$ around the Λ^0 book mass) for the background subtraction procedure as this sample contains data belonging to exactly the same acceptance (in momenta and angular ranges) as the real data. This argument does not apply to the two sideband estimates discussed above.

6.1.7 Systematic studies

As this is the first time that LW polarization data are presented, the results have been subjected to a number of systematic studies to -hopefully- verify the consistency of the results obtained.

These studies included pion momenta selections to exclude unrealistically low values artificially introduced due to the limited momentum resolution of the LW method. Also proton momentum selections were performed to maximize the efficiency of the tracking and PID algorithms. The PID requirement was made more restrictive to eliminate all possible contributions of backgrounds originating from a false PID of the proton. Several LW modules were disabled in the analysis to eliminate the possibility of a varying LW acceptance due to a loss in efficiency. A MC study simulation of polarized Λ^0 decays has been carried out to study possible geometric effects of the LW acceptance. None of these studies yielded effects that were not found to be correctly compensated in the analysis discussed above.

So far the polarization was always studied in a $\pm 3\sigma$ window around the book mass of the Λ^0 or in the sidebands. As another systematic study this window was changed and the polarization outside this window was evaluated. It was found that the polarization measured in the mass range of 1.142 GeV to 1.18 GeV, i.e. outside the $\pm 3\sigma$ window, has an unexpectedly high value of $37\% \pm 6\%$. None of the aforementioned studies could identify the origin of this asymmetry.

Alternatively, the possibility of a contamination from $\Lambda(1520)$ decay was considered. This hyperon decays via the channel $\Lambda(1520) \rightarrow p + K^-$ and can be a possible source of background in the Λ^0 spectrum as no distinction can be made between pions and kaons for LW tracks. Moreover, the yield of $\Lambda(1520)$ hyperons is relatively large [65]. The $\cos\theta$ distribution of the $\Lambda(1520)$, measured in the same way as in the case of the Λ^0 hyperon, is not symmetric and depends on the helicity of the beam as observed by [66]. Such an artificial asymmetry could have been misinterpreted as a large polarization. To investigate whether this is plausible, it has been investigated whether the (π, p) pairs reconstructed with the LW could give rise to a $\Lambda(1520)$ invariant mass peak if all pions are treated as kaons. Such an analysis yielded no significant signal around the book mass of the $\Lambda(1520)$. Also when this study was applied to the short track data set, despite the better mass resolution, no $\Lambda(1520)$ signal could be observed. Although [65, 5] indicate a relatively large production ratio between $\Lambda(1115)$ and $\Lambda(1520)$ of about 3:1 the absence of a $\Lambda(1520)$ signal is probably due to the cuts applied to the data. Especially the vertex separation cut reduces the $\Lambda(1520)$ yield significantly because of its prompt decay.

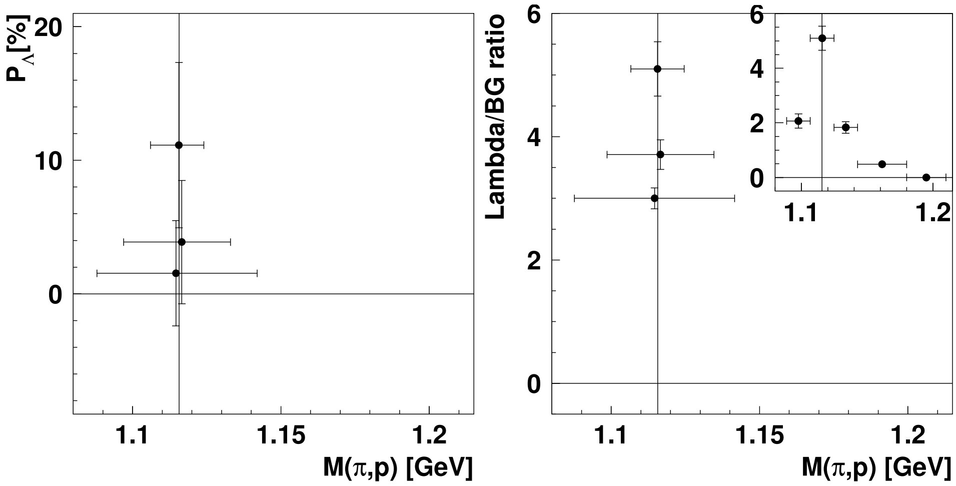

Figure 6.11: On the left: the measured Λ^0 polarization with the use of the LW in different windows around the Λ^0 book mass. The three points correspond to windows of $\pm 1\sigma$, $\pm 2\sigma$ and $\pm 3\sigma$ with $\sigma = 9$ MeV. On the right: the Λ^0 to background ratio as a function of the Λ^0 invariant mass with an insert showing this ratio in different invariant mass bins.

Finally it has been investigated to what extend P_Λ changes if the window around the Λ^0 book mass is changed. The results are shown on the left of figure 6.11. The three measurements correspond to $\pm 1\sigma$, $\pm 2\sigma$ and $\pm 3\sigma$ windows where $\sigma = 9$ MeV. The three data points are consistent with each other although a somewhat higher polarization for the $\pm 1\sigma$ window is obtained. This can possibly be attributed to the Λ^0 to background ratio, seen on the right hand side of figure 6.11, which is much higher for the $\pm 1\sigma$ window as compared to the wider ranges. The inserted picture on the right hand side represents the Λ^0 to background ratio for different invariant mass bins.

Apart from the statistical uncertainty, the obtained polarization value carries a systematic uncertainty. The systematic uncertainty consists of two parts: that related to experimental effects, and that related to the method used. Following [5] the first part amounts 0.4 %. On the basis of the studies mentioned before, we estimate the second part to be about 4 %. Taken together the Λ^0 polarization measured by the LW can be quoted as $3.2 \pm 5.7 \pm 4.0$ %.

6.1.8 Kinematics

With the PYTHIA Monte Carlo simulation discussed in section 5.1.7 it is possible to compare the average kinematic variables found in the data to those obtained from a simulation. Moreover, PYTHIA simulations provide an estimate of kinematic variables that cannot be measured. In table 6.4 the kinematic variables are listed as obtained from the MC and those derived from data which have the beam lepton detected. When the beam lepton is not detected these variables can only be extracted from the MC and are given in table 6.5.

	Long		Short		LW	
	MC	DATA	MC	DATA	MC	DATA
$\langle x_B \rangle$	0.076	0.083	0.082	0.091	0.098	0.101
RMS x_B	0.064	0.050	0.072	0.056	0.081	0.061
$\langle y \rangle$	0.63	0.60	0.60	0.55	0.55	0.52
RMS y	0.17	0.14	0.19	0.17	0.20	0.17
$\langle z \rangle$	0.47	0.47	0.35	0.39	0.34	0.36
RMS z	0.17	0.15	0.16	0.15	0.18	0.15
$\langle W^2 \rangle$[GeV^2]	31.3	29.5	29.5	27.0	27.1	25.4
RMS W^2[GeV^2]	9.2	7.4	10.4	8.8	10.9	8.6
$\langle Q^2 \rangle$[GeV^2]	2.2	2.2	2.1	2.1	2.4	2.2
RMS Q^2[GeV^2]	1.6	0.9	1.6	1.0	1.8	1.0
$\langle x_F \rangle$	0.36	0.32	0.17	0.19	0.13	0.12
RMS x_F	0.21	0.18	0.22	0.18	0.23	0.18

Table 6.4: The average kinematic variables from the PYTHIA Monte Carlo and from the data where the beam lepton was detected.

From the comparison shown in table 6.4 one can see that the MC and the data are in a reasonable agreement, which validates the use of the MC for the data without detected lepton. Also note that the average value of x_F, a key variable when discussing the longitudinal Λ^0 polarization data, decreases when going from the long track data set to the LW track data sample. However, it is also seen that the average value of x_F does not reach deeply into the negative x_F domain as was originally anticipated based on older versions of the MC [47]. The fact that less negative x_F values are reached can be attributed to a more steep decrease of the Λ^0 cross section with angle (or

	Long	Short	LW
$\langle x_B \rangle$	0.001	0.001	0.001
RMS x_B	0.002	0.003	0.003
$\langle y \rangle$	0.58	0.48	0.47
RMS y	0.21	0.22	0.23
$\langle z \rangle$	0.43	0.39	0.37
RMS z	0.17	0.19	0.19
$\langle W^2 \rangle$[GeV^2]	30.5	25.6	25.1
RMS W^2[GeV^2]	10.8	11.4	11.6
$\langle Q^2 \rangle$[GeV^2]	0.008	0.007	0.007
RMS Q^2[GeV^2]	0.018	0.017	0.016
$\langle x_F \rangle$	0.28	0.20	0.14
RMS x_F	0.19	0.21	0.22

Table 6.5: The kinematic variables from the PYTHIA Monte Carlo for events that do not contain a detected beam lepton.

negative x_F), also causing a substantial reduction in the yield as compared to previous MC-based estimates. In section 5.1.8 a similar observation was made when the Λ^0 yield was compared to MC estimates. In particular for the quasi-real photoproduction case (no detected beam lepton), the yield at large angles (or $x_F < 0$) is very low. This indicates that the hyperon production mechanism is still poorly understood.

With the x_F distributions determined in the MC it is possible to present the polarization values found for the long, short and LW data samples as a function of x_F. This result is shown in figure 6.12.

Here the three polarization measurements are shown on the left with their statistical errors. The horizontal bars represent the RMS value of the corresponding x_F distribution shown on the right. The x_F distributions on the right are normalized to the Λ^0 yield found in the data for each of the three data sets. From figure 6.12 it is concluded that the LW increase the Λ^0 yield as expected, but the increase towards negative x_F values does not go beyond $x_F \approx -0.2$.

In an attempt to decrease the average x_F value covered by a subset of the LW data that do not contain the detected lepton the correlation of x_F with other kinematic variables has been studied. A possible variable is the light-cone momentum fraction of the beam positron carried by the Λ^0[64]. It is denoted by ζ and is defined as

$$\zeta = \frac{E_\Lambda + p^z_\Lambda}{E_e + p_e}, \tag{6.13}$$

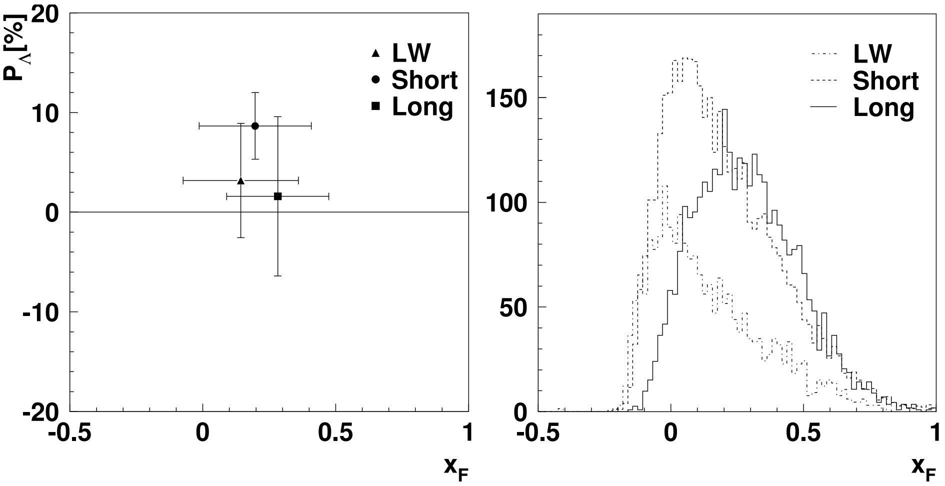

Figure 6.12: On the left the polarization values for the long, short and LW data sets as a function of the x_F value derived from the MC. The horizontal bar for each data point represents the RMS value of the distribution over which is integrated. The MC distributions in x_F on the right are normalized to the Λ^0 yield found in the data for each data sample.

where E_Λ and p^z_Λ represent the energy and z component of the Λ^0 momentum and E_e and p_e are the energy and momentum of the positron beam. A correlation plot of ζ versus x_F can be seen in figure 6.13.

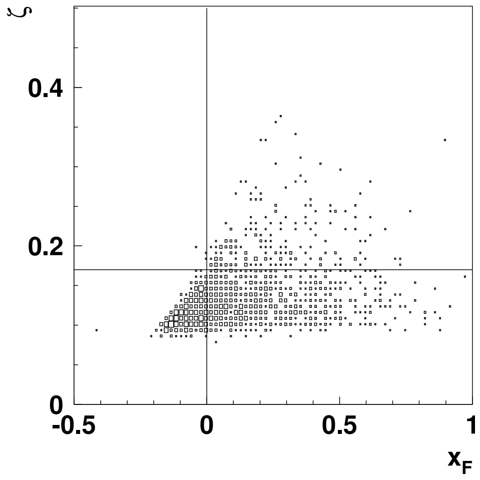

Figure 6.13: Correlation plot obtained from the PYTHIA MC for x_F versus ζ for the kinematics covered by the LW. The horizontal line indicates a possible limit on ζ to select only events with positive x_F ($\zeta > 0.17$) or to lower the average value of x_F ($\zeta < 0.17$).

The correlation between x_F and ζ is apparent but does not enable a clean separation between the positive and negative x_F regions. The correlation can be used to discard the negative domain of x_F by selecting events with $\zeta > 0.17$, as indicated by the horizontal line in figure 6.13, or to lower the average value of x_F by removing events with $\zeta > 0.17$. This selection of events will be applied in the next chapter where the polarization measurements are used to derive values of the spin transfer coefficient $D^{\Lambda}_{LL'}$ or the spin correlation coefficient C_{su}.

6.2 Λ^0 polarization with a transverse target

Part of the data have been taken with the transverse target magnet switched on. With these data it is possible to measure the Λ^0 polarization in the direction of the transversely oriented magnetic field of the target. The analysis is similar to that of the longitudinal Λ^0 polarization discussed in the previous section. Whereas the longitudinal Λ^0 polarization is induced by the polarization of the beam, the Λ^0 polarization discussed in this section is due to the transverse target polarization. Hence, in the former case the measured Λ^0 polarization is proportional to the original beam polarization, while in the latter case it is proportional to the target polarization.

Note that the direction of the Λ^0 polarization measured in this analysis is parallel to the field orientation of the transversely polarized target and should not be mistaken with the transverse Λ^0 polarization. This transverse Λ^0 polarization is a spontaneously arising polarization which can be observed with an unpolarized beam and an unpolarized target. The direction of the spontaneous transverse Λ^0 polarization is perpendicular to the production plane of the Λ^0.

Because the field direction of the target magnet is flipped every minute the data set is already balanced to within 0.0007%. The weighted target polarization for the complete data set is shown in figure 6.14 where DIS events were used as a weight. To eliminate the contribution of the longitudinal Λ^0 polarization component the weighted beam polarization was also selected to be zero in a similar way as was done in the longitudinal Λ^0 polarization analysis. It was also verified that the weighted beam polarization was zero for the positive and negative target polarization separately.

The moment method is used to obtain the Λ^0 polarization parallel to the target spin direction in the rest frame of the Λ^0 hyperon. This method not only takes into account effects due to the acceptance of the detector but also eliminates the contribution of the spontaneous transverse Λ^0 polarization because this spontaneous polarization does not depend on the direction of

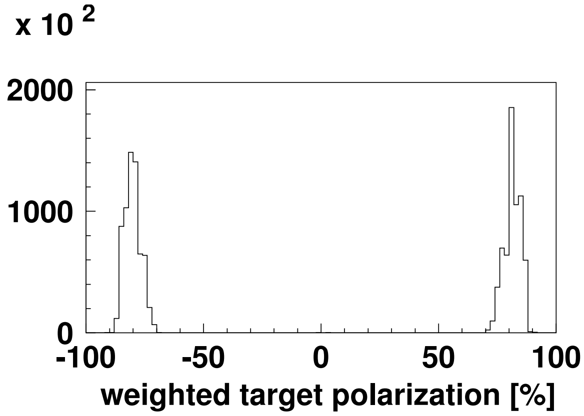

Figure 6.14: The weighted target polarization for the complete data set with a transversely polarized target where DIS events are used as a weight. The positive and negative target polarizations are respectively 81.4 % and -80.1 % with a total weighted average of $7 \cdot 10^{-4}$ %.

the target polarization and adds vectorially to the Λ^0 polarization parallel to the transverse target field.

The result of the moment method applied to the transverse polarized target data is shown on the left hand side of figure 6.15. It shows the different background determinations in the sidebands and the result of the mixed event data under the invariant mass peak. The events in the peak region were selected in a $\pm 3\sigma$ window around the Λ^0 book mass where $\sigma = 2.6$ MeV in case of the long and short tracks and $\sigma = 24$ MeV in the LW track data set. The sideband range for the long and short track sample covers the mass range from 1.07 GeV up to 1.105 GeV and from 1.13 GeV to 1.18 GeV, while in the case of the LW tracks the invariant mass range from 1.18 GeV up to 1.5 GeV is used. On the right side of this figure polarization values are presented after subtraction of the contribution of the mixed event background under the invariant mass peak. Also the result when a zero background polarization is subtracted is shown.

From the left hand side of figure 6.15 one can see that the different background determinations are consistent with each other in case of the long and short track data set. For the LW sample the background determined from the sideband results in higher values. This could be due to the invariant mass range of the sideband which is well above the book mass of the Λ^0 hyperon resulting in measured asymmetries which have little in common with the polarization value obtained from the data under the invariant mass peak of the Λ^0 hyperon. Furthermore, the absence of a correction for the bend tracks in the target magnetic field worsens the invariant mass resolution. As can be seen from figure 5.23 the Λ^0 mass peak determined with the LW is

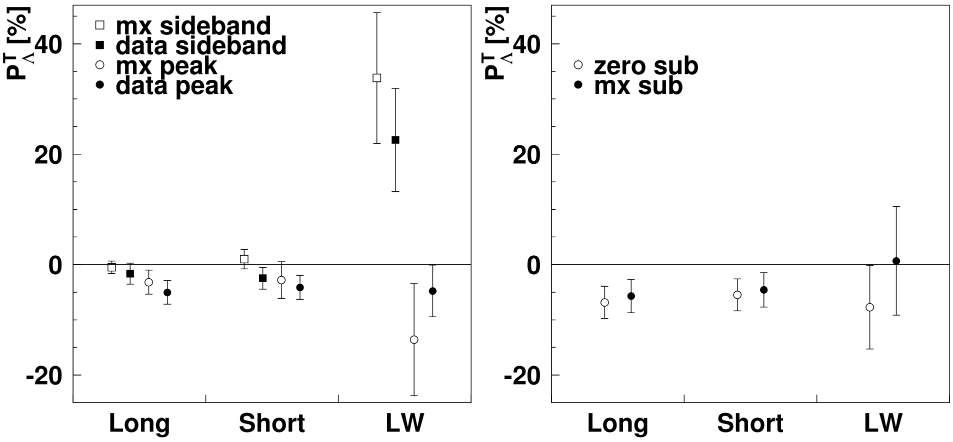

Figure 6.15: The polarization of the Λ^0 in the direction of the magnetic field of the transverse polarized target for long, short and LW tracks is shown. On the left uncorrected data obtained from the measurements (closed symbols) and a mixed event data sample (open symbols), for events under the invariant mass peak (circles) and those in the sidebands (squares) are shown. On the right, the results after subtraction of the mixed event background under the invariant mass peak (closed circles) and when a zero background polarization is subtracted (open circles) are displayed.

broader w.r.t. the unpolarized data which causes a distribution of the Λ^0 hyperon events, and background events, over a much broader invariant mass range.

From the results presented on the right hand side of figure 6.15 it is concluded that the background subtraction does not have a large effect on the spectrometer data, but does influence the LW result. However, when a background with zero polarization is subtracted the results are still consistent with each other. In each of the three different data sets a small negative polarization value is found.

6.3 Conclusions

In this chapter Λ^0 polarization measurements are presented. This polarization has been measured for the first time with the use of the Lambda Wheels and are compared to other Λ^0 polarization values as derived from long and short tracks reconstructed by the HERMES spectrometer.

The $\cos\theta$ distribution, which is a key element in polarization measurements, is understood. In the case of the spectrometer tracks the shape of the distribution is due to the limited acceptance. In the LW data set the shape is resembling that of a 4π detector except for an artifact close to $\cos\theta = 1$, which can be attributed to the finite momentum resolution encountered in the Λ^0 reconstruction method used.

Three different methods to obtain the longitudinal Λ^0 polarization were investigated and found to be consistent. The size of the longitudinal Λ^0 polarization is relatively small and similar to values obtained from spectrometer data.

The background contribution to the longitudinal Λ^0 polarization has been estimated with the use of a mixed event data set. The data have been corrected for this contribution.

The relevant kinematic variables have been studied in a PYTHIA MC and agree with those observed in data that include a detected beam lepton. This enables the use of this simulation for those data sets where the kinematic variables cannot be measured.

Also the polarization of the Λ^0 in the direction of the magnetic field orientation of the transversely polarized target has been measured. A similar method is used as in the longitudinal Λ^0 polarization measurement. Also in this case small polarization values were found.

These results are further discussed in the next chapter, where the physics interpretation of the measured Λ^0 polarization values are addressed.

Chapter 7

Interpretation of the data

With the measurements of the longitudinal Λ^0 polarization described in the previous chapter it is now possible to interpret these data in two ways. In the current fragmentation region the longitudinal spin transfer $D^{\Lambda}_{LL'}$ is related to the u-quark contribution to the spin of the Λ^0 hyperon. In the target fragmentation region the spin correlation coefficient C_{sq} can be obtained which is a measure of the relative orientation of the spin of the struck quark with respect to that of the s-quark in the target nucleon. These two subjects are discussed in section 7.1 and 7.2, respectively. Moreover, for those data where the Λ^0 polarization could be measured along the direction of the transversely polarized target it is possible to obtain information on the transversity distribution. This subject is discussed in section 7.3.

7.1 The Longitudinal Spin Transfer $D^{\Lambda}_{LL'}$

In order to enable the interpretation of the longitudinal Λ^0 polarization measurements in terms of the longitudinal spin transfer $D^{\Lambda}_{LL'}$ Λ^0 hyperons originating from the current fragmentation region have to be selected. Within the kinematic ranges covered by the HERMES experiment an absolute separation between the current and target fragmentation regions cannot be realized because the center-of-mass energy ($\sim$ 7 GeV) is relatively close to the proton mass resulting in overlapping distributions near $x_F \sim 0$ [15]. Furthermore, the kinematic variable x_F cannot be directly calculated for the Λ^0 polarization measurements presented in this work because the scattered beam lepton is not detected in coincidence with the reconstructed Λ^0 hyperon. However, a correlation between the light-cone momentum fraction ζ and x_F, shown in figure 6.13, obtained from a Monte Carlo simulation can be used. By selecting only those events with $\zeta > 0.17$ only those events with positive x_F are selected which leads to an enhancement of the number of Λ^0 hyperons originating from the current fragmentation region.

Using equation 2.13 the longitudinal spin transfer $D^{\Lambda}_{LL'}$ can be calculated as:

$$D^{\Lambda}_{LL'} = \frac{P^{\Lambda}_{L'}}{P_b D(y)}, \tag{7.1}$$

where P_b is the longitudinal polarization of the beam given in table 6.1 and

$$D(y) = \frac{1-(1-y)^2}{1+(1-y)^2} \tag{7.2}$$

is the depolarization factor which can be calculated using the average value for the kinematic variable y given in table 6.5 as obtained from the MC simulations. The resulting data for $D^{\Lambda}_{LL'}$ are presented in figure 7.1 together with previously published results [5]. These include results from the NOMAD [6] and E665 [7] experiments. The three solid points have been derived from the three P_Λ measurements shown in figure 6.10 and listed in table 6.3 after the selection $\zeta > 0.17$. In the bottom panel of figure 7.1 the mean and RMS values of the three different x_F distributions over which is integrated are shown. Note that the published results of the HERMES, NOMAD and E665 experiments have been derived from scattering processes where the scattered lepton is detected together with the Λ^0 hyperon. This requirement results in a higher Q^2 range being probed as compared to the current work where the scattered beam lepton is not detected and $\langle Q^2 \rangle \approx 0.0$ GeV^2.

The current is work based on data collected in the year 2004, during which the newly installed silicon tracking detector, the Lambda Wheels, was fully operational for the first time. The LW data point (leftmost solid circle in figure 7.1) has relatively large error bars as the ζ-cut removes the bulk of the low x_F data probed by this instrument. Otherwise, the three new low-Q^2 measurements are in agreement with the previously published HERMES results based on data collected during the years 1996-1997 and 1999-2000. Furthermore, the results of the current work are also in agreement with the measurements by the NOMAD experiment and the much less accurate E665 data. Within the present level of experimental precision the differences in the Q^2 range probed by the experiments does not seem to matter. The average of the three new data points is given by $D^{\Lambda}_{LL'} = 0.35 \pm 0.20$.

A general remark on all measurements of $D^{\Lambda}_{LL'}$ has to be made. It has been shown in [9] that in the HERMES experiment 46% of the Λ^0 hyperons originate from the decay of heavier hyperons of which the Σ^0 (38%), Σ^{*-} (3%),

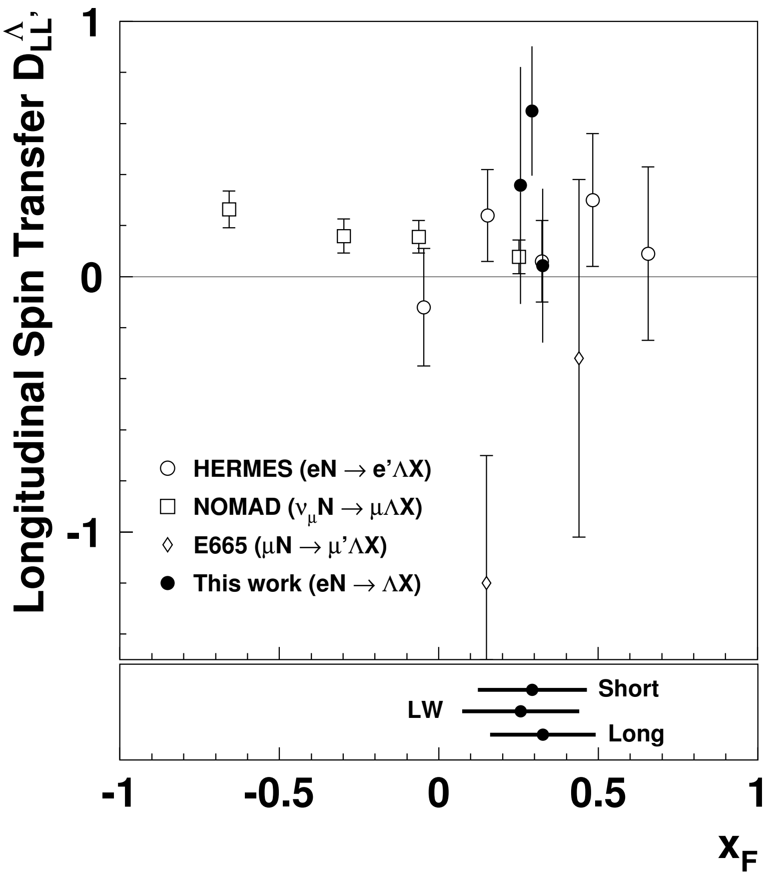

Figure 7.1: The longitudinal spin transfer $D^{\Lambda}_{LL'}$ measured by the HERMES [5]($\langle Q^2 \rangle = 2.4$ GeV^2), NOMAD [6]($\langle Q^2 \rangle = 5$ GeV^2) and E665 [7]($\langle Q^2 \rangle = 1.3$ GeV^2) experiments. The solid points represent the results of the current work ($\langle Q^2 \rangle \approx 0.0$ GeV^2). In the bottom panel the x_F ranges are shown over which the data have been integrated. The solid points and horizontal bars represent the mean and RMS value of the x_F distribution, respectively.

Σ^{*+} (2%) and Ξ^- (2%) are the most important ones. The Λ^0 particles originating from the $\Sigma^0 \to \Lambda^0\gamma$ decay obtain a polarization from the polarization of their parent as in the relation $P_\Lambda = -\frac{1}{3}P_{\Sigma^0}$ [22]. Other heavy hyperons can transfer their polarization to the Λ^0 in a different way causing an overall change of the polarization of the directly produced Λ^0 hyperons. As long as the induced polarization of the heavier hyperons has not been measured, it is not possible to correct for this effect unambiguously. Previous $D^{\Lambda}_{LL'}$ data shown in figure 7.1 also suffer from this effect and were not corrected for this effect either. In the past it has often been assumed that the sign of P_H for the various hyperons H would vary, which would lead to a cancellation of the effect on P_Λ. However, the new results of [9] show that the Σ^0

hyperon is by far the most important contribution, making it unlikely that such a cancellation occurs. In fact, to enable a realistic correction for the polarization contribution of heavier hyperons one should at least measure P_{Σ^0}. Such measurements do not exist today.

An accurate determination of the contribution of the u-quark to the total spin of the Λ^0 hyperon is not feasible at present in view of the arguments given above, although the measurements indicate that this contribution is likely to be small. This is also in agreement with the model calculations by Ma et al. [67] in the kinematic region covered by the present measurements. Further measurements of the longitudinal Λ^0 polarization are needed to provide a definite answer. These new measurements should occur in an experiment where a clear separation between the two types of fragmentation processes is possible. In this way the contributions from the Λ^0 hyperons produced in the target fragmentation region could be separated from those produced in the current fragmentation region. Future measurements should also include the reconstruction of the heavy hyperons and in particular the Σ^0 from which the Λ^0 hyperon could originate. By measuring the polarization of these heavier hyperons as well, a precise value of $D^{\Lambda}_{LL'}$ can be obtained.

7.2 The Spin Correlation Coefficient C_{sq}

Similar to the method described in section 7.1 the spin correlation coefficient C_{sq} can be calculated from the longitudinal Λ^0 polarization data by selecting events originating from the target fragmentation region. Moreover, if the polarization of the beam and the depolarization factor $D(y)$ are known, the following relation (as given by equation 2.23) can be used to evaluate C_{sq}:

$$C_{sq} = -\frac{P_\Lambda}{P_B D(y)}. \tag{7.3}$$

It is noted that the dilution factor due to the contribution of Λ^0 particles originating from the decay of heavier hyperons is not taken into account in the present results (nor in equation 7.3) for the reasons given in section 7.1 above. The requirement $\zeta < 0.17$ is imposed on the data to reduce the contribution of Λ^0 hyperons produced in the current fragmentation region. Again the same remarks regarding the non-ideal separation of the current and target fragmentation regions hold.

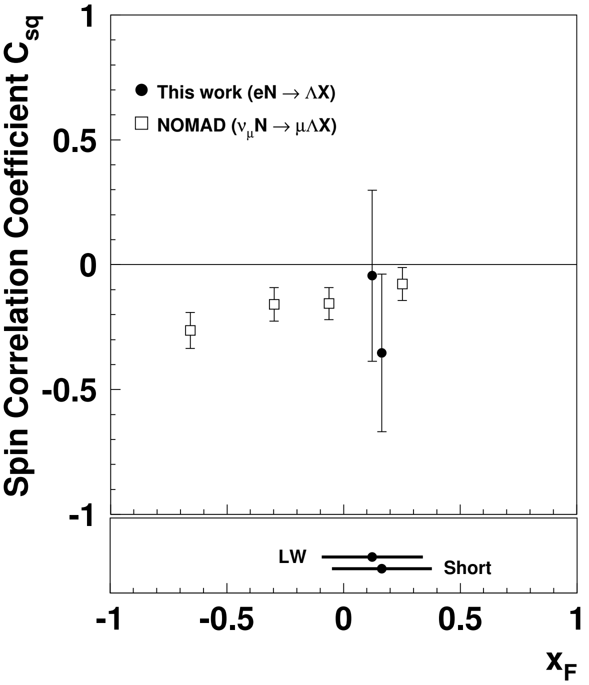

Figure 7.2: The spin correlation coefficient C_{sq} measured by the NOMAD [6] experiment and the present work. The bottom panel represents the RMS of the x_F distribution over which the data have been integrated.

The results for C_{sq} of the present work are shown in figure 7.2 together with the results obtained by the NOMAD experiment [6]. It is noted that the $\zeta < 0.17$ cut resulted in hardly any long track data. As a consequence the C_{sq} value derived from the long track data had error bars in excess of 100 % and are therefore not shown in figure 7.2. The bottom panel of figure 7.2 represents the mean and RMS values of the x_F distributions over which the data have been integrated. One can see that the results of the current work are in good agreement with the results obtained by the NOMAD experiment. These two different types of measurements (which have also been obtained at rather different average Q^2 values) seem to indicate a relatively small and negative value of the spin correlation coefficient C_{sq}. The average of the two present data points is found to be $C_{sq} = -0.20 \pm 0.23$.

Under the assumption that the dilution effect of heavier hyperons and current fragmentation contributions are small the result favors theoretical models which predict $C_{su} \approx 0$ (over those that lead to very large C_{su} values). One model leading to small C_{su} values is based on the assumption that gluons are a dominant carrier of the nucleon spin [4], as was discussed in section 2.2.1. More generally, one can conclude that the correlation between the spin of the scattered u-quark and the s-quark in the target nucleon is small suggesting that the s-quarks are not strongly polarized in the nucleon. This is also in qualitative agreement with the inclusive and semi-inclusive DIS measurements performed at HERMES where $\Delta s + \Delta \bar{s} = -0.085 \pm 0.013(\text{theo.}) \pm 0.008(\text{exp.}) \pm 0.009(\text{evol.})$ was derived from measurements of the spin structure function g_1 [2], and $\Delta s = 0.028 \pm 0.033(\text{stat.}) \pm 0.009(\text{syst})$ was obtained from studies of the flavor separated quark helicity distributions [3]. Improvements of the present results can be obtained by increasing the statistics, extending the data to lower values of x_F (which requires the lepton to be detected) and applying the same improvements mentioned above in section 7.1 in relation to future $D^{\Lambda}_{LL'}$ measurements.

7.3 Transverse target Λ^0 polarization

Measurements of the Λ^0 polarization in the direction of the transverse target magnetic field described in section 6.2 make it possible to study transversity effects. The relation between the measured Λ^0 polarization P_Λ, the measured target polarization P_N and various other quantities of interest can be shown by rewriting equation 2.29:

$$\frac{P_\Lambda}{P_N D(y)} = \frac{h_{1,u}(x,Q^2)}{f_{1,u}(x,Q^2)} \cdot \frac{H^{\Lambda}_{1,u}(z,Q^2)}{D^{\Lambda}_{1,u}(z,Q^2)} \tag{7.4}$$

$$= \mathrm{DF} \cdot \mathrm{FF}, \tag{7.5}$$

where the short hand notation DF denotes the ratio between the transversity distribution h_1 and the quark number density f_1, and FF denotes the ratio of the fragmentation functions H^{Λ}_1 and D^{Λ}_1 describing the fragmentation of a transversely polarized (unpolarized) quark to a transversely polarized (unpolarized) Λ^0, respectively. Relation 7.5 applies to Λ^0 hyperons produced in the current fragmentation region which leads to the requirement $\zeta > 0.17$ as described in section 7.1. The data are analyzed in such a way to extract $\mathrm{DF} \cdot \mathrm{FF}$ from the polarization data.

The result of the transversity analysis is presented in figure 7.3 where in the bottom panel the mean and RMS values of the x_F distributions over which has been integrated integrated are shown. As was argued before in section 7.1 the LW data have a large error bar once the requirement $\zeta > 0.17$ is applied.

As can be seen in figure 7.3 the three measurements are consistent with each other and result in an average value of $\mathrm{DF} \cdot \mathrm{FF} = -0.07 \pm 0.13$. Under the same assumptions regarding the fragmentation process and heavy hyperon contamination as were discussed previously, the data set suggests

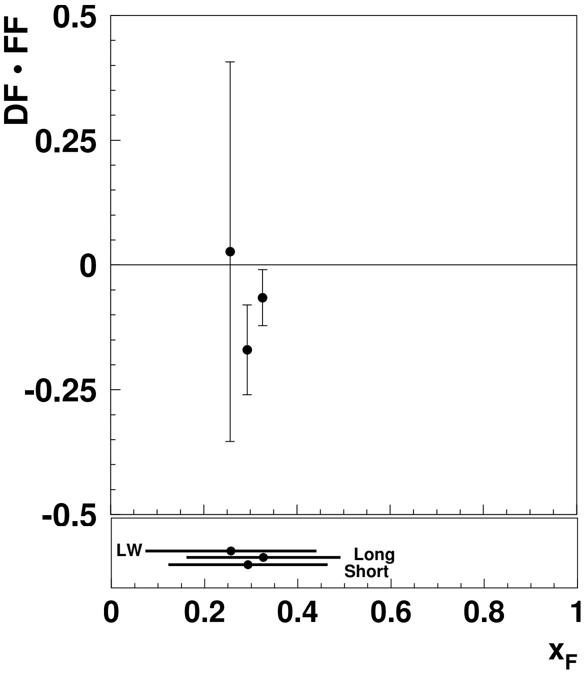

Figure 7.3: The product of the ratios of distribution and fragmentation functions, DF · FF, defined in equation 7.5 as a function of x_F. The bottom panel shows the mean and RMS values of the corresponding x_F distribution over which the data have been integrated.

a somewhat small and negative value of the measured product. This result, although still quite inaccurate, suggest a small value for the transversity function which is also found in the other two transversity measurements performed at HERMES. In these measurements, which were based on single-spin asymmetries (SSAs) for semi-inclusive π^+, π^- and π^0 production [12] and SSAs for pion pair production [13] small asymmetries at the 5 % level were found. As these asymmetries also correspond to a product of h_1 and some unknown fragmentation function, the results are qualitatively in agreement. The fragmentation functions $H_{1,u}^{\Lambda}$ in the measured product is unknown and also contributes to the small negative value of the product DF · FF. In fact, as was discussed in [12] the negative sign of DF · FF is most likely due to the fragmentation function.

Only recently the first preliminary results from the COMPASS experiment on this subject came available [14, 68]. The COMPASS results include Λ^0 polarization values in the direction of the transversely polarized target as a function of the Bjorken scaling variable x. It should be noted however that these data were not corrected for the polarization of the transverse target $P_N \sim 50$ % nor the target dilution factor of $f \sim 0.4$. As both factors are substantially smaller as compared to the present experiment ($P_N \sim 81$ % and $f \sim 1$), the statistics of the results shown in [14, 68] cannot be directly compared to the present data. The COMPASS data set shows a Λ^0 polarization which is consistent with zero for x values below 0.1. Above this value there is an indication for a small negative Λ^0 polarization.

The result presented in the current work is the first measurement of the transversity distribution using Λ^0 hyperons in the HERMES experiment. In order to disentangle the fragmentation and distribution functions more statistics are needed with an accurate determination of different kinematic variables and -most importantly- an independent determination of $H_{1,u}^{\Lambda}$ in e^+e^- experiments is called for. In the case of the single spin asymmetries of [12] such independent data have recently come available.

Chapter 8

Summary and Outlook

The work described in this thesis is based on measurements performed in the year 2004 with the use of the HERMES spectrometer and the addition of a new silicon tracking detector named the Lambda Wheels.

With this experimental setup it has been tried to address the following three questions:

- What is the role of the s-quark in the spin structure of the nucleon?
- Is the spin of the Λ^0 hyperon entirely due to that of the strange quark, or is the Λ^0 spin structure more complicated like that of the nucleon?
- What is the quark transversity distribution in the nucleon?

Measurement of the polarization of Λ^0 hyperons can contribute to finding answers to each one of the questions mentioned above. This has been explained by sketching the theoretical framework of Λ^0 polarization in Deep Inelastic Scattering and discussing the presently available measurements.

The experimental setup used for the measurements on which this thesis is based has been described in detail with a separate description and discussion of the newly installed Lambda Wheels. This new tracking detector expands the acceptance of the HERMES spectrometer and also extends the covered kinematic region. The performance of the LW during the 2004 data taking period has been discussed and the efficiency was found to be 79.2 ± 3.4 %.

It has been demonstrated that it is possible to reconstruct Λ^0 hyperons using tracks reconstructed with the LW. The resolution was found to be a factor 4 worse compared to that found with the standard reconstruction using spectrometer tracks. This is consistent with the expectations for a reconstruction method where there is no momentum measurement for those tracks which are reconstructed in the LW only.

The background has been modelled with a data set based on the mixed event method which enabled the correction of the measured data for background contributions. These results were compared with PYTHIA Monte Carlo simulations, in which Λ^0 hyperons were simulated. A good agreement was observed between the average values of the measured and simulated kinematic variables. At the same time an overestimate of the MC yield for particles with lower momenta was found. This leads to an overestimate of the Λ^0 yield in the MC which reaches a factor 4 for quasi-real photoproduction of Λ^0 hyperons reconstructed with the LW.

Data taken with a transversely polarized target have also been analyzed. A correction method has been developed for spectrometer tracks to compensate for the bend induced by the target magnetic field. With the correction applied resolutions comparable to those found in the unpolarized data were obtained. The correction cannot be applied to LW tracks because of the absence of a momentum measurement. The angular resolutions of spectrometer and LW tracks are not sufficient to apply the correction method in an alternative way. However, for tracks originating from a Λ^0 decay in those regions where the field is low or absent, it is still possible to use the LW.

With the reconstructed Λ^0 events the Λ^0 polarization has been measured in quasi-real photoproduction, i.e. at $Q^2 \approx 0$ GeV^2. Three different methods to obtain the longitudinal Λ^0 polarization were investigated and found to be consistent. With the use of the mixed event data set a correction of the measured polarization for the contribution of the background was performed. The size of the resulting longitudinal Λ^0 polarization is relatively small and similar values were obtained from the measurements with the spectrometer. The PYTHIA MC was used to evaluate the mean value of the x_F distributions probed by the photoproduction data. Also, the polarization of the Λ^0 hyperon in the direction of the spin of the transversely polarized target was measured, and also in this case small polarization values were found.

The measurement of the longitudinal Λ^0 polarization has enabled the determination of the longitudinal spin transfer $D^{\Lambda}_{LL'}$ which is a probe of the contribution of the u-quark to the spin of the Λ^0 hyperon. The average value of all data analyzed resulted in $D^{\Lambda}_{LL'} = 0.35 \pm 0.20$ at $Q^2 \approx 0$ GeV^2. This result is in agreement with the previously published HERMES result [5] and with the measurements of the NOMAD [6] and E665 [7] experiments. The latter three experiments [5, 6, 7] were carried out at squared four-momentum transfer values of a few GeV^2, which is substantially above the value probed by the present experiment. As the resulting $D^{\Lambda}_{LL'}$ values are consistent, the Q^2 value of the measurements does not seem to matter. In none of the experiments a clear separation between current and target fragmentation regions can be realized. Also all $D^{\Lambda}_{LL'}$ measurements have an unknown contribution of the polarization transfer from heavier hyperons to Λ^0 hyperons produced in their decays. These uncertainties prevent an accurate determination of the u-quark contribution to the spin of the Λ^0, although the present results seem to suggest that this contribution is likely to be small.

The spin correlation coefficient C_{sq} can be evaluated from the measured longitudinal Λ^0 polarization for data corresponding to the target fragmentation region. This coefficient represents the correlation between the spin of the struck quark in the target nucleon and that of the s-quark in the nucleon. An average value of $C_{sq} = -0.20 \pm 0.23$ is found in the analyzed data set which is in agreement with the measurements of the NOMAD [6] experiment. These results indicate that there is a small and possibly even negligible correlation between the spin of the struck u-quark and that of the s-quark in the target nucleon, but is also in agreement with models in which the gluon is an important carrier of nucleon spin.

With the measurements of the Λ^0 polarization in the direction of the transversely polarized target transversity effects were studied. The product of two ratios was studied namely DF which is the ratio of the transversity distribution h_1 and the quark number density f_1 and the ratio denoted by FF of the fragmentation functions H_1^Λ and D_1^Λ describing the fragmentation of a transversely polarized (unpolarized) quark to a transversely polarized (unpolarized) Λ^0, respectively. The resulting average value was found to be $\mathrm{DF} \cdot \mathrm{FF} = -0.07 \pm 0.13$. This result suggests a small value for the transversity function which is in qualitative agreement with other measurements performed at HERMES [12, 13].

The results obtained in this thesis have proven that the operation of a full silicon tracking detector array inside the vacuum of the beam is possible, and that the reconstruction of Λ^0 hyperons with the use of this detector can be used to measure the polarization of Λ^0 particles. Such measurements contribute to finding answers of several remaining fundamental questions in the field of hadron spin physics. Furthermore, the results presented in this thesis confirm previous results with a new independent method.

Based on these first results it is possible to outline the requirements for new experiments. In order to increase the precision of the first results presented in this thesis an increase of the Λ^0 hyperon yield is necessary. This could be achieved in high luminosity experiments with proper tracking and PID detectors as those described in [69]. In such experiments it is important to also reconstruct the heavy hyperons from which a substantial fraction of the Λ^0 hyperons is originating [9]. Also an accurate determination of the kinematic variables and specifically a separation between Λ^0 hyperons originating from target fragmentation and those formed in the current fragmentation region is of importance. This can be realized by carrying out such experiments at substantially higher beam energies. These new experiments could be performed for instance, at the neutrino factory proposed in [23] where the physics potential of accurate measurements of the kind explored in this thesis are underlined.

Samenvatting en vooruitblik

Het beschreven werk in dit proefschrift is gebaseerd op metingen verricht in het jaar 2004 met behulp van de HERMES spectrometer en de daar aan toegevoegde Lambda Wielen (LW), een nieuwe silicium tracking detector.

Met deze experimentele opstelling is getracht een antwoord te vinden op de volgende vragen:

- Wat is de invloed van het s-quark op de spinstructuur van het nucleon?
- Wordt de spin van het Λ^0-hyperon volledig gedragen door de spin van het s-quark of is de spinstructuur van het Λ^0-hyperon complexer zoals in het geval van het nucleon?
- Wat is de transversity verdeling van quarks in het nucleon?

De meting van de polarisatie van Λ^0-hyperonen kan bijdragen tot het vinden van antwoorden op elk van de bovengestelde vragen. Dit is uitgelegd in de beschrijving van het theoretisch kader van de polarisatie van Λ^0-hyperonen in diep-inelastische verstrooiing (DIS) en het behandelen van de op dit ogenblik beschikbare metingen.

De gebruikte experimentele opstelling voor de metingen waar dit proefschrift op gebaseerd is, is in detail beschreven met een aparte, uitgebreide beschrijving en bespreking van de recentelijk geïnstalleerde LW. Deze nieuwe tracking detector verruimt de acceptatie van de HERMES spectrometer en breidt het gemeten kinematisch gebied uit. De manier waarop gedurende de meetperiode in 2004 meetgegevens zijn verzameld met de LW is beschreven. In die periode functioneerden de LW met een efficiëntie van 79.2 ± 3.4 %.

Het is aangetoond dat het mogelijk is om Λ^0-hyperonen te detecteren via de sporen die met behulp van de LW gereconstrueerd konden worden. Het is vastgesteld dat de massaresolutie een factor 4 slechter is dan de standaardreconstructie gebaseerd op de gemeten spectrometersporen. Dit is consistent met de verwachtingen voor een reconstructiemethode zonder momentummeting van de sporen die enkel in de LW gereconstrueerd worden.

De achtergrond is gemodelleerd met een dataset gebaseerd op een “mixed event methode" die ons instaat stelt de gemeten gegevens te corrigeren voor de achtergrond. De resultaten zijn vergeleken met PYTHIA Monte Carlo-simulaties waarmee Λ^0-hyperonen werden gesimuleerd. Een goede overeenkomst werd vastgesteld tussen de gemiddelde waarden van de gemeten en gesimuleerde kinematische variabelen. Ook werd een overschatting van de MC-opbrengst voor deeltjes met een laag momentum vastgesteld. Dit leidt tot een overschatting van de Λ^0-opbrengst in de MC die een factor 4 bereikt ten opzichte van Λ^0-hyperonen die met de LW gereconstrueerd worden.

De metingen met een transversaal gepolariseerd target zijn ook geanalyseerd. Er is een correctiemethode ontwikkeld voor sporen in de spectrometer die compenseert voor de afbuiging in het magnetisch veld. Met deze correctiemethode zijn resoluties bereikt die vergelijkbaar zijn met de resoluties verkregen in de ongepolariseerde metingen. De correctie kan echter niet toegepast worden op de sporen gemeten met de LW door de afwezigheid van een meting van het momentum. De hoekresoluties van de sporen in de spectrometer en de LW zijn onvoldoende om de correctiemethode toe te passen op een alternatieve manier. Het is echter wel mogelijk om de sporen in de LW te gebruiken voor deeltjes die afkomstig zijn van een verval van het Λ^0-hyperon in die gebieden waar het magneetveld laag genoeg of afwezig is.

Met de gereconstrueerde Λ^0-hyperonen is de polarisatie van het Λ^0-deeltje gemeten in quasi-reële fotoproductie waar $Q^2 \approx 0$ GeV^2. Drie verschillende methodes om de longitudinale Λ^0-polarisatie te bepalen zijn besproken waarbij vastgesteld is dat de verschillende resultaten consistent zijn. Met behulp van de mixed event dataset is een correctie van de gemeten polarisatie voor de bijdrage van de achtergrond toegepast. De grootte van de gevonden longitudinale Λ^0-polarisatie is relatief klein en vergelijkbaar met waarden die met behulp van de spectrometer zijn verkregen. De PYTHIA MC is gebruikt om de gemiddelde waarde van de x_F-verdelingen te bepalen en die te vergelijken met de resultaten verkregen in andere fotoproductie metingen. Bovendien is de polarisatie van het Λ^0-hyperon gemeten in de richting van de spin van het transversaal gepolariseerde target. Ook met deze metingen zijn kleine waarden voor de polarisatie vastgesteld.

De meting van de longitudinale Λ^0-polarisatie maakt een bepaling mogelijk van de longitudinale spinoverdracht $D^{\Lambda}_{LL'}$ die een maat is voor de bijdrage van de spin van het u-quark aan de totale spin van het Λ^0-hyperon. De gemiddelde waarde van alle geanalyseerde metingen leidt tot $D^{\Lambda}_{LL'} = 0.35 \pm 0.20$ bij $Q^2 \approx 0$ GeV^2. Dit resultaat is in overeenstemming met het eerder gepubliceerde HERMES-resultaat voor deze grootheid [5] en met de metingen van de NOMAD [6] en E665 [7] experimenten. De drie laatstgenoemde experimenten [5, 6, 7] werden uitgevoerd bij Q^2 waarden van enkele GeV^2, die substantieel boven de waarde liggen die hoort bij de metingen die in dit proefschrift worden beschreven. Vermits de resulterende $D_{LL'}^{\Lambda}$-waarden consistent zijn, blijkt de waarde van Q^2 van de metingen niet van belang te zijn. In geen enkele van de besproken metingen is een duidelijke scheiding tussen current- en target-fragmentatiegebieden mogelijk. Bovendien hebben alle $D_{LL'}^{\Lambda}$-metingen een onbekende bijdrage van het verval van zwaardere hyperonen naar Λ^0-hyperonen. Deze onbekende bijdrage verhindert een nauwkeurige bepaling van de u-quark-bijdrage aan de spin van het Λ^0. Niettemin suggereren de huidige resultaten dat deze bijdrage waarschijnlijk klein is.

De spin correlatiecoëfficiënt C_{sq} kan berekend worden uit de gemeten longitudinale Λ^0-polarisatie voor metingen in het target fragmentatiegebied. Deze coëfficiënt beschrijft de correlatie tussen de spin van het getroffen quark en die van het s-quark in het target nucleon. Een gemiddelde waarde van $C_{sq} = -0.20 \pm 0.23$ werd bepaald aan de hand van de geanalyseerde metingen. Dit resultaat is in overeenstemming met de metingen van het NOMAD [6] experiment. Deze resultaten wijzen op een kleine en mogelijk verwaarloosbare correlatie tussen de spin van het getroffen u-quark en die van het s-quark in het nucleon van het target, maar is ook in overeenstemming met modellen waarbij het gluon een belangrijke drager is van de spin in het nucleon.

Met de metingen van de Λ^0-polarisatie in de richting van het transversaal gepolariseerd target zijn transversity-effecten bestudeerd. Het product van twee verhoudingen is bepaald, namelijk DF, die de verhouding weergeeft van de transversity verdeling h_1 en de quark verdeling f_1, en de verhouding aangeduid met FF van respectievelijk de fragmentatiefuncties H_1^{Λ} en D_1^{Λ}, die de fragmentatie beschrijft van een transversaal gepolariseerd (ongepolariseerd) quark naar een transversaal gepolariseerd (ongepolariseerd) Λ^0. De resulterende gemiddelde waarde is $\mathrm{DF} \cdot \mathrm{FF} = -0.07 \pm 0.13$. Dit resultaat suggereert een kleine waarde voor de transversity-functie hetgeen in kwalitatieve overeenstemming is met andere metingen in het HERMES-experiment [12, 13].

De verkregen resultaten die beschreven staan in dit proefschrift hebben bewezen dat het mogelijk is om een volledige silicium trackingdetector in het vacuüm van de bundel in bedrijf te houden en daarmee Λ^0-hyperonen te reconstrueren en hun polarisatie te bepalen. Zulke metingen dragen bij tot het vinden van antwoorden op verschillende fundamentele vragen in het veld van de hadron spinfysica. Bovendien bevestigen de resultaten gepresenteerd in dit proefschrift voorafgaande resultaten met het gebruik van een nieuwe onafhankelijke methode.

Met behulp van deze eerste resultaten is het mogelijk om de vereisten voor nieuwe experimenten te schetsen. Een grotere nauwkeurigheid van de eerste resultaten gepresenteerd in dit proefschrift is mogelijk door een verhoging van het aantal gereconstrueerde Λ^0-hyperonen. Dit kan men verkrijgen in experimenten die uitgevoerd worden met een hogere luminositeit en een geschikte reconstructie en identificatie van de gedetecteerde deeltjes zoals beschreven in [69]. In zulke experimenten is het van belang om ook de zwaardere hyperonen te reconstrueren vermits een substantiële fractie van de Λ^0-hyperonen hiervan afkomstig is [9]. Bovendien is een nauwkeurige bepaling van de kinematische variabelen van belang, alsook de scheiding tussen het current- en target-fragmentatiegebied. Dit kan gerealiseerd worden in experimenten met een wezenlijk hogere bundelenergie. Deze nieuwe experimenten kunnen bijvoorbeeld plaatsvinden in de neutrinofabrieken als voorgesteld in [23], waar het fysicapotentieel van nauwkeurige metingen als deze onderzocht in dit proefschrift benadrukt worden.

Appendix A

Target Magnetic Field Correction

This appendix describes in detail the determination of the optimal values for the two parameters, zfield and Bfield, which are crucial in the correction method, described in section 5.2.2, for those tracks which are bent in the transverse target magnetic field. First the effectiveness of the correction method is studied with the use of a Monte Carlo simulation in which the optimal values for the two parameters Bfield and zfield are determined. With the use of the Monte Carlo simulation also the improvement in resolution of the Λ^0 invariant mass resulting from the correction method is studied. In the second section the optimized correction method is applied to data.

A.1 Monte Carlo simulation

To study the effectiveness of the correction method a Geant Monte Carlo (MC) simulation is used to track the decay particles of the Λ^0 in a geometry representing both the target and front tracking regions. The TM is modeled in a realistic way by using the measured field map in these MC calculations. With this MC the decay vertex, and the track parameters and momenta in this vertex are generated. As a result momenta and track parameters are obtained as they would be measured in the field free region by the front tracking. This enables a comparison between the generated values in the MC and the reconstructed values from the correction method applied to the simulated momenta and track parameters in the field free region.

A.1.1 Fixing the field parameters

Because the invariant mass of the Λ^0 particles used in the MC is kept equal to the PDG value, the optimal values for Bfield and zfield are those for which the reconstructed invariant mass is closest to this book value. However this criterion cannot be used in an analysis of real data because this could bias the result. Therefore the MC data set is split in the two topologies A and B described previously in figure 5.15. The optimal values for Bfield and zfield are those for which the RMS of the invariant mass spectra of these two topologies is minimal. Furthermore, the systematic shift in invariant mass which is opposite in the two topologies is minimized by choosing optimal values for Bfield and zfield.

When the RMS of the invariant mass spectra is calculated for various values of Bfield and zfield the figures displayed in figure A.1 are obtained. On the left events of the topology A type are used, on the right the events have topology B.

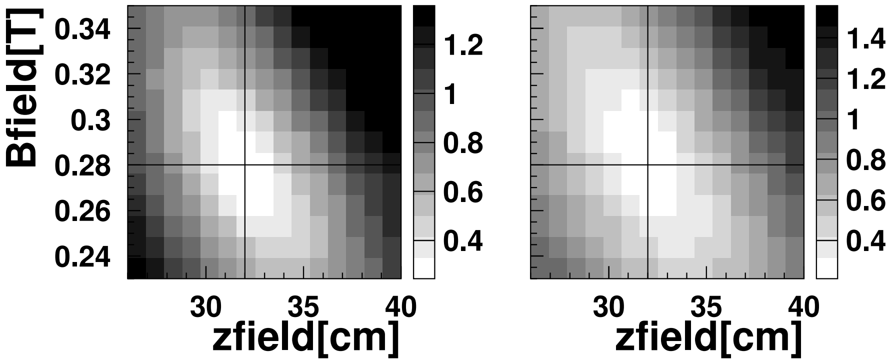

Figure A.1: The RMS width [MeV] of the Λ^0 peak in the invariant mass spectra for various values of the parameters Bfield and zfield. On the left events with topology A are used, on the right the result for topology B is given.

From these plots one can determine the value of Bfield and zfield for which the RMS of the invariant mass is minimal. This value of Bfield and zfield is the same in the two topologies, namely 0.28 T and 32.0 cm respectively, as indicated by the horizontal and vertical lines in figure A.1. One can also see that the approach towards the minimum RMS value is steeper for topology A as compared to topology B. This is due to the fact that the tracks are bent towards each other in topology A (see figure 5.15). Therefore, the angle between the tracks is larger and the calculation of the decay vertex more accurate which results in a better determination of the angle between the bent tracks and a better defined invariant mass.

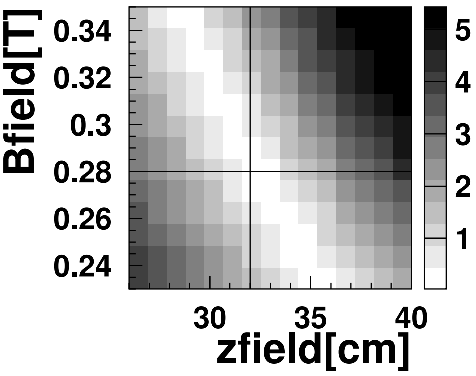

Figure A.2: The absolute difference in the mean value [MeV] of the invariant mass peak as obtained with the two topologies for various values of Bfield and zfield.

By calculating the absolute difference of the mean value of the Λ^0 peak in the invariant mass in the two topologies for various values of Bfield and zfield figure A.2 is obtained. The optimal values for Bfield and zfield found from the RMS of the invariant mass spectrum lie inside the valley of minima indicated by the white diagonal band in figure A.2. This means that the shift in invariant mass due to the TM in the two topologies can be minimized to less than 1 MeV, but as such is not very sensitive to the absolute value of Bfield or zfield.

A.1.2 Resolution improvement

With the optimal values of the Bfield and zfield parameters now available the improvement in mass resolution with the constant box field approximation can be studied. The effect on the invariant mass resolution of the correction method is best illustrated with the plots shown in figure A.3. Here, the difference between the calculated invariant mass and the PDG value of the Λ^0 is plotted as a function of the z value of the decay vertex (in cm). On the left in figure A.3, the result is plotted when using the straight tracks without correction. On the right, the same data are used after applying the correction method. The values 0.28 T for Bfield and 32.0 cm for zfield are used.

From the left hand plot in figure A.3 it is seen that straight tracks only give a proper resolution of a few MeV towards the edge of the field at about 31 cm from the center of the target. This would result in an increased resolution in invariant mass of about 2 MeV. In the right hand plot the improvement is clearly seen. The width in invariant mass is smaller than 1 MeV for vertices below 30 cm from the center of the target. The shape of the distribution is

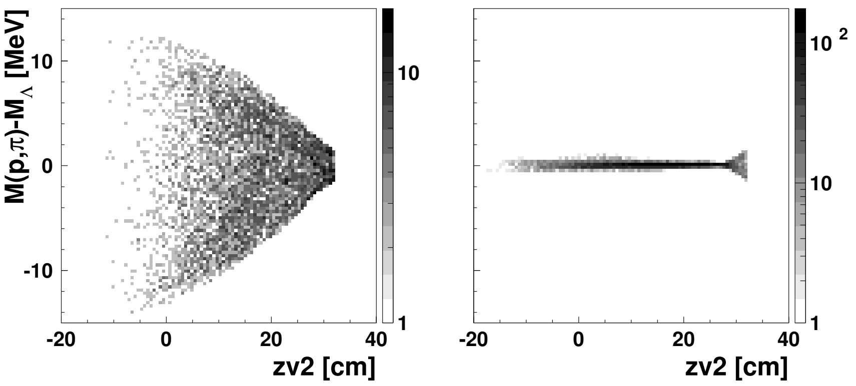

Figure A.3: The calculated invariant mass minus the PDG value of the Λ^0 as a function of the decay vertex $zv2$. For straight tracks without correction on the left, with the correction method applied on the right.

due to the constant field over the entire z-range. At z-values close to 28 cm where the calculated invariant mass becomes equal to the PDG value of the Λ^0 the integrated magnetic field seen by the charged particles traversing the field is equal to the constant field. Closer to the edge the constant field overestimates the target field which drops at higher values of z. Since the overall resolution of about 1 MeV is smaller than the resolution in the unpolarized case which is around 2 MeV we can conclude that the constant box field approximation serves its purpose well.

A.1.3 Scan the valley of minima

With the distributions in figure A.3 in mind it is possible to make a scan inside the valley shown in figure A.2. This is an alternative way of finding the optimal values of Bfield and zfield which is used in the data analysis discussed in the following section.

In order to scan the valley of minima in figure A.2 a clear separation between the two topologies has to be made. Therefore only events with a decay vertex below z values of 26 cm are used. Below this z value the resulting invariant mass is always larger or always smaller than the book value for topology A or B, respectively.

The scan through the valley in figure A.2 is carried out by taking constant values for zfield and determining for each value of zfield the value for Bfield where the difference in invariant mass between the two topologies is minimal. These results are plotted in figure A.4. From a parabola fit of these data a minimum of 31.96 ± 0.49 cm is found which agrees with the 32 cm found with the RMS of the invariant mass for the two topologies separate. This

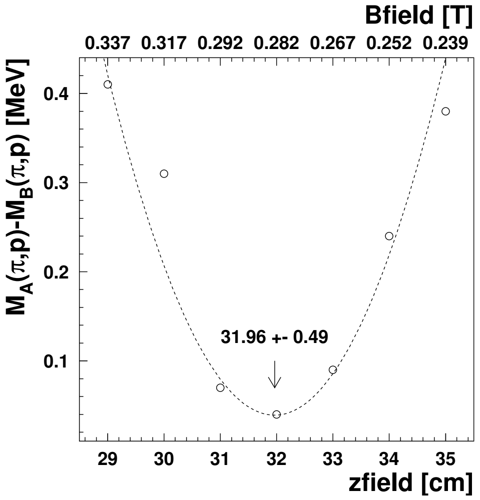

Figure A.4: The difference in invariant mass between the two topologies versus zfield values. Those values for Bfield are taken for which the absolute difference in invariant mass between the two topologies is minimal. The dashed curve is a parabola fit with its minimum indicated.

proves the consistency between the two methods for obtaining the correct values for Bfield and zfield.

With the correction method based on the approximation of the target magnetic field by a constant box field it was shown that the invariant mass of the Λ^0 can be reconstructed with a precision of better than 1 MeV. The values for the parameters (Bfield and zfield) of this constant box field were found with two different methods. The application of this analysis on the data is discussed in the next section.

A.2 Results obtained with the spectrometer data

In this section the data taken with the polarized target are analyzed using the tracks detected in the spectrometer. The methods developed with help of the MC to determine the optimal values for the Bfield and zfield parameters are applied to the data.

The data are split in the two topologies A and B in which the horizontal slope of the pion track is respectively larger and smaller than that of the proton track as sketched in figure 5.15. As with the MC the RMS and mean value of the invariant mass in the two topologies is used to find the optimal value for Bfield and zfield. However, in the data analysis there is always a contamination of background events in the invariant mass spectrum.

Therefore the Λ^0 peak is fitted with a Gaussian and a polynomial is added to describe the background. This Gaussian fit is then used to extract the values for the RMS and mean of the Λ^0 peak.

In figure A.5 the RMS is plotted for the two topologies A and B as obtained with the various values for Bfield and zfield used in the correction method.

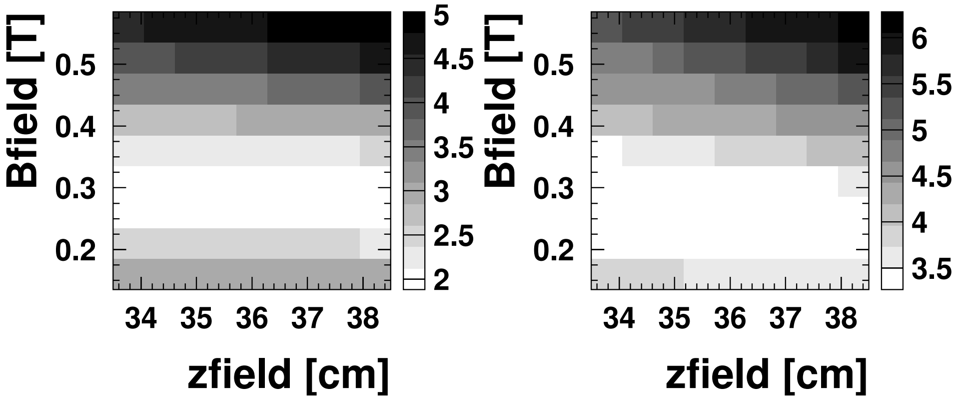

Figure A.5: The RMS [MeV] of a Gaussian fit of the Λ^0 invariant mass peak for various values of Bfield and zfield, on the left for events of the topology A type, on the right topology B.

Because the RMS of the invariant mass distributions is larger and more spread out the optimal values for Bfield and zfield cannot be determined directly from these plots. However, when we plot the absolute difference of the mean of the invariant mass for the two topologies figure A.6 is obtained. In this case there is a clear valley of minima.

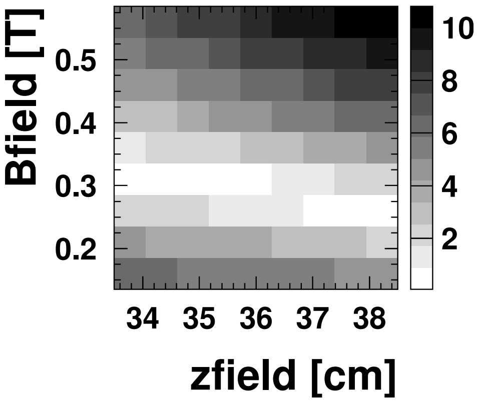

Figure A.6: The absolute difference of the mean [MeV] of a Gaussian fit of the invariant mass peak obtained with the two topologies for various values of Bfield and zfield.

When this valley of minima is scanned the data shown in figure A.7 are

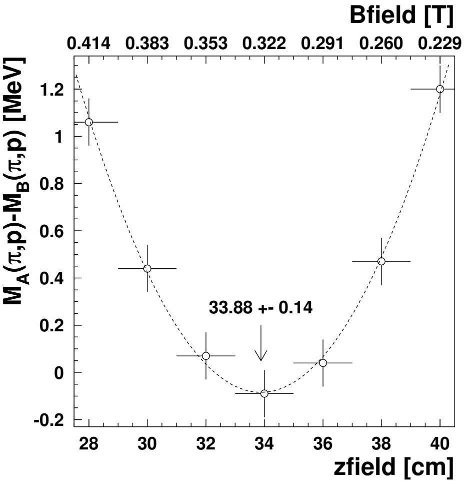

Figure A.7: The difference in invariant mass between the two topologies versus zfield found using spectrometer tracks. For each zfield value the corresponding Bfield value is determined for which the absolute difference in invariant mass between the two topologies is minimal.

obtained where a parabola fit is used with a minimum of 33.88 ± 0.14 cm as indicated with the arrow. These points are obtained by keeping the values for zfield constant and determining the value for Bfield for which the absolute difference between the two topologies minimal. In figure A.7 a clear minimum can be seen. From this figure the optimal values for Bfield and zfield in the data are found to be 0.32 T and 34.0 cm respectively.

Bibliography

[1] EMC, J. Ashman *et al.*, *A measurement of the spin asymmetry and determination of the structure function g1 in deep inelastic muon-proton scattering*, Phys. Lett. **B206**, 364 (1988).

[2] Hermes, A. Airapetian *et al.*, *Precise determination of the spin structure function g_1 of the proton, deuteron and neutron*, Phys. Rev. **D74**, in press (2006), hep-ex/0609039.

[3] Hermes, A. Airapetian *et al.*, *Quark helicity distributions in the nucleon for up, down, and strange quarks from semi-inclusive deep-inelastic scattering*, Phys. Rev. **D71**, 012003 (2005), hep-ex/0407032.

[4] J. Ellis, D. Kharzeev, and A. Kotzinian, *The proton spin puzzle and Λ polarization in deep-inelastic scattering*, Z. Phys. **C69**, 467 (1996), hep-ph/9506280.

[5] Hermes, A. Airapetian *et al.*, *Longitudinal Spin Transfer to the Λ Hyperon in Semi-Inclusive Deep-Inelastic Scattering*, Phys. Rev. **D74**, 072004 (2006), hep-ex/0607004.

[6] Nomad Collaboration, P. Astier *et al.*, *Measurement of the Λ polarization in ν_μ charged current interactions in the NOMAD experiment*, Nucl. Phys. **B588**, 3 (2000).

[7] E665 Collaboration, M. Adams *et al.*, *Λ and $\bar{\Lambda}$ polarization from deep inelastic muon scattering*, Eur. Phys. J. **C17**, 263 (2000).

[8] R. Jaffe, *Polarized Λ's in the current fragmentation region*, Phys. Rev. **D54**, 6581 (1996).

[9] A. Reischl, *Quasi-real photoproduction of hyperons and their impact on the Λ polarization*, PhD thesis, Universiteit van Amsterdam (UvA), The Netherlands, April 2007.

[10] G. van der Steenhoven, *Future directions in studying QCD aspects of nuclear physics*, International Nuclear Physics Conference, Goteborg, Sweden, Jun 27 - Jul 2, 2004.

[11] M. Anselmino, *Transversity and Lambda polarization*, (2003), hep-ph/0302008.

[12] Hermes, A. Airapetian *et al.*, *Single-Spin Asymmetries in Semi-Inclusive Deep-Inelastic Scattering on a Transversely Polarized Hydrogen Target*, Phys. Rev. Lett. **94**, 012002 (2005), hep-ex/0408013.

[13] P. B. van der Nat, *First measurement of interference fragmentation on a transversely polarized hydrogen target*, 2005, hep-ex/0512019.

[14] Compass, F. Bradamante, *Transversity physics at COMPASS*, (2006), hep-ex/0602013.

[15] M. C. Vetterli, *The Spin Structure of the Nucleon (Lectures at the 13th Lake Louise Winter Institute)*, 1998, hep-ph/9812420.

[16] E. Berger, *Semi-Inclusive Inelastic Electron Scattering from Nuclei*, January 1987, Proceedings of the Workshop on Electronuclear Physics with Internal Targets, Stanford, CA.

[17] J. Soffer, *Is the riddle of the hyperon polarizations solved?*, 1999, hep-ph/9911373, Proceedings of Hyperon99, Physics Symposium, FNAL Batavia.

[18] J. Ellis, A. Kotzinian, and D. Naumov, *Intrinsic Polarized Strangeness and Λ^0 Polarization in Deep-Inelastic Production*, Eur. Phys. J **C25**, 603 (2002), hep-ph/0204206.

[19] D. Ashery and H. Lipkin, *Expected polarization of Λ particles produced in deep inelastic polarized lepton scattering*, Phys. Lett. **B469**, 263 (1999).

[20] M. Burkardt and R. L. Jaffe, *Polarized $q \to \Lambda$ Fragmentation Functions from $e^+e^- \to \Lambda + X^*$*, Phys. Rev. Lett. **70**, 2537 (1993), hep-ph/9302232.

[21] Hermes, A. Airapetian *et al.*, *Measurement of Longitudinal Spin Transfer to Λ Hyperons in Deep-Inelastic Lepton Scattering*, Phys. Rev. **D64**, 112005 (2001), hep-ex/9911017.

[22] R. Gatto, *Relations between the Hyperon Polarizations in Associated Production*, Phys. Rev. **109**, 610 (1958).

[23] M. Mangano *et al.*, *Physics at the front-end of a neutrino factory: a quantitative appraisal*, (2001), hep-ph/0105155.

[24] V. Barone and P. G. Ratcliffe, *Transversity. Proceedings, Workshop, Como, Italy, September 7-10, 2005*, Prepared for International Workshop on Transverse Polarization Phenomena in Hard Processes (Transversity 2005), Villa Olmo, Como, Italy, 7-10 Sep 2005.

[25] A. A. Sokolov and I. M. Ternov, *On polarization and spin effects in the theory of synchrotron radiation*, Sov. Phys. Dokladi **8**, 1203 (1964).

[26] D. Barber *et al.*, *The HERA polarimeter and the first observation of electron spin polarization at HERA*, Nucl. Instrum. Meth. **A329**, 79 (1993).

[27] D. Barber *et al.*, *The first achievement of longitudinal spin polarization in a high energy electron storage ring*, Phys. Lett. **B343**, 436 (1995).

[28] M. Beckmann *et al.*, *The Longitudinal Polarimeter at HERA*, Nucl. Instrum. Meth. **A479**, 334 (2002), physics/0009047.

[29] HERMES, A. Airapetian *et al.*, *The HERMES Polarized Hydrogen and Deuterium Gas Target in the HERA Electron Storage Ring*, Nucl. Instrum. Meth. **A540**, 68 (2005).

[30] T. Shin, *The Nuclear Dependence of Structure Function Ratios from Unpolarized Deep Inelastic Scattering*, PhD thesis, Massachusetts Institute of Technology, Feb 2000.

[31] HERMES, K. Ackerstaff *et al.*, *The HERMES spectrometer*, Nucl. Instrum. Meth. **A417**, 230 (1998), hep-ex/9806008.

[32] J. Steijger, *The lambda wheels, a silicon vertex detector for HERMES*, Nucl. Instrum. Meth. **A453**, 98 (2000).

[33] C. Miller, *Proposal for a HERMES Drift Vertex Chamber*, HERMES Report No. 95-072, 1995 (unpublished).

[34] J. Brack *et al.*, *The HERMES forward tracking chambers: construction, operation, and aging effects*, Nucl. Instrum. Meth. **A469**, 47 (2001).

[35] A. Andreev *et al.*, *Multiwire proportional chambers in the HERMES experiment*, Nucl. Instrum. Meth. **A465**, 482 (2001).

[36] S. Bernreuther *et al.*, *The HERMES back drift chambers*, Nucl. Instrum. Meth. **A416**, 45 (1998), hep-ex/9803005.

[37] N. Akopov *et al.*, *The HERMES Dual-Radiator Ring Imaging Čerenkov Detector*, Nucl. Instrum. Meth. **A479**, 511 (2002), physics/0104033.

[38] H. Avakian *et al.*, *Performance of the Electromagnetic Calorimeter of the HERMES experiment*, Nucl. Instrum. Meth. **A417**, 69 (1998), hep-ex/9810004.

[39] M. van Beuzekom *et al.*, *The HERMES silicon project - The radiation protection system*, Nucl. Instrum. Meth. **A512**, 44 (2003).

[40] T. Benisch *et al.*, *The luminosity monitor of the HERMES experiment at DESY*, Nucl. Instrum. Meth. **A471**, 314 (2001).

[41] CERN, *EPIO Experimental Physics Input Output Package*, CERN Program Library Long Writeup 101, 1993.

[42] CERN, *ADAMO-Entity-Relationship Programming System*, Programming Techniques Group, 1994, Users Guide, Version 3.3.

[43] *HERMES Data Quality webpage*, `http://www-hermes.desy.de/groups/daqlgrp/`

[44] T. Sjostrand *et al.*, *PYTHIA 6.3 and JETSET webpage*, 2005.

[45] P. Liebing, *Can the Gluon Polarization in the Nucleon be Extracted from HERMES data on Single High p_T Hadrons?*, PhD thesis, Universität Hamburg, Hamburg, June 2004.

[46] A. Hillenbrand, *Measurement and Simulation of the Fragmentation Process at HERMES*, PhD thesis, Friedrich-Alexander-Universität, Erlangen-Nürenberg, 2005.

[47] G. van der Steenhoven *et al.*, *New silicon-detector systems for the HERMES front region*, HERMES Report No. 97-032, 1997 (unpublished).

[48] D. Heesbeen, *Quasi-real photo-production of hyperons on polarized $^{1,2}H$ targets*, PhD thesis, Rijksuniversiteit Groningen, The Netherlands, June 2003.

[49] J. Visser, *Deep inelastic scattering off hydrogen and deuterium*, PhD thesis, Rijksuniversiteit Groningen, The Netherlands, September 2002.

[50] J. Visser *et al.*, *Design and performance of a silicon test counter for HERMES*, Nucl. Instrum. Meth. **A521**, 430 (2004).

[51] HERMES, G. van der Steenhoven, *The (spin) structure of the nucleon*, 2002, Prepared for Conference on Quarks and Nuclear Physics (QNP 2002), Julich, Germany, 9-14 Jun 2002.

[52] M. G. van Beuzekom, E. Garutti, D. Heesbeen, J. J. M. Steijger, and J. Visser, *First experience with the HERMES silicon detector*, Nucl. Instrum. Meth. **A461**, 247 (2001).

[53] A. Reischl, M. Demey, D. Heesbeen, and J. Steijger, *Lambda Wheel Alignment (part I/II/III)*, 2003.

[54] R. Kaiser, *The HERMES Recoil Detector, Technical Design Report*, HERMES Report No. 02-003, 2002 (unpublished).

[55] Vector Informatic GmbH, *CAN web page*, 2005.

[56] CAEN, *CAEN web page*, `http://www.caen.it/`

[57] J. Steijger and M. Demey, *Lambda Wheel raw data*, 2003.

[58] W. Wander, *Reconstruction of high energy scattering events in the HERMES experiment*, PhD thesis, Friedrich-Alexander-Universität, Erlangen-Nürenberg, April 1996.

[59] A. Kisselev, private communication.

[60] S. Eidelman *et al.*, *Review of Particle Physics*, Phys. Lett. **B592**, 1 (2004).

[61] D. Ejere, *Monte Carlo Simulation of Lambda Production in Deep Inelastic Scattering*, Master's thesis, Vrije Universiteit Amsterdam, The Netherlands, Oct 2000.

[62] HERMES, S. Belostotski, *Longitudinal spin transfer to the* Λ *hyperon in lepto-production*, 2001, JINR E1,2-2002-103, 192 (2002), Proc. of the IX-Workshop on High Energy Spin Physics (SPIN-01), Dubna 2001.

[63] G. Schnell, *Longitudinal polarization of the* Λ *in DIS of polarized positrons from nucleons*, PhD thesis, New Mexico State University, Las Cruzes New Mexico, May 1999.

[64] O. Grebenyuk, *Transverse Polarization of* Λ *and* $\bar{\Lambda}$ *Produced Inclusively in eN Scattering at HERMES*, Acta Physica Polonica **B33**, 3797 (2002).

[65] HERMES, A. Airapetian *et al.*, *Evidence for a narrow* $|S| = 1$ *baryon state at a mass of 1528 MeV in quasi-real photoproduction*, Phys. Lett. **B585**, 213 (2004), hep-ex/0312044.

[66] CLAS, S. P. Barrow *et al.*, *Electroproduction of the* $\Lambda(1520)$ *hyperon*, Phys. Rev. **C64**, 044601 (2001).

[67] M. Bo-Qiang, I. Schmidt, and J.-J. Yang, *Flavor and spin structure of* Λ*-baryon at large* x, Phys. Lett. **B477**, 107 (2000).

[68] A. Ferrero, Λ *Asymmetries*, September 2005, Talk given on the International Workshop on Transverse Polarization Phenomena in Hard Processes (Transversity 2005), Villa Olmo (Como), Italy.

[69] M. van Beuzekom, *Identifying fast hadrons with silicon detectors*, PhD thesis, Rijsuniversiteit Groningen, The Netherlands, May 2006.

Acknowledgements

Although I finished this Phd with not too much of a delay there were times when I thought about quitting (haven't we all). Getting through those moments and actually finishing the analysis was probably the hardest part of the past 4 years. Without the support from my girlfriend Helga, my mother Mia and my friend Andreas I would not have reached the finish. Whenever I lost track of how to proceed, which problems to tackle first and how to approach the never ending series of obstacles obstructing the final goal I could count on the support of Jos, my mentor. Always there with his analytic approaches, never fading enthousiasm and so much patience with his inexperienced students. I admire your persistence despite every set back during our cooperation in the past four years. Especially during the final stage of the thesis the help of Gerard, my promotor, was most welcome. The way Gerard can simplify the most complex physics cases is amazing, his persevering optimism can really give you that push to continue the project and his corrections and suggestions on the text of this thesis lifted my phd to a next level. During the four years in the HERMES collaboration many colleagues were there to talk to when facing a problem or to have lunch or coffee with. At NIKHEF I have to thank a.o. Paul, Andreas, Gabriel, Henk, Willem, Louk, Hella, Max, Marko (my first housemate), Vanessa, David, Erika, Armen, Johanna, Jeroen and the people from the NNV Peter, Carlijn and Ingrid. I also owe gratitude to the technical support from Martin (always available despite his packed agenda) and the happy three Rob, Arnold and Jan. During my stay at DESY there was the support (day and night) from the management Elke, Pasquale, Beni, Delia, Jim, Mathias all the fellow detector experts Micha, Vitaly, Andrzej, Guennadi, Vladimir, Dennis, Anton, Yorck and Yoerg, Davide, Marco, Avetik, Riccardo, Eduard, Larry, Yves, Bino and all the colleagues in 55a and 1e. In particular I would like to thank Oleg Grebeniouk for supporting me in starting up the Λ^0 analysis using the LW. Also a big thank you to the members of the Λ^0 subgroup who watched my progress and were a good sparring-partner, Stan, Naomi, Yuri, Anton, Paulina and Martin. Finally I would like to thank my family for supporting me wherever I was in Europe at that time and in particular Willy and Ansie, my private moving team.